POLITECNICO
MILANO 1863

SCUOLA DI INGEGNERIA INDUSTRIALE
E DELL'INFORMAZIONE

A semi-automatic pipeline for the assessment of cardiogenic emboli stroke risk using CFD simulations

TESI DI LAUREA MAGISTRALE IN
BIOMEDICAL ENGINEERING - INGEGNERIA BIOMEDICA

Author: **Carlo Bettinelli**

Student ID: 243783
Advisor: Prof. Emiliano Votta
Co-advisor: Francesco Sturla, Ione Iannirubert0
Academic Year: 2024-25

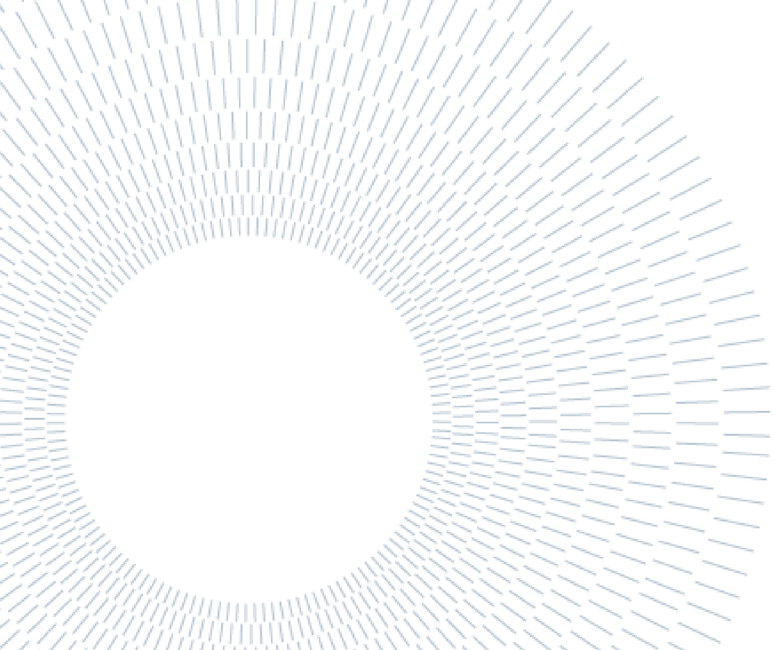

Abstract

One of the major risks associated with transcatheter aortic valve implantation (TAVI) is characterized by the occurrence of cerebrovascular events (CVE), that can lead to disabling or fatal complications, e.g. the stroke. These events are generally caused by the embolization of debris that, transported through the aortic arch (AoArch) and the supra-aortic arteries, may reach and occlude the cerebral arteries. It is supposed that haemodynamics in the AoArch, depending on its morphology, can be a factor to consider for the assessment of this risk.

Therefore, this work is aimed to study five anatomies of different AoArch types (I, II, III) to find the relationship between anatomy and particle emboli transport to the supra-aortic arteries, originating from the brachiocephalic trunk (BCT), left common carotid artery (LCCA) and left subclavian artery (LSVA). AoArch models, firstly pre-processed with ANSA to generate a finer discretization for supra-aortic vessels, were simulated with SimVascular to perform unsteady computational fluid dynamics (CFD) simulations. These simulations were carried out with the assumption of rigid aortic wall, inlet boundary conditions extracted from the patient-specific 4DFlow magnetic resonance and outlet boundary conditions defined by a lumped-parameter model (LPM) calibration to reproduce a physiological flow split. For each patient, two simulations have been performed, one with patient-specific profile from 4DFlow imaging and one with an ideal plug profile. Post-processing, performed with FlowVC, consisted of performing a particle tracking (PT) of spherical Lagrangian particles with different density and dimension, for the prediction of the main particle pathway, studying the inlet velocity profile influence.

Model validation has demonstrated the potential replaceability of the patient-specific profile with an ideal profile, the good overall prediction of flow patterns and time-dependent mean velocity trend, and the potentialities of the LPM calibration of the boundary conditions, although showing some discrepances between imaging mean velocity data and resulted mean velocity. PT analyses demonstrated that higher-density debris are more likely to remain in the AoArch, while lower-density particles tend to enter supra-aortic insertions. Type II arch resulted the most prone to the cardiogenic emboli stroke risk, with particles being transported mainly through the BCT. The difference in modelling the inlet profile shown minimum difference in terms of particles remaining in the arch and globally ending their path in the supra-aortic branches. 4DFlow profile appeared to be more able to provide an equal partition of the particles among the three supra-aortic arteries for type I and II anatomies, while for type III, demonstrated to be the AoArch type least prone to CVE risk, the recirculation at the level of the isthmus may influence the transport of particles through the LSVA, more enhanced when a patient-specific profile is considered. Type I patients were characterized by different particles percentages, demonstrating that patient-specific anatomical features may influence the CVE risk, even with the same arch type.

From this study, it emerged that anatomical features and debris characteristics can have an important role in cardiogenic emboli stroke risk assessment. Furthermore, the comparison of PT for the same anatomy simulated with different inlet velocity profiles represents an interesting analysis for the adaptability of the model to clinical environments where 4DFlow imaging is not available.

Key-words: transcatheter aortic valve implantation (TAVI), cardiogenic embolic stroke, computational fluid dynamics (CFD), patient-specific simulations, embolic particle tracking, velocity profiles comparison.

Abstract in lingua italiana

Uno dei maggiori rischi associati all'impianto di valvola aortica transcatetere (TAVI) è rappresentato dall'insorgenza di eventi cerebrovascolari ischemici (CVE), che possono sfociare in complicanze invalidanti o mortali quali l'ictus. Tali eventi sono generalmente causati dall'embolizzazione di detriti che, trasportati attraverso l'arco aortico (AoArch) e i vasi sovra-aortici, possono raggiungere ed occludere le arterie cerebrali. Si suppone che l'emodinamica in AoArch, influenzata dalla sua morfologia, sia un fattore di cui tenere conto nella valutazione di questo rischio.

Pertanto, questo lavoro si pone lo scopo di studiare cinque anatomie di AoArch di tipi diversi (I, II, III) al fine di individuare la relazione tra anatomia e trasporto di particolato embolico alle arterie sovra-aortiche, originanti dal tronco brachiocefalico (BCT), dall'arteria carotide comune sinistra (LCCA) e dall'arteria succlavia sinistra (LSVA). I modelli di AoArch, pre-processati su ANSA per la generazione di una discretizzazione più fine sui vasi sovra-aortici rispetto a quella dell'arco, sono stati simulati tramite SimVascular con lo scopo di eseguire simulazioni fluidodinamiche computazionali (CFD) non stazionarie. Le simulazioni sono state eseguite con l'assunzione di parete aortica rigida, condizioni al contorno di ingresso provenienti dalla risonanza magnetica 4DFlow del paziente e condizioni al contorno in uscita ottenute da calibrazione tramite modelli a parametri concentrati (LPM) per ottenere una ripartizione dei flussi più vicina possibile a percentuali fisiologiche. Per ciascun paziente, sono state eseguite due simulazioni, una con profilo paziente-specifico da imaging 4DFlow ed una con un profilo idealizzato piatto. La post-elaborazione, eseguita su FlowVC, ha permesso di effettuare il tracciamento di particelle (PT) sferiche lagrangiane di diametro e densità variabile per definire i percorsi preferenziali del particolato, studiando l'influenza del profilo di velocità in ingresso.

La validazione del modello ha dimostrato la possibile sostituibilità del profilo paziente-specifico con un profilo idealizzato, la buona predizione generale dei pattern di flusso e dell'andamento di velocità media nel tempo e infine le potenzialità della calibrazione mediante LPM, seppur dimostrando una certa discrepanza tra le velocità medie in aorta discendente simulate ed ottenute da imaging. Dalle analisi di PT, emerge che il particolato più denso tende a rimanere nell'AoArch, mentre quello con minore densità è più propenso a depositarsi nei vasi sovra-aortici. L'arco di tipo II è risultato essere il più incline al rischio di ictus da embolia cardiogenica, con trasporto del particolato principalmente attraverso il BCT. La diversa scelta di modellizzazione del profilo in ingresso ha dimostrato delle differenze minime in termini di particolato rimanente in arco e particolato che globalmente termina il proprio percorso nei vasi sovra-aortici. Negli archi di tipo I e II il profilo da 4DFlow tende a ridistribuire in maniera più equa il particolato tra i tre vasi sovra-aortici, mentre negli archi di tipo III, dimostratosi essere il tipo di arco meno soggetto al rischio di CVE, i ricircoli a livello dell'istmo potrebbero aver influenzato la risalita del particolato attraverso la LSVA, maggiormente accentuati dall'utilizzo di un profilo paziente-specifico. Le anatomie di tipo I sono state caratterizzate da percentuali di particolato differenti, dimostrando che caratteristiche anatomiche paziente-specifiche possono influenzare il rischio di CVE anche a parità di tipo di arco.

Dallo studio emerge che le caratteristiche anatomiche e del particolato possono avere un impatto importante sulla determinazione del rischio di ictus embolico cardiogenico. Inoltre, il confronto del PT nella stessa anatomia simulata con diversi profili di velocità rappresenta un'analisi molto interessante per l'adattamento del modello ad ambienti clinici in cui l'immagine 4DFlow non è disponibile.

Parole chiave: Impianto di valvola aortica transcatetere (TAVI), ictus embolico cardiogenico, fluidodinamica computazionale (CFD), simulazioni paziente-specifiche, tracciamento di particelle emboliche, confronto tra profili di velocità.

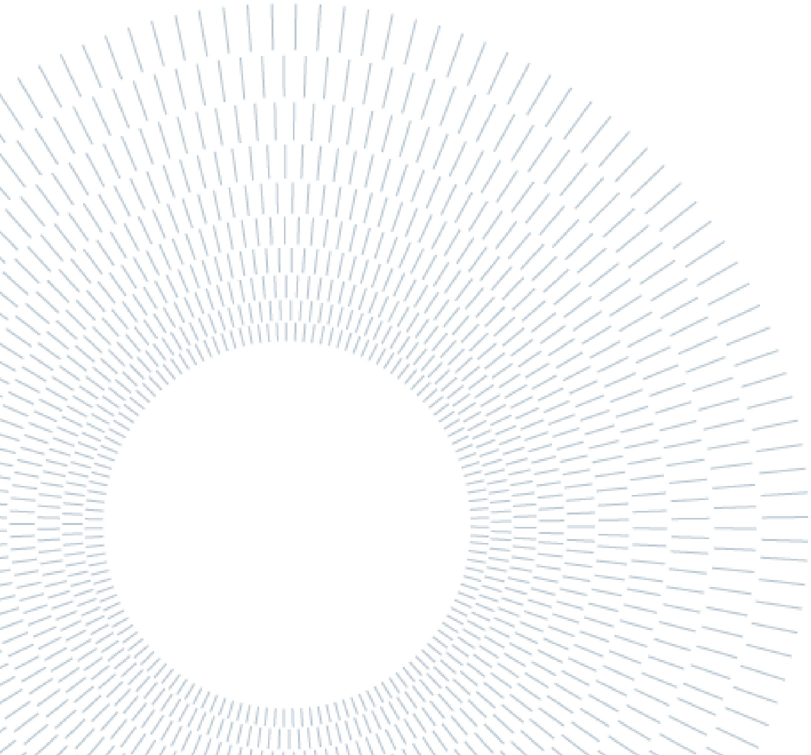

Contents

List of Acronyms

TAVI/TAVR	Transcatheter Aortic Valve Implantation/Replacement
AV	Aortic Valve
CVE	Cerebrovascular Events
SAVR	Surgical Aortic Valve Replacement
CPD	Cerebral/Cerebral Embolic Protection Devices
CFD	Computational Fluid Dynamics
TA	Thoracic Aorta
AA	Abdominal Aorta
AR	Aortic Root
LVOT	Left Ventricular Outflow Tract
STJ	Sinotubular junction
IVT	Inter-valvular Triangle
AAo	Ascending Aorta
AoArch	Aortic Arch
BCT	Brachiocephalic Trunk
LCCA	Left Common Carotid Artery
LSVA	Left (proximal) Subclavian Artery
DAo	Descending Aorta
Wo	Womersley number
St	Strouhal number

Re	Reynolds number
T-ALL	T-cell Acute Lymphoblastic Leukaemia
LDL	Low-density Lipoproteins
SBI	Silent Brain Infarction
TIA	Transient Ischaemic Attack
AI	Artificial Intelligence
CT	Computed Tomography
MRI	Magnetic Resonance Imaging
4DFlow MRI	Four-Dimensional Flow Magnetic Resonance Imaging
PWV	Pulse Wave Velocity
WSS	Wall Shear Stress
PC-MRA	Phase-Contrast Magnetic Resonance Angiography
PT	Particle Tracking
FEA/FEM	Finite Element Analysis/Modelling
FSI	Fluid-Structure Interaction
TAWSS	Time-Averaged Wall Shear Stress
OSI	Oscillatory Shear Index
ITK	Insight Toolkit
CNN	Convolutional Neural Network
GCI	Grid Convergence Index
AMR	Adaptive Mesh Refinement
NS	Navier-Stokes
RBC	Red Blood Cell
BC	Boundary Condition

2/3/4-EWKM	2/3/4-Element Windkessel Model
LPM	Lumped-Parameter Model
MAP	Mean Arterial Pressure
ROM	Reduced-Order Models
CFL	Courant-Friedrichs-Lewy coefficient
FEuM	Forward Euler Method
BEuM	Backward Euler Method
FDM	Finite Difference Method
FVM	Finite Volume Method
LPT	Lagrangian Particle Tracking
Polimi	Politecnico di Milano
STL	Stereolithography
VTK	Visualization Toolkit
VTU	Visualization Toolkit Unstructured grid
MSA	Mesh Sensitivity Analysis
VTP	Visualization Toolkit PolyData
svZeroDSolver	SimVascular Zero-Dimensional Solver
CL	Centerline
JSON	JavaScript Object Notation
BFGS	Broyden–Fletcher–Goldfarb–Shanno
svFSI	SimVascular FSI
HPC	High-Performance Computing
MAE	Mean Absolute Error
RMSE	Root Mean Squared Error

Introduction

Transcatheter aortic valve implantation/replacement (TAVI/TAVR) has been performed for the first time in 2002 by Dr. Alain Cribier in a non–operable aortic stenosis patient. Since that year, the increased knowledge on each aspect of the surgical procedure has led to extending the indication for TAVI, from inoperable cases to high- and intermediate-risk ones [1]. An estimated 180,000 patients receive TAVI every year and it is expected that the extension to low–risk patients may increase this figure to 270,000 [2].

Albeit revolutionary, TAVI is associated with several risks, including cardiovascular complications and problems related to valve durability, coronary access or aortic valve (AV) anatomy, like bicuspid aortic valve or aortic regurgitation. However, the most feared complication consists in the occurrence of cerebrovascular events (CVE), such as embolic strokes, which may cause the death of the patient or cognitive impairment with relevant functional and social consequences. Such events are mainly caused by embolization of debris from the native valve or vascular wall, which enter the bloodstream and can flow into the supra-aortic branches, i.e., the arterial branches that stem from the aortic arch and supply head and upper limbs with blood [1], but they can be also caused by embolization of air bubbles, caused by large catheters or contrast injections [3]. TAVI-related strokes are classified as acute/periprocedural strokes or subacute/late strokes. Acute strokes occur during TAVI procedures, as the expansion of the prosthetic valve induces the fracture and the migration of calcified or atheromatous tissue. Subacute strokes occur within 48h from the end of the procedure, but their causes are less known, and they are only potentially associated with TAVI [3]. The extent of stroke-related brain damage depends on the size of debris, and the risk of stroke depends on many factors, including the sex of the patient (female patients show a higher risk than male patients), the time elapsed since the operation (the risk is higher in the first day after TAVI), and the expansion mechanism of the prosthetic valve (balloon–expandable valves are associated with a lower risk than self–expandable). However, neither the use of pre- or post-dilatation nor the use of anticoagulant or antiplatelet treatments affect the risk of stroke [1].

Randomised trials have been conducted to study the incidence of stroke due to TAVI and surgical AV replacement (SAVR) in elderly people at low or medium surgical risk with severe aortic stenosis. TAVI has been shown to be non-inferior to SAVR with respect to death from any cause, including stroke, within one year, with an incidence of death from any cause 2.6% for the transcatheter procedure and 6.2% for the surgical intervention and an incidence of stroke of 2.9% and 4.7% respectively. However, SAVR presented procedural complications in fewer patients than TAVI, 1% and 1.5% respectively [3].

Cerebral protection devices (CPDs) are the most widely used prevention strategy against stroke. CPDs include capture devices, i.e., filters or net-like structures inserted near the carotid arteries to prevent embolization of the cerebral circulation, and deflector devices, i.e. large grid-like structures inserted into the aortic arch to protect the three main supra-aortic vessels [4]. However, the use of CPDs is not without limitations, which depend on the mechanism of neuroprotection: the operator must take care of preventing the re-entry of debris captured into the bloodstream and to ensure adequate protection by correctly positioning the device. When deflector devices are used, it is necessary to verify with clinical trials that their use does not affect peripheral circulation, including renal circulation, and does not create problems related to incomplete coverage of the supra-aortic vessels, damage to the vessels or arteries into which the device is introduced, thrombosis, or residual flow accumulation in the device [5]. Finally, the use of CPDs is not recommended in patients with particularly tortuous supra-aortic vessels [6].

Several predictive models have been developed to determine the risk of in-hospital stroke following TAVI. These are based on factors such as previous strokes or chronic kidney disease or peripheral artery disease [7] [8]. However, there are no documented reliable criteria for determining ischaemic risk in patients undergoing TAVI. The calcium score, which represents an index of the severity of aortic stenosis as visible in computed tomographic scans, may be a factor to consider, although it does not represent an indicator of the risk of periprocedural stroke [9]. It is therefore possible to assume that a high calcium score may represent an important parameter, as it is believed that the greater the number of calcified debris in the bloodstream, the greater the possibility that these may move towards the brain.

Since debris detached from plaques is carried in the bloodstream, it is likely that fluid dynamics is also a factor to be considered. In turn, aortic fluid dynamics, and particularly the path of debris, is influenced by the anatomy of the aorta, which depends on its shape and on the insertion points of the supra-aortic trunks. For instance, the type of aortic arch has been shown to influence blood flow vorticity in relation to aortic dissection [10].

To this end, the study herein presented aims to combine computational fluid dynamics (CFD) and particle tracking analyses to explore the role of aortic arch anatomy in the risk of TAVI-related embolism, aiming to help the definition of criteria on the use of CPD devices. This project, based on numerical simulations, could represent an important alternative to in vivo clinical trials. Experimental analyses are particularly expensive, both in terms of the materials and devices used and the manual labour involved and often involve a small pool of patients with specific requirements. A computational study, despite the modelling assumptions, is more economical and potentially more versatile.

CFD analyses were performed on five 3D aortic anatomies reconstructed by segmenting diagnostic images, acquired on patients over 65 years of age and pre-processed using CAD software to generate a volumetric mesh. Two patients were characterized by type I aortic arch, two patients were characterized by type III aortic arch, and one patient was characterized by type II aortic arch. Fluid dynamics simulations were performed using an open-source software (SimVascular) assuming that:

1. Blood behaves like an incompressible Newtonian fluid.
2. Every outlet of each fluid dynamic model is represented by a RCR lumped-parameters approach, with patient–specific values.
3. The velocity imposed at the inlet of the aortic arch is also a patient-specific parameter and is determined by a 4D Flow MRI imaging analysis of each patient. Along this study, the difference between a 4DFlow-derived patient-specific profile and an idealized plug profile are studied.

A Particle Tracking (PT) analysis was performed for each fluid dynamic field using FlowVC software, considering different locations on the aortic wall as sources of particles. Particles represent the debris and were injected into the fluid domain from the typical locations of calcified or fatty plaques, where debris is most commonly generated in the real world. Through PT analysis, the probability of debris reaching the supra-aortic branches was assessed, with particular reference to carotid and vertebral arteries, which are access channels to the cerebral circulation.

The present thesis is organized in five chapters. Chapters one and two frame the work in its broader context, describing the clinical background of the work and the current approaches to the problem tackled herein, respectively. Chapter three describes the methodology developed and applied to solve the problem. Finally, chapter four and five present and discuss the results, leading to the conclusions of the work and to the identification of possible future developments.

1 Clinical Background

TAVI-related stroke can be influenced by blood fluid dynamics, which is in turn influenced by the anatomy of the aorta. Thus, the first part of this chapter describes the anatomy of the thoracic aorta, including aortic fluid dynamics, wall histology and biomechanical properties. The second part of this chapter presents AV stenosis, TAVI and TAVI-related risks. On this basis, in the final part of the chapter the aim of the thesis is described in detail.

1.1. Anatomy of Thoracic Aorta

The aorta is the largest elastic artery in the human body [11]. It arises from the heart as thoracic aorta (TA), extends superiorly toward the thoracic outlet and then loops 180° to extend inferiorly to the diaphragmatic hiatus, where the abdominal aorta (AA) starts [12]. The TA and the AA have distinctive mechanical properties: the TA is more compliant than the AA, especially in the proximal segments, because it must maintain diastolic pressure and blood flow at the level of peripheral circulation [11].

The TA consists of four main segments (Figure 1.1):

- Aortic root (AR): it is a bulb-like 3D structure located at the transition from the left ventricular outflow tract (LVOT) to the ascending aorta. It is delimited proximally by the virtual basal ring or aorto-ventricular junction and distally by the sinotubular junction (STJ) [13]. When observed in a cross-sectional view, the AR exhibits a trilobate shape, due to the presence of the three sinuses of Valsalva, which are named left, right, and non-coronary, respectively. Each sinus houses the corresponding cusp of the AV, whose insertion line on the AR wall is crown-shaped; the three peaks of the profile correspond to the commissures, i.e., the boundaries between adjacent cusps, and define the STJ plane. The region between each commissure and the virtual basal ring, which runs through the most proximal point of each leaflet insertion line, is called inter-leaflet or inter-valvular triangle (IVT) [11]. The two main coronary arteries stem from the wall of the left and right sinuses, respectively. The AR is asymmetrical: the three sinuses have different circumferential and longitudinal extent, the right coronary sinus being larger than the left and the non-coronary sinus. Therefore, the IVTs have different sizes, and the STJ plane is not parallel to the plane of the virtual basal ring [13]. The aortic root undergoes morphological deformation throughout the cardiac cycle, reaching maximum expansion at systolic peak and minimum expansion during isovolumetric relaxation [14].

- Ascending Aorta (AAo): which runs from the STJ to the fourth thoracic vertebra, where the brachiocephalic branch originates [11].
- Aortic arch (AoArch), which includes the origins of supra-aortic vessels, i.e., brachiocephalic trunk (BCT) or innominate artery, left common carotid (LCCA), and left subclavian artery (LSVA). The AoArch is the highest region of the thoracic aorta and the region most prone to anatomical variability and congenital anomalies [15].
- Descending Aorta (DAo), which lies between the origin of LSVA and the diaphragm.

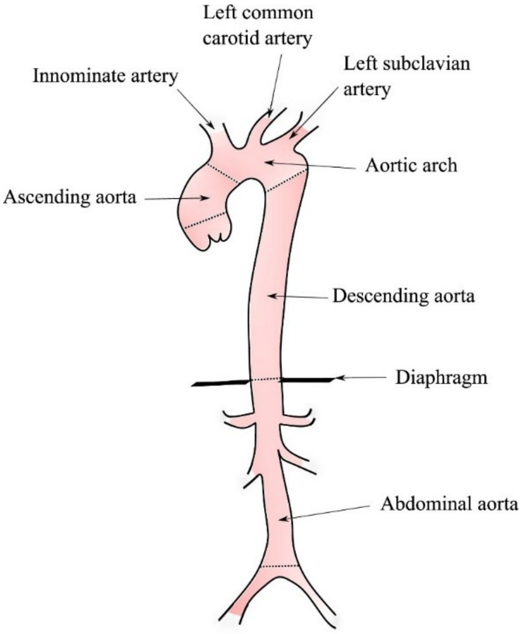

Figure 1.1: Anatomy of the Aorta: the different segments of the TA and the AA are delimited by dashed lines. The three supra-aortic vessels stemming from the AoArch are highlighted [16].

The TA diameter changes over the various tracts: it is about 23 mm at the virtual basal ring, about 30 mm at the sinuses of Valsalva, and decreases progressively to 29 mm at the AAo, 28 mm in the proximal section of the AoArch, 26 mm in the distal section of the AoArch, 25 mm at the isthmus [17], which is the part of the aorta just distal to the origin of the LSVA [18], and 24 mm at the diaphragm [17].

1.1.1. Histology and Mechanical properties of Thoracic Aorta wall

The wall of the TA is composed of three concentric layers or *tunicae*: intima, media and adventitia (Figure 1.2) [11]. The intima is the innermost tunica and is made of a single layer of endothelial cells anchored to an underlying basal membrane, a highly specialised extra cellular matrix network consisting primarily of type IV collagen, laminin, perlecan and heparan sulphate proteoglycan. Endothelial cells have the role of producing signals to control the vessel tone and produce enzymes for immune function, blood clotting and platelet adhesion [19]. The media is the thickest tunica and is made of elastin lamellae, i.e., networks of cross-linked fibres made of elastin and other microfibrillar proteins such as fibrillin, and smooth muscle cells. This micro-structure allows the TA wall to store elastic energy when the lumen is pressurized and to transfer this energy to blood flow as the pressure in the lumen decreases [19]. The thickness of the media decreases as progressively more distal tracts are considered, going from 877μm proximally to 369μm distally [20]. The adventitia is made of fibroblasts, fibrocytes and bundles of collagen supported by an external elastic lamina, and its function consists of providing tensile strength [19]. The wall thickness-to-lumen diameter ratio remains constant along the aorta: from the results of the study conducted by Mensel et al. [21], AAo thickness median value is 1.46mm for females and 1.56mm for males, while DAo thickness median value is 1.26mm for females and 1.36mm for males. Computing the ratio with respect to the diameters of the aorta in the AAo and at the isthmus (Subchapter 1.1), it can be observed that wall thickness for the AAo and the DAo is about the 5% of the corresponding diameter.

The vasa vasorum are also recognised, which serve to keep the cells of the aortic wall layers alive. They are mainly concentrated in the tunica media, and they penetrate deeper towards the lumen in the TA as compared to the AA [19].

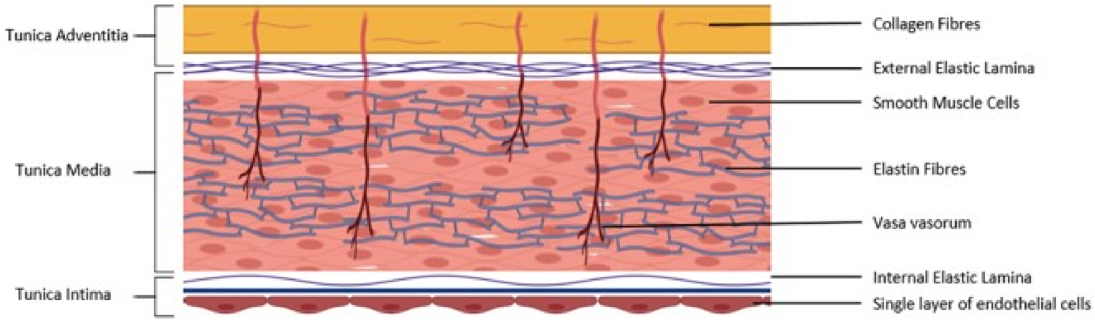

Figure 1.2: Histological representation of the TA wall: tunica adventitia is shown in yellow, containing collagen fibres and settling on the external elastic lamina and contains collagen fibres. Tunica media is shown in pink, and it is the thickest layer, characterized by smooth muscle cells, elastin fibres and vasa vasorum network. Tunica intima is shown in dark red, it is separated from the media by the internal elastic lamina, and it is characterized by a single layer of endothelial cells [19].

The tissue of the TA wall has a non-linear and anisotropic visco-elastic mechanical behaviour. It is non-linear because at low stretch levels it exhibits great extensibility and its response is mostly mediated by elastic, but as elongation increases collagen fibres are progressively recruited leading to an exponential stiffening of the tissue; when recruitment is complete, the tissue is characterized by a much greater stiffness [19]. It is anisotropic because collagen fibres are organized in two preferentially oriented families, whose directions are almost symmetrical with respect to the longitudinal direction of the wall. Under uniaxial tensile loading conditions, this arrangement provides TA wall tissue with greater stiffness and greater ultimate tensile stress in the circumferential direction than in the longitudinal one [22] [23].

Figure 1.3 shows the nominal stress – nominal stretch relationship of ten porcine aorta specimens undergoing uniaxial tests for circumferential, longitudinal and intermediate directions: specimens have been preloaded with a force of 0.05N to be straightened, then they have undergone preconditioning cycles with stretch rate of 2%/s to a nominal stretch of 1.5 and finally they have been stretched until failure at the same stretch rate [22]. Results confirm the non-linear and anisotropic mechanical behaviour of the aorta: the ultimate tensile stress is higher for circumferential direction (> 1500kPa) than for longitudinal (~ 1000kPa) and the stretch interval is wider for circumferential direction (1 ÷ 2), than for longitudinal, (1 ÷ 1.8).

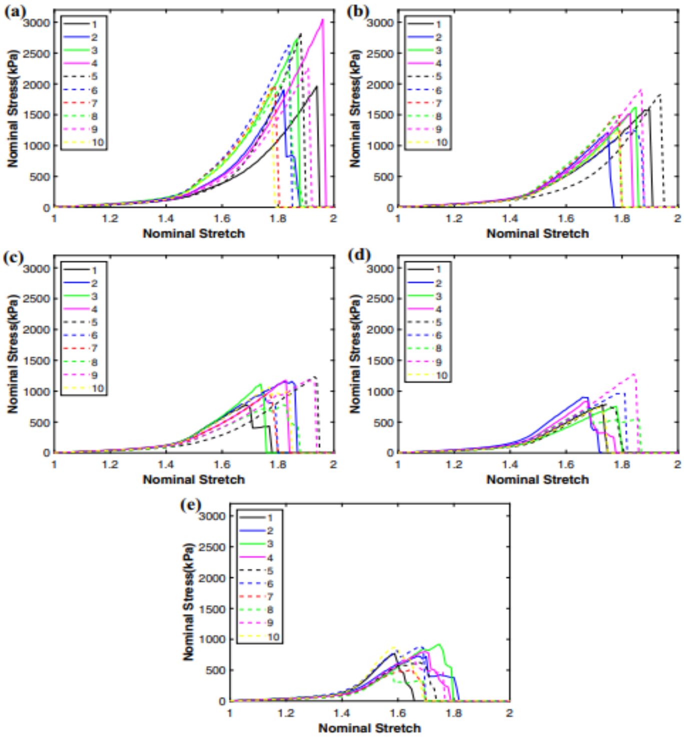

Figure 1.3: variation of nominal stress with nominal stretch for the samples oriented at (a) 0°, (b) 30°, (c) 45°, (d) 60°, (e) 90° (longitudinal) with respect to the circumferential direction for the failure test. Legend indicates the porcine aorta specimen analyzed [22]. The aorta wall is characterized by a non-linear stress-stretch relationship and by a different ultimate tensile stress (curve peaks), which is the highest for circumferential direction and the lowest for the longitudinal direction.

In healthy TAs, blood flow exhibits an incomplete-helicoidal pattern in the AAo with clockwise rotation from a posterior left to an anterior right position between diastole and systole. Flow is generally anterograde, with a component of retrograde flow in the distal end of AAo, with clockwise rotation along the aortic intrados, the inferior and concave wall of the AoArch, that goes to the great vessels during diastole and in the same period turns antegrade in the proximal AAo. In coronary sinuses, regular vortexes are seen during diastole; these are clockwise in the left sinus and counterclockwise in the right sinus. In elderly patients and in patients with coronary artery disease, anterior right skewed jet, irregular vortexes and systolic multidirectional flow are observed; therefore age, diseases and geometrical alterations of the aorta can influence aortic flow dynamics and can lead to issues related to myocardial perfusion or atherosclerosis [24]. Figure 1.4 shows magnetic resonance imaging of the blood flow, focusing on the retrograde flow along the intrados, the difference between young and old subjects and vortexes in the coronary sinuses.

Stalder and colleagues studied flow instabilities in 30 healthy aortas [25] and showed that the value of the Womersley number (Wo), which expresses the ratio between the unsteady inertial forces and viscous forces in pulsatile flows, decreases from the AAo to the DAo, so it can be observed that the effects of pulsation on blood flow are progressively lowering, because the DAo exhibits a lower flow rate than the flow rate in the AAo. However, Wo is greater than 10, indicating non-negligible pulsatility, in every tract of the TA. Contextually, the Strouhal number (St), which expresses the ratio between oscillatory and convective inertial forces, decreases along the AAo, increases at the proximal end of the AoArch, and then decreases along the DAo. Strouhal number is directly proportional to the vessel diameter and inversely proportional to the dynamic velocity range (computed as the difference between the maximum and the mean velocity acquired along the time period) and its value decreases from the start of the AAo (plane 1 of Figure 1.5) to the start of the AoArch (plane 3 of Figure 1.5), then it increases after the BCT insertion (plane 4 of Figure 1.5) and finally decreases until the end of the DAo (plane 8 of Figure 1.5). The increase of St from the start of the AoArch to the BCT insertion is related to a local reduction of the dynamic velocity range.

Mean, peak and critical peak Reynolds number (Re), which expresses the ratio between inertial and viscous forces, are higher in the AAo and in the DAo than in the AoArch because of higher blood flow velocities. The time-averaged value of Re suggests that blood flow in aorta is on average laminar, but at peak systole Re exceeds 4000, suggesting the presence of turbulent flow. In the AoArch blood flow has a lower Re because of a loss in blood flow rate, which travels in the supra-aortic branches. Results of Wo, St and Re are shown in Table 1.1 [25].

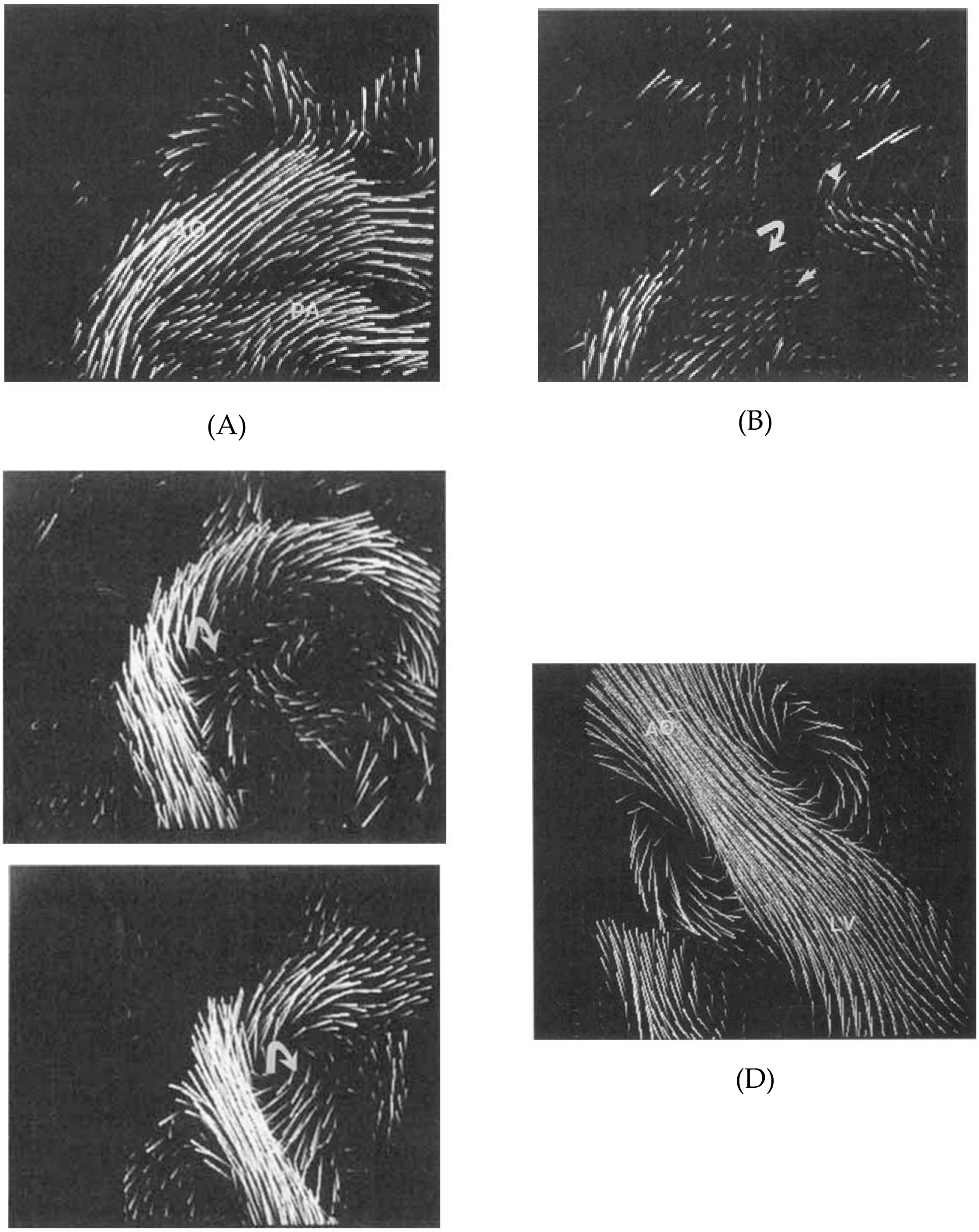

(A)

(B)

(C)

(D)

Figure 1.4: Velocity maps of blood flow in the aorta [24]. Figure A shows the velocity map in normal subject AoArch. Figure B shows the blood flow clockwise reversion along the AoArch intrados (curved arrow). Figure C shows a comparison of velocity maps from a younger (upper) and an older (lower) patient, where it is possible to notice the multi-directionality and higher skewness for the elder patient. Figure D shows the vortices in the coronary sinuses: the right sinus shows a counterclockwise rotation, while the left sinus shows a clockwise rotation.

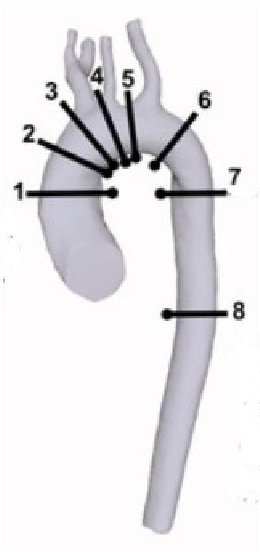

Figure 1.5: TA planes for the computation of Wo, St and Re numbers. Plane 1 is the start of the AAo, plane 2 the middle of the AAo, plane 3 the end of the AAo and the start of the AoArch, plane 4 the end of BCT insertion, plane 5 the end of LCCA insertion, plane 6 the isthmus and the start of the DAo, plane 7 the middle section of the DAo and plane 8 the end of the DAo [25].

Table 1.1: mean values of Wo, St and Re numbers along the aorta [25]. Planes are shown in Figure 1.5.

Plane	P1	P2	P3	P4	P5	P6	P7	P8
Wo	16.1	15.6	15.0	14.0	13.3	12.5	12.5	12.0
St	0.026	0.0254	0.0243	0.0263	0.0240	0.0219	0.0194	0.0164
$\mathbf{Re_{mean}}$	1200	1172	1192	1002	993	1015	1193	1277
$\mathbf{Re_{peak}}$	4528	4408	4360	3485	3393	3357	3860	4200
$\mathbf{Re_c^{peak}}$	4591	4503	4418	4082	3982	3895	3984	4050

1.1.2. Aortic Arch

The AoArch is a complex structure located between the AAo and the DAo. As stated in Anatomy of Thoracic Aorta paragraph, it represents the region that includes the origins of supra-aortic vessels, and it is the segment of TA most prone to anatomical variability and congenital anomalies, as visible through medical imaging [15]. Different criteria can be adopted to classify AoArch anatomy. The first one is based on its position with respect to anatomical landmarks and identifies four variants:

- Left-sided AoArch, which is considered as the normal configuration because it is present in most subjects [15].
- Right-sided AoArch, which runs to the right of the trachea [26]
- Double AoArch, which is characterised by a bifurcation that forms around the trachea and oesophagus, then converges into the descending aorta. The right and left pathways give rise to the respective supra-aortic trunks. It is the mostly diagnosed due to symptoms related to obstruction of oesophagus and/or trachea, that lead to swallowing difficulties in adult patients and respiratory problems in infants or children [27]
- Cervical AoArch, which is elongated at or above the level of the medial ends of the clavicles [28]

Anatomical comparison of left-sided, right-sided and double AoArch is shown in Figure 1.6, while cervical AoArch is shown in Figure 1.7.

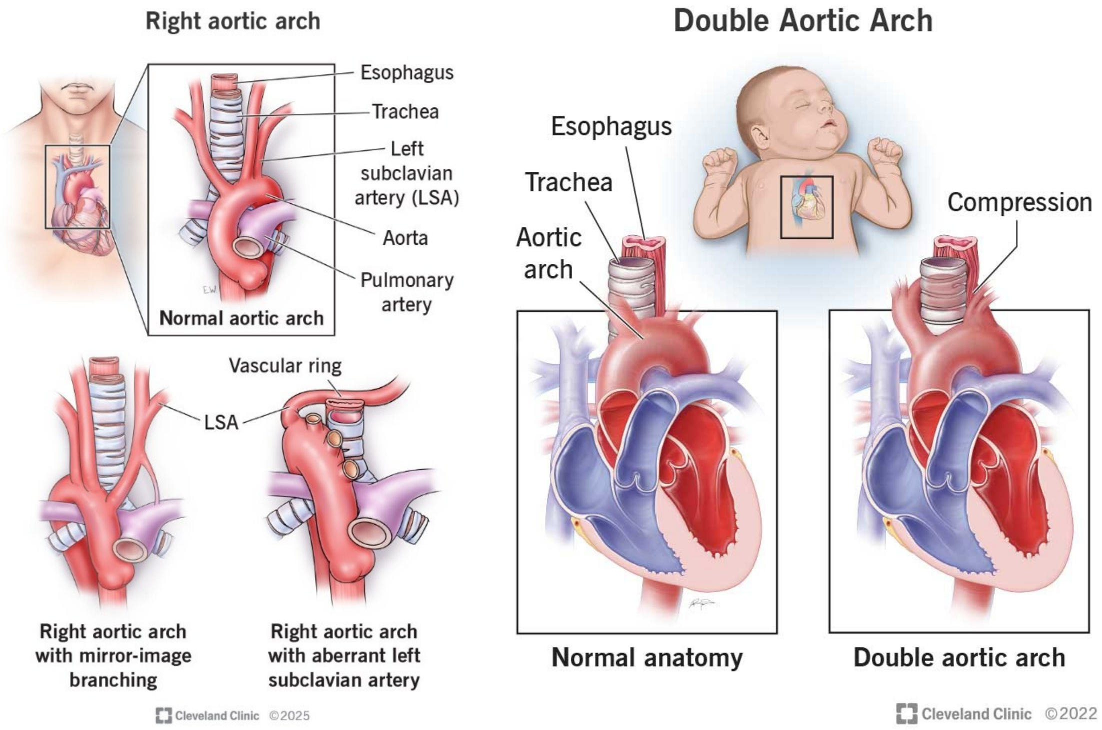

(A) (B)

Figure 1.6: comparison between normal AoArch (left-sided) with right-sided AoArch (A) [29] and double AoArch (B) [30]. The positioning of the AoArch is defined with respect to the trachea, while for double AoArch the bifurcation that envelops oesophagus and trachea, causing their compression, and the differentiation of supra-aortic origins are visible.

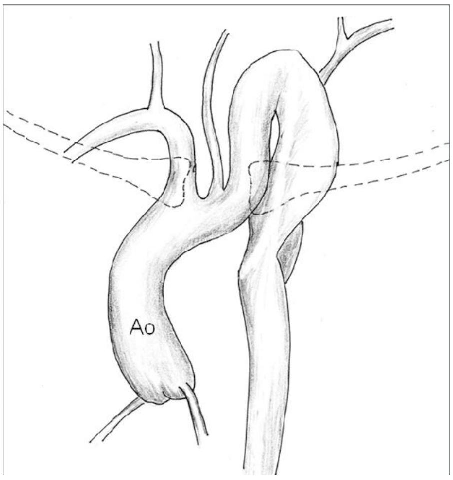

Figure 1.7: cervical AoArch. The elongation above the clavicles is visible [28].

The AoArch type has implications on the difficulty in the catheterization of the BCT. On this basis, AoArch anatomy is often classified depending on the relative distance between the origin of the first supra-aortic branch to the most superior arch wall [31], which is normalized with respect to the LCCA diameter [32]. Three types of AoArch are defined (Figure 1.8):

- Type I, where the distance from the BCT origin to the most superior arch wall is smaller than the LCCA diameter.
- Type II, where the distance from the BCT origin to the most superior arch wall is between 1 and 2 times the LCCA diameter.
- Type III, where the distance from the BCT origin to the most superior arch wall is greater than twice the LCCA diameter.

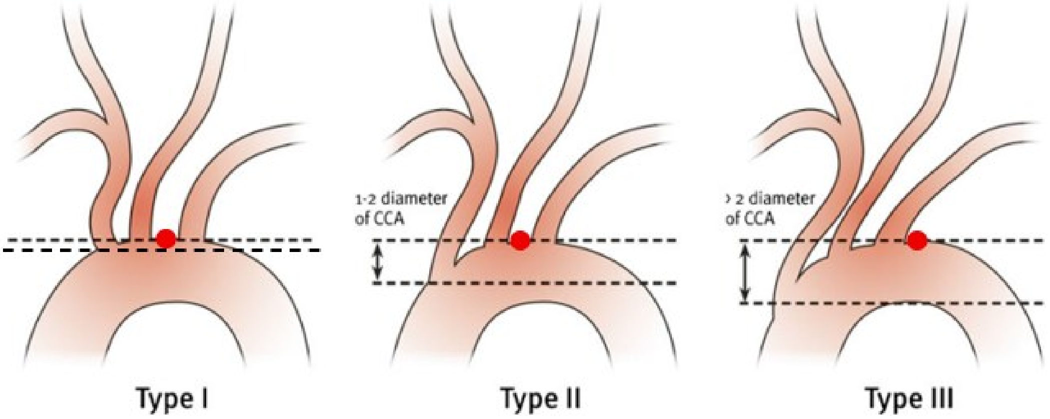

Figure 1.8: Aortic arch types based on the origins of the supra-aortic vessels to the parallel plane perpendicular to the outer curvature of the arch [33]. The inferior dashed line is set at the origin of the BCT, the superior one is set at the highest point of the AoArch, which is highlighted with the red point.

Another classification is based on the number of emerging branches, which is represented in the form "nb", where n is the number of branches emerging from the AoArch. The most prevalent type is the 3b configuration, which is considered the typical AoArch branching configuration. However, also 2b and 4b configuration are detected, although their prevalences are much lower than 3b [34]. The most frequently documented cases for 2b and 4b AoArch are the so-called “bovine AoArch”, characterized by a common origin of the BCT and the LCCA, and the aberrant left vertebral artery, where this vessel originates directly from the AoArch [15] (Figure 1.9).

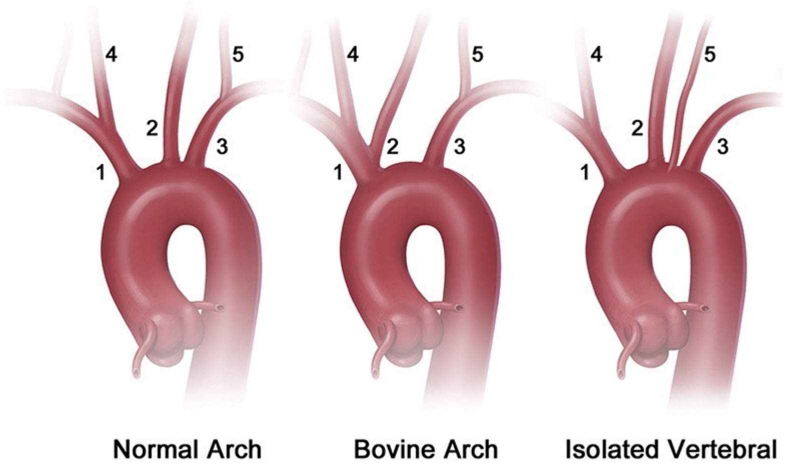

Figure 1.9: Branching configuration for normal arch and most common variants [35]. 1=brachiocephalic trunk, 2=left common carotid artery, 3=left subclavian artery, 4=right common carotid artery, 5=left vertebral artery

Many studies have tried estimating the frequency of AoArch morphologies. However, many of those, despite being run on thousands of subjects, lack the statistical power required to draw reliable conclusions. In a study conducted on a total of 1,136 patients in the Radiology Department of Gaziosmanpasa University in Turkey, the standard 3b configuration was found in 74.4% of subjects, while the bovine arch configuration and aberrant left vertebral artery configuration were observed in 21.1% and 3.7% of subjects, respectively [36]. Another study conducted at the Heidelberg University Hospital in Germany showed that type I aortic arch is the most common, with 777 cases out of 1,705 patients, while type II and III arches are less common, with 585 and 340 cases, respectively [37].

1.2. TAVI and AV Stenosis

AV stenosis is a progressive disease whose end stage is characterized by the obstruction of left ventricular outflow (Figure 1.10). If untreated, it leads to left ventricle hypertrophy due to pressure overload and ultimately to heart failure [38]. Its prevalence is about 0.2% among middle-aged adults, and it increases to 9.8% in elderly people. Mortality is not increased when aortic stenosis is asymptomatic, but the rate of death exceeds 50% at 2 years for patients with symptoms such as syncope, angina and exertional dyspnoea [39]. Currently, there are no medical therapies to prevent or slow down the progression of AV stenosis [38].

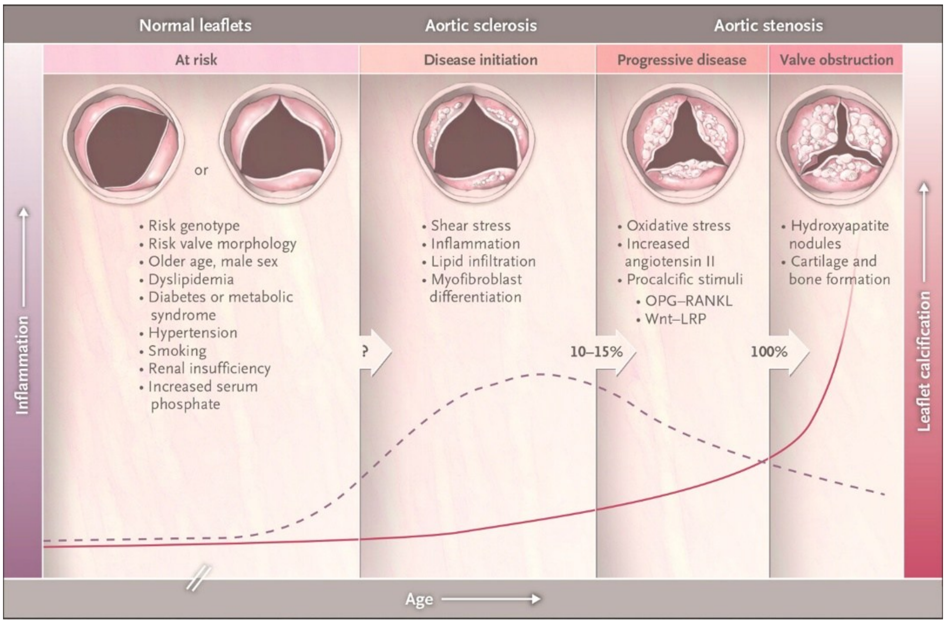

Figure 1.10: Disease mechanism and time course of calcific aortic stenosis [38].

The pathogenesis of AV stenosis depends on anatomical, genetic and clinical factors [38]. These include bicuspid AV disease [38], a congenital malformation in which the AV has two leaflets instead of the usual three and that is associated with aortic regurgitation or dilatation of the proximal aorta [40], and a mutation in the NOTCH1 gene [38], which is also responsible for certain types of T-cell acute lymphoblastic leukaemia (T-ALL) [41].

Other factors that can influence aortic stenosis are age and gender, high concentrations of low-density lipoproteins (LDL) and cholesterol, hypertension [38], metabolic disorders including diabetes [42], and unhealthy habits such as smoking or alcohol consumption [43]. For example, it is shown in a large retrospective database study in England that women and people in the most deprived areas are less prone to AV stenosis and hence are more rarely treated via AV replacement [44].

Another AV pathology is aortic regurgitation, which is a condition where diastolic backward flow re-enters the left ventricle because of incomplete AV closure. This condition is caused by leaflet disease, like bicuspid AV or ectasia of the aortic annulus, or other abnormalities that can involve the aortic root or the AAo [45].

AV replacement is the only viable option for treating AV stenosis and the main procedures, as stated in the Introduction, are SAVR and TAVI. SAVR is an open-heart intervention requires a 6-inches (about 15cm) sternotomy to access the native valve, which is removed and replaced by a prosthetic valve. The latter can be a bioprosthetic valve, with leaflets made of chemically treated animal or human tissue housed in an artificial support, or a mechanical prosthesis, made of carbon and steel and requiring anticoagulant treatment [46]. TAVI is a less-invasive intervention, so it is considered better for high-risk and unfit-for-surgery patients. It is generally performed under local anaesthesia and requires accessing a peripheral vessel, where a catheter equipped with an expandable valve is inserted and driven to the aortic root, where the prosthetic valve is deployed [47]. The use of this procedure has been extended to intermediate-risk patients and studies have been conducted to evaluate its clinical efficacy on low-risk candidates [47]. TAVI is also more versatile than SAVR because the catheter can be inserted distally through different accesses depending on patient-related factors such as co-morbidities or anatomical aspects [47]. The most common access is the transfemoral one, allowing the operator to reach the AV passing from the femoral artery, which is a direct branch of the aorta [48] (Figure 1.11).

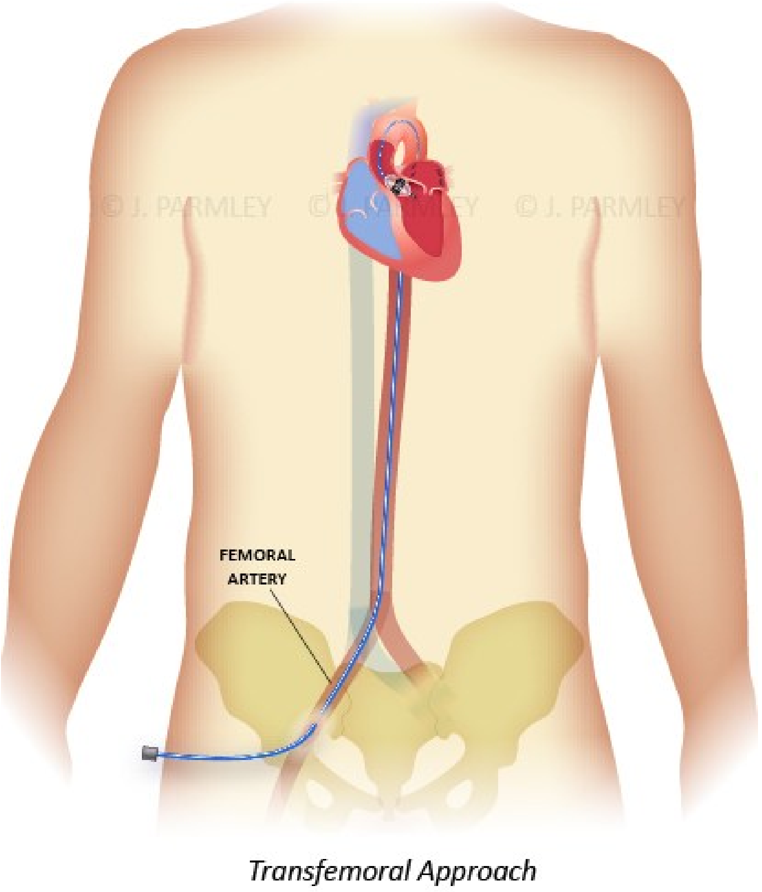

Figure 1.11: transfemoral access for TAVI. The catheter is inserted into the femoral artery and then pushed through the aorta to reach the stenotic AV [49].

As highlighted by Laborde et al. [50], TAVI procedures can present problems, which are either not directly related to the prosthetic valve or directly related to it. The former case consists in complications related to patient-specific features that complicate the access to the implant site: vascular access, and cardiac perforation or tamponade. The problems directly related to the prosthetic valve can consist in valve malposition, paravalvular regurgitation, pericardial effusion and tamponade, cardiogenic shock or low cardiac output, coronary obstruction, conduction abnormalities and rhythm disturbances.

1.2.1. TAVI-related strokes

As stated in the Introduction, TAVI-related CVE, and more specifically periprocedural strokes, are an important problem. These events are characterized by the embolization of calcified debris or air bubble and their transport from the AoArch through the supra-aortic vessels, occluding the cerebral arteries, as shown in Figure 1.12.

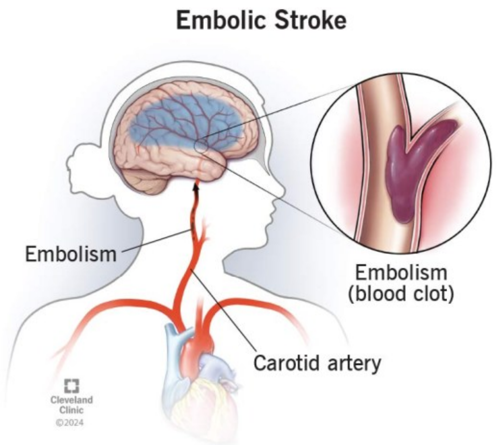

Figure 1.12: Embolic stroke [51]. The blood clot occludes the cerebral artery, blocking the blood flow that arises from the carotid artery.

According to the 2024 review by Reddy et al. [52], the risk of this fatal event has remained almost unchanged along ten years since 2011, going from 2.8% in 2012 to 2.3% in 2019 (Figure 1.13) [53].

Periprocedural stroke incidence is evaluated depending on the conviction of ascertainment and the protocol adopted, which can lead to much higher or much lower stroke rates compared to registry data [52]. For example, PARTNER 3, conducted in low-risk patients, showed a stroke rate of 0.6% [54]. Silent brain infarction (SBI) is another category of CVE, which is more insidious than stroke because it is silent in the short term but causes cognitive degeneration in the long term. Trials and observational data indicate that periprocedural strokes (at most one month after the intervention) and early phase strokes (one month to one year after the intervention) are related to TAVI, while the occurrence of late strokes seems related to age and pre-existing comorbidities [52]. Indeed, De Backer et al. [55] compared the occurrence of CVEs in about 2.500 TAVI patients treated between 2008 and 2016 vs. four groups of about 10.000 controls clustered by age, sex and comorbidities, with a 5-years follow-up. In the first 90 days, cumulative ischaemic CVE risk was 2.2% and 0.5% for TAVI recipients and controls, respectively, with a peak in the first 30 days and a statistically significant difference, which show that TAVI influences the incidence of ischaemic stroke, which is more frequent than transient ischaemic attack (TIA). Cumulative incidence of late stroke, occurring 90 days to 5 years after TAVI, was higher for TAVI patients, but without a statistically significant difference.

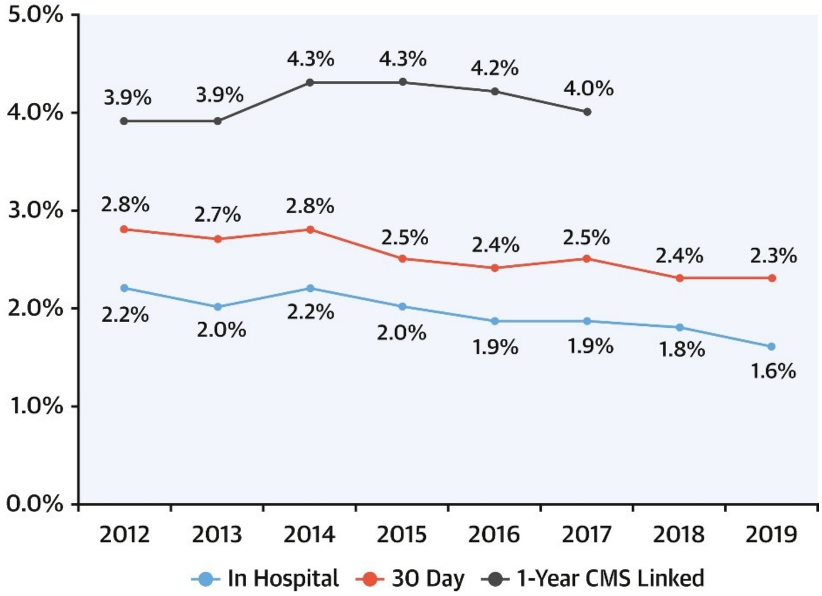

Figure 1.13: strokes rates after TAVR. In-hospital rates are in blue, 30-day rates in red and 1-year rates in gray. Data were collected by the Society of Thoracic Surgeons – American College of Cardiology Transcatheter Valve Therapy Registry from 2011 to 2019 [53].

Factors like age, sex or comorbidities, in particular diabetes mellitus, appeared to statistically correlate with the risk of late stroke in TAVI recipients. The role of diabetes mellitus was confirmed by Maida et al. [56], who reported that diabetic patients are 2-6 times more susceptible to CVEs. Reddy et al. [52] have highlighted the following causes, which are variable dependently on the occurrence time of stroke:

- Acute strokes, occurring in the first 24 hours, are generally caused by embolization of debris, periprocedural thrombus or plaques located in the Aortic Arch.
- Subacute strokes, occurring 24 hours to 30 days after TAVI, are caused by continued thrombogenesis around embolised material when anticoagulant treatment has stopped or by a delay in diagnosis due to persisting procedural sedation.
- Early strokes, occurring 30 days to one year after TAVI, can be caused by thrombosis on the new valve or acquired atrial fibrillation.

- Late stroke, occurring more than one year after TAVI, are more related to frailty or comorbidities like atherosclerosis, chronic kidney disease or diabetes [56] than the TAVI procedure, as demonstrated by De Backer et al. study [55].

Prevention of TAVI-related stroke can be performed by antithrombic treatment or by using CPDs, whose effectiveness has been suggested by recent evidence, but most of them are not yet recommended for clinical usage [57] . CPDs can be classified according to two main criteria: mechanism of action (capture CPDs and deflector CPDs) and number of vessels protected (partial and total protection devices) (Figure 1.14) [57].

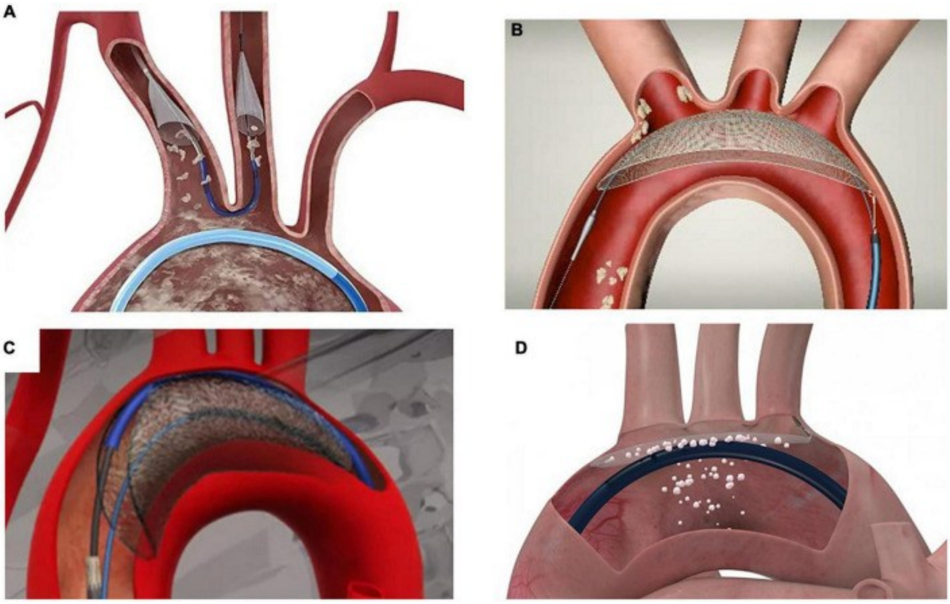

Figure 1.14: CPDs [57]. A: Sentinel® Cerebral Protection System (Boston Scientific, Marlborough, Massachusetts), partial-protection capture device. B: TriGUARD 3™ Cerebral Protection Device (Keystone Heart, Tampa, FL, USA, a Venus Medtech Company), complete-protection deflector device. C: Emblok® Embolic Protection System (Innovative Cardiovascular Solutions, Grand Rapids, Michigan), total-protection capture device. D: ProtEmbo® Cerebral Protection System (Protembis GmbH, Aachen, Germany), total-protection deflector device.

According to Jimenez Diaz et al. [57], Sentinel® (Figure 1.14A) is the most widely used CPD, and it is a partial-protection capture filter consisting of two polyurethane filters with 140-mm-diameter pores deployed into the ostia of BCT and LCCA. Evidence of its use has been demonstrated with two randomized trials, MISTRAL-C [58] and CLEAN TAVI [59], showing that patients protected with the device manifested fewer new lesions, smaller total lesion volumes and less frequent neurocognitive. The meta-analysis proposed by Ndunda et al. [60] shows that Sentinel® use can reduce the risk of stroke, mortality and severe bleeding at 30 days. However, the multicenter randomized SENTINEL U.S. IDE trial [61] shows a non-statistically significant reduction in new lesion volume on magnetic resonance scans for Sentinel®. TriGUARD 3™ (Figure 1.14B) is described as a semi-permeable nitinol mesh able to deflect particles larger than 140µm covering all the supra-aortic branches [57]. DEFLECT I [62] and DEFLECT II [63] prospective studies confirmed the safety of its usage and the decrease in lesion volume, despite a not decreased number of post-procedural cerebral lesion. DEFLECT III [64] has confirmed the safety of the device, showing a higher patients' freedom from ischaemic brain lesions in the first month and less neurological deficits and cognitive impairments, while REFLECT I [65] and REFLECT II U.S. [66] trials have shown better results in terms of cerebral protection, especially a higher coverage of central nervous system. Emblok® (Figure 1.14C) is a total-protective capture CPD made of a polyurethane mesh with pore size of 125µm and it is set in position by a nitinol frame [57]. It was tested in 2020 by Azeem Latib et al. [67], showing safety, no neurological events and a cerebral total new lesion volume comparable to other trials. ProtEmbo® (Figure 1.14D) cerebral protection system is a temporary intra-aortic deflection filter characterized by a heparin-coated mesh, whose pore size (60µm) is the smallest among the four devices reported in the article [57], and set in position with a self-expansion ensuring the appropriate coverage of all the vessels. PROTEMBO SF trial [68] was the first-in-human study for this device, showing safety and reduction in the number of new brain lesion, while PROTEMBO C Trial [69] showed also smaller brain lesion with respect to historical data.

Jimenez Diaz et al. [57] have proposed the use of antithrombotic therapy to prevent embolic strokes based on European and American guidelines [70] [71]. However, no clear guidelines have been presented, and no perfectly validated approaches are presented.

1.2.2. Imaging

Imaging techniques are fundamental to make a pre-evaluation of cardiovascular disease, including AV stenosis, and to define the right procedure for their management, either pharmacological therapy or surgical intervention. Interesting outcomes of the application of Artificial Intelligence (AI) are observed, speeding up the evaluation of diseases and vessel morphology with algorithms and information integration at different time steps [72]. Traditional imaging techniques include echocardiography, computed tomography (CT) and magnetic resonance imaging (MRI). Echocardiography is a readily available, low-cost and minimally invasive strategy for the assessment of cardiomyopathies, aortic, valvular or pericardial diseases [73] (Figure 1.15).

CT scans use motorized rotating x-rays source to generate stacked cross-sectional slices (tomographic images) representing the imaging volume [74] (Figure 1.16). CT angiography is fundamental for TAVI-planning due to its capability to dimension the prosthetic valve, detect valve properties, e.g. morphology and its degree of calcification, coronary ostial height, Valsalva sinus diameter, STJ diameter and height, AAo diameter and the vascular access of the catheter [75]. CT scans are also used to reconstruct 3D volumes of the vascular structure (Figure 1.16D).

MRI is also used to produce 3D detailed anatomical images (Figure 1.17), but differently from CT scans, the images are generated with a magnetic field, induced by a large magnet. This source forces protons to align with it and, after being stimulated by a radiofrequency, they release energy, detected by MRI sensors. Patient must remain very still to not blur the image, and can receive a contrast agent, e.g. gadolinium, to increase proton alignment velocity to the field [76]. Non-contrast MRI is recommended for patient allergic to the contrast medium, manifesting compromised renal function or having contraindications for stress echocardiography, and it is chosen when CT angiography or stress echocardiography cannot rightly assess the patient condition [81]. MRI is not recommended for pregnant women or patient with iron implants because the magnetic field can de-allocate the implant or severely affect the foetus [76]. The imaging technique is also more expensive than CT scan [76] and the longer scan time can limit its usage in TAVI planning [77].

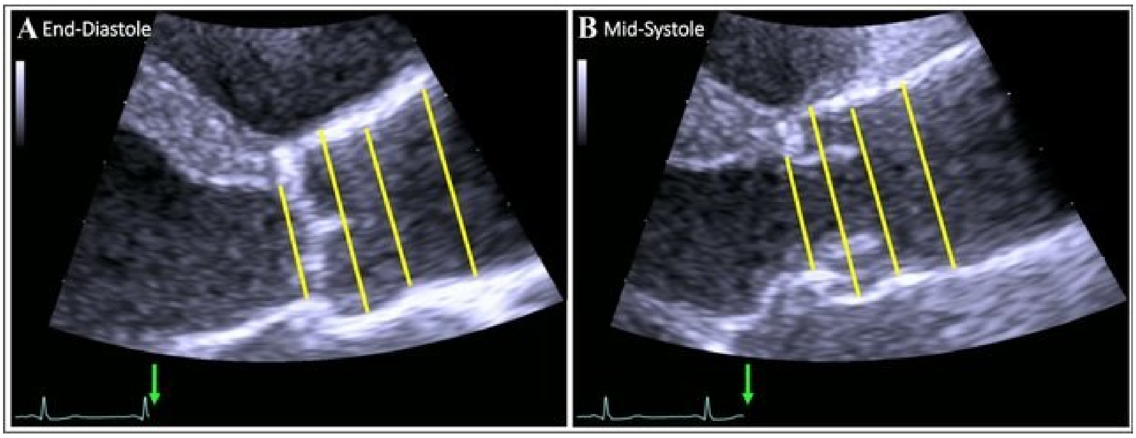

Figure 1.15: Echocardiographic measurement of the AR in end-diastole (A) and mid-systole (B) [78]. AV closure and opening are clearly visible.

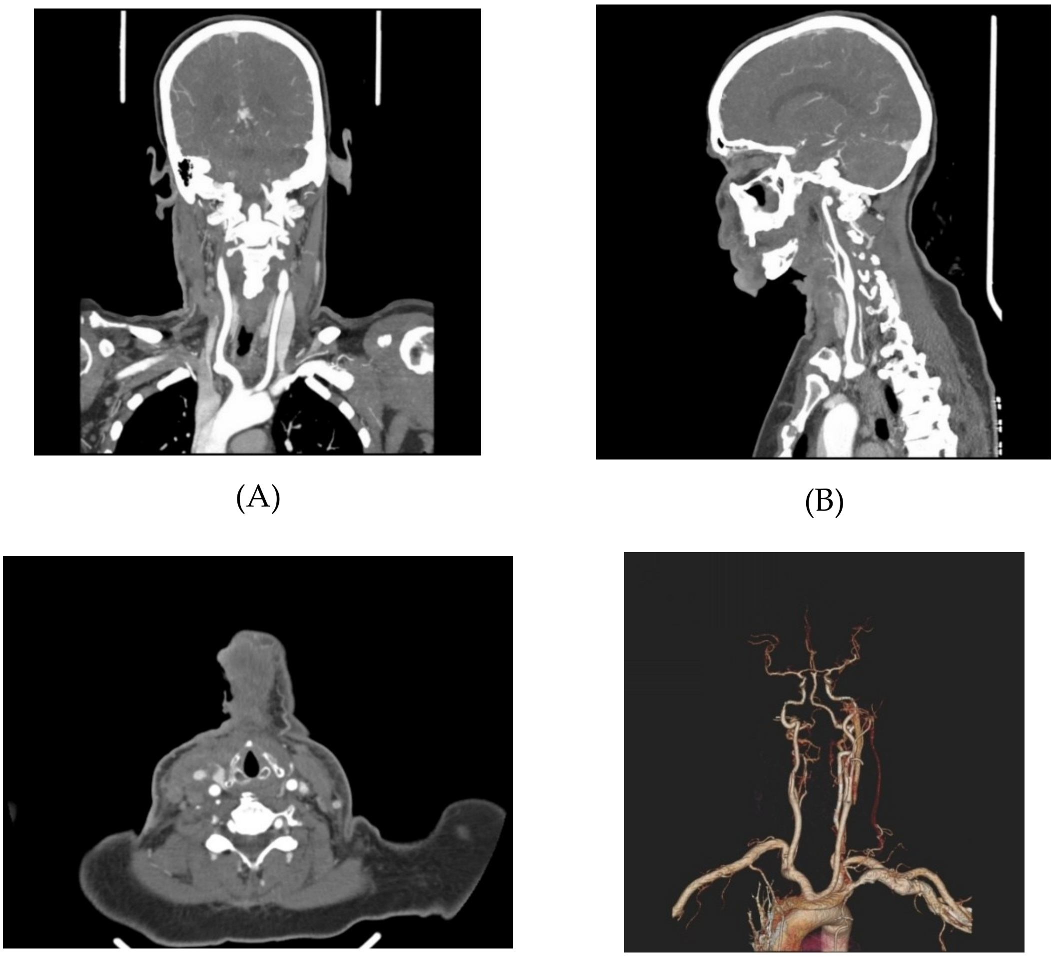

(A) (B)

(C) (D)

Figure 1.16: CT scan of a 50-year-old female patient with TIAs and previous history of operation at the right submandibular region [79]. A, B and C show respectively the coronal view (frontal), sagittal view (lateral) and axial view (top view). D shows the 3D volume rendering of the AoArch and its branches.

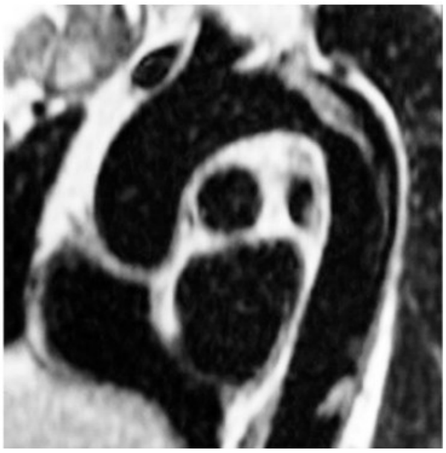

Figure 1.17: MRI image of the AAo, AoArch and DAo with a thrombus originating in the proximal part of the LSVA and extending through part of the DAo [80]. The representation of the aorta and thrombus are clearly recognizable.

In recent years, newer imaging techniques have emerged and they are based on AI integration [72] or on fusion of existing approaches [81] to improve the image quality.

One of the most important achievement is reached by the Four-Dimensional Flow Magnetic Resonance Imaging (4DFlow MRI): MRI is here aimed to generate a velocity map of aortic blood flow, which is used to measure the aortic Pulse Wave Velocity (PWV) and Wall Shear Stress (WSS) or identifying potential emboli [82]. 4D Flow can be used also to generate temporally resolved Phase-Contrast Magnetic Resonance Angiography (PC-MRA) to observe instant by instant aorta changes during the cardiac cycle [83]. PC-MRA uses flow-encoding bipolar gradients to generate images with phase-based colouring, allowing the measurements of flow speed and directionality. Two images are sufficient to generate a 1D PC-MRA, while an additional image is acquired to visualize flow in more direction [82].

Imaging is an important instrument to detect ischemic strokes. CT and MRI are used to evaluate the arteries to detect pre-cranial or intracranial stenosis or occlusion, to properly choose the right management method [84]. As said along the entire paragraph, the choice of imaging technique is related to the condition of the patient and its reaction to contrast medium.

2 State of the art

While the previous chapter represents the clinical context in which the aim of this master's Thesis places itself, this section provides the current research results for the analyses performed in the study. CFD is introduced, explaining how it can be performed, then Particle Tracking (PT) is explained, and finally previous complete works and the aim of this thesis work are presented.

2.1. CFD workflow

CFD applications in biomedical engineering, and particularly in the cardiovascular field, is aimed to assess diseases like atherosclerotic events, aneurysms or stenoses [85]. CFD is considered an important tool to evaluate and plan the treatment of these pathologies, by analysis of mechanical and hemodynamic parameters [86]. It can be coupled with Finite Element Analysis or Modelling (FEA/FEM) of vascular walls to perform Fluid-Structure interaction (FSI) [87]. In the study conducted by Carvalho et al. in 2022 [88], the comparison between CFD and FSI modelling of blood flow in stenotic coronary arteries showed that velocities, time-averaged wall shear stresses (TAWSS) and oscillatory shear indexes (OSI) were about the same as the ones computed in CFD simulations: the only difference is an overestimation of CFD-derived WSS with respect to FSI-derived ones. However, in AoArch modelling, significant differences could be observed, like the deformation of the AAo during the cardiac cycle, investigated in the PhD Thesis of the former PhD candidate from Università degli Studi di Pisa Katia Capellini [89].

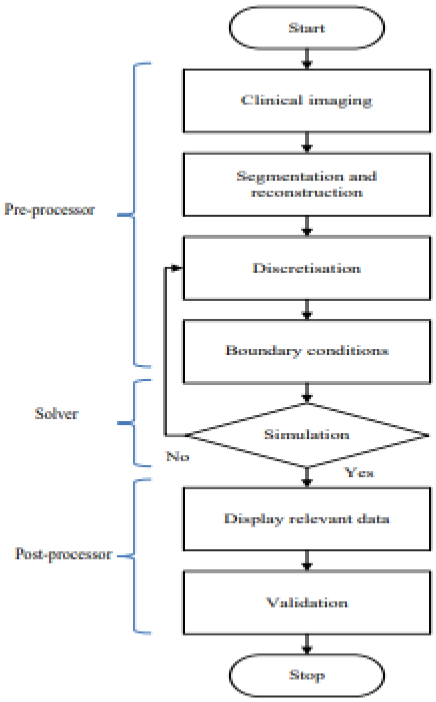

Figure 2.1: Typical CFD workflow [90]

The typical CFD modelling workflow is composed by three macro-phases (Figure 2.1): pre-processing phase, consisting of model reconstruction, spatial discretization and boundary conditions definition; simulation phase; the post-processing, based on display of the results, validation of the model and eventually other steps that exploit the CFD results for other applications. Each part of this workflow is investigated in the following subsections.

2.1.1. Geometry extraction methods

Geometry extraction is a fundamental point of CFD analyses because appropriate methods can provide a reliable vascular tree reconstruction, which is capable to guarantee reliable results. The state-of-the-art method is the segmentation of medical imaging, performed either with the use of software, e.g. 3D Slicer [91] or Materialise Mimics [92], or code libraries like the Python library Insight Toolkit (ITK) [93].

Segmentation methods can be divided into two categories: traditional techniques (intensity-based, boundary-based, region-based and model-based methods) and deep-learning based methods (Convolutional Neural Network, fully convolutional neural network, U-Net and V-Net methods) [94]. Traditional techniques are usually simple to use, although requiring much time and manual intervention and being affected by imaging artifacts or noise. On the other hand, deep-learning based, although requiring high amount of data for the algorithm training, are less dependent on manual intervention and human expertise, providing a higher accuracy and efficiency [94].

Newer methods and approaches to automatize the segmentation pipeline were introduced, like TotalSegmentator, proposed by Wasserthal et al. in 2023 [95] as a robust tool for CT images. Another automatic segmentation method based on deep-learning and the use of a convolutional neural network (CNN) was proposed in 2022 by Saitta et al. [96]: this method is capable of creating the segmentation mask and then the 3D structure of the patient imaging. SeqSeg is another automatic segmentation pipeline and it was proposed in 2024 by Cepero and Shadden [97]: it is an automatic segmentation algorithm based on sequential reconstruction of the aortic anatomy, which is performed by setting a start seed point and the propagation direction of the segmentation.

The 3D model obtained as output of the segmentation can be further processed into CAD software to obtain a structure that can be simulated. The main operations of segmentation post-processing are trimming, based on the removal of unwanted parts of the geometry or the cut of terminal parts of the outlet vessels to create the caps, smoothing, consisting on filter application to reduce noise and irregularities, wrapping, the application of a virtual veil to cover or enclose the model, and the extrusion, useful to elongate the vessels in the caps region to help the flow to develop, which can guarantee numerical convergence and more accurate results [98].

These tools are useful to create a 3D model ready to be meshed and then simulate, but right parameters and algorithms must be chosen to obtain the desired results. For example, Laplacian smoothing and Taubin smoothing works in different ways: the first one is based on the vertex diffusion, potentially leading to triangles sliding or shrinkage [99]; the second one is a generalization of Gaussian smoothing that prevents the shrinkage of elements, maintaining the initial form and dimensions [100].

2.1.2. Meshing

Meshing is a crucial step in performing a simulation of complex models like the vascular tree or the aorta. It consists of the model spatial discretization in elements generally regular in shape and dimensions, to allow the step-by-step resolution of the domain equation. In CFD simulations, only the lumen of the hydraulic system is discretized, while for FSI another mesh, representing the solid domain, must be generated.

Mesh quality and resolution have a direct effect on the quality of the simulations. A finer discretization can generate a higher number of elements leading to a higher solution accuracy, despite an increase in terms of computational time [101]. The right mesh dimension must be chosen to reach a compromise between low computational costs and the best possible accuracy. A grid independence study is required to find a compromise between mesh refinement and temporal optimization, and it is conducted by generating more than one mesh for the assessment of how much the refinement influences the solution accuracy [102]. Error calculation can be performed with different techniques, like the Grid Convergence Index (GCI) by Roache [103].

Mesh quality is also based on elements shape: highly deformed elements can introduce instabilities or numerical errors in the solution [101]. Some mesh quality metrics are reported like aspect ratio, volume ratio and skewness [104]:

- Aspect ratio: the ratio between the maximum length and the minimum length of a cell, defined with respect to the cell shape (for hexahedral cells the maximum and the minimum edge length are considered, while for tetrahedral cells the maximum cell length and the cell internal sphere radius are used to compute the parameter). The ideal value of this parameter is 1, asserting that maximum and minimum dimensions of the cell must be as similar as possible.
- Volume ratio: the ratio of volumes of adjacent cells, to observe how much the larger cell is great with respect to the smaller. If an element is near to more than one other element, the cell's volume ratio is chosen as the maximum computed for the considered element. The ideal value is 1, asserting that two adjacent cells must be similar in volume.
- Skewness: the normalized distance between a line that connects two adjacent cell centroids and the distance from that line to the shared face's centre. Skewness value can go from 0 to infinite: a good quality is observed by the lowest possible skewness value.

Elements of a volume mesh can be classified basing on their shape (Figure 2.2) and each one has its own strengths and weaknesses [105]: tetrahedral meshes can reproduce complex geometries, despite being computationally expensive due to a high cells number; hexahedral meshes are more efficient but less suitable for complex models; prismatic elements can improve the modelling of the boundary layer; pyramids cells are helpful for mesh transitions regions; polyhedral meshes, obtained by polygons construction around each tetrahedron node, show the highest efficiency, given by a reduced elements number.

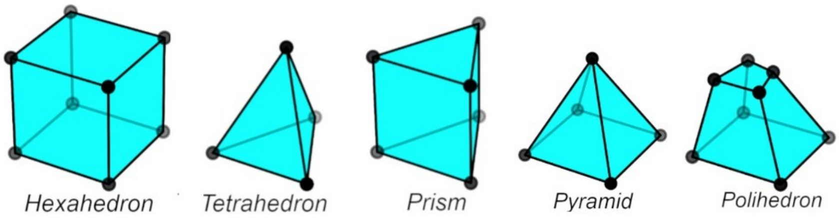

Figure 2.2: volume mesh elements shape [105].

The better efficiency of polyhedral mesh is also shown in a comparative article reported on Symscape [106], where a tetrahedral, a hexahedral and a polyhedral mesh were generated for the same model: although a comparable accuracy, polyhedral mesh was characterized by the lowest number of elements, the fastest residual convergence, the lowest number of iterations and consequentially the lowest computational time. Although polyhedral meshes are more efficient and more element-size independent than tetrahedral, it has been demonstrated that both tetrahedral and polyhedral meshes are able to provide reliable results [107].

Volume mesh elements are usually homogeneous in dimensions, but specific regions can be refined to increase the local accuracy [108] [109] (Figure 2.3): this solution is able to provide a more reliable solution without excessively elongating the computational time. The refinement can be performed either by choosing the refinement-needing part [109] or by using algorithms based on vessels dimensions [108] or simulation results, e.g. Adaptive Mesh Refinement (AMR) [110]. An example of AMR algorithm is the sub-grid scale method [111], based on the velocity vector field: by using this approach, the accuracy of the solution in the regions is obtained by progressive division of the single cell in smaller entities to progressively increase sub-grid velocity field accuracy.

Meshes can be generated by using CAD software, which can be open source or commercial. The mainly used software like STAR-CCM+, Gmsh or BlockMesh, but ANSA, a commercial software made by the Swiss company BETA CAE Systems, appears to be one of the best: its strength are researchable in a user-friendly interface, the availability of support and documentation, the feasibility to create hybrid and adaptive meshes and the prismatic boundary layer, the possibility to assess mesh quality with metrics, and the possible process automation [105]. This software is used for many applications, including biomedical modelling [112] [113].

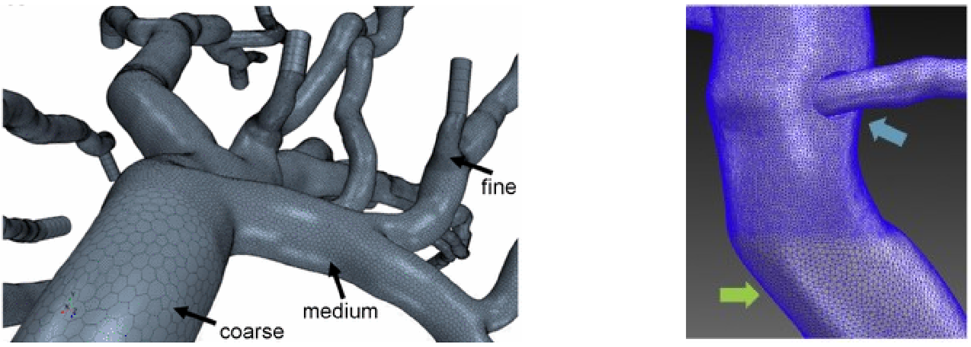

(A) (B)

Figure 2.3: examples of local mesh refinement. Figure A shows a radius mesh refinement, where higher-radius regions have a coarser configuration than lower-radius regions [108]. Figure B shows a region mesh refinement, where the region of interest (pointed with light blue arrow) exhibits a finer discretization than the rest of the model (pointed with green arrow) [109].

2.1.3. CFD simulations

CFD models are mainly solved with the Navier-Stokes (NS) equation, reported in the Equation (2.1), representing the Newton's Second Law of Motion for fluid substances [114]. ρ is the fluid density, μ is the fluid viscosity, v is the velocity vector, p represents the static pressure and g represents the body force per unit of mass [115].

$$\rho\left(\frac{\partial v}{\partial t}+(v\cdot\nabla)v\right)=-\nabla p+\mu\nabla^2 v+\rho g \tag{2.1}$$

The two elements on the left-hand side of the equation represents the local acceleration, defined by the time derivative and describing the unsteady behaviour of the flow, and the convective acceleration, defined by the spatial derivative and describing the velocity change caused by spatial factors [115]. The three terms on the right-hand side of the equation represent the forces determining the acceleration to which the fluid is subjected: these are, in order, pressure forces, defined as pressure gradient and describing the pressure difference push on the fluid, viscous diffusion forces, defined as function of velocity Laplacian and representing the dissipation of energy caused by fluid friction, and body forces, defined as constants and comprising any external force applied to the fluid dynamic system, and sometimes written as b [115].

Some simplifications may be assumed to facilitate the equation solving, e.g. the steady state (null time derivative), the absence of external forces (null external force term), or rheological assumptions related to fluid density and viscous behaviour. Blood is a non-Newtonian fluid characterized by a thixotropic behaviour: its viscosity decreases when shear-rate is high ($> 400\text{s}^{-1}$), and it is characterized by a yield stress given by the formation of rouleaux, aggregates of Red Blood Cells (RBCs) occurring at low shear rates ($< 1\text{s}^{-1}$) and obstructing the blood flow [116].

Blood viscosity also depends on the haematocrit, the percentage of the total blood volume occupied by RBCs: a higher haematocrit leads to a higher viscosity. Fåhraeus–Lindqvist effect (Figure 2.4) describes another viscosity variation, depending on the vessel diameter: when it decreases, the haematocrit near the vessel wall decreases due to the RBCs migration to the centre of the vessel lumen, reaching an absolute minimum viscosity value for radius near to 10μm, then sharply increasing for further lower diameters [116].

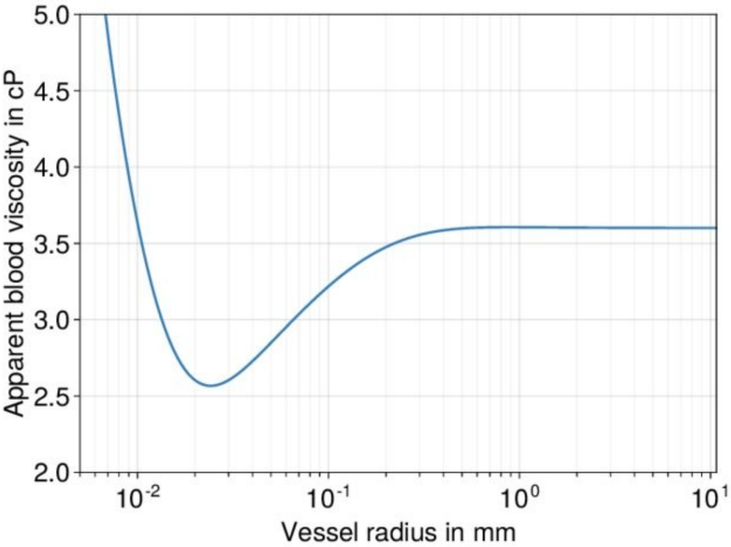

Figure 2.4: Fåhraeus-Lindqvist effect representation [117]

Blood is generally modelled as Newtonian incompressible fluid, so both viscosity and density are assumed to be constant. It is confirmed with steady [118] and unsteady [119] CFD simulations that differences between Newtonian fluid modelling and non-Newtonian fluid modelling were generally null for high shear rates, although more enhanced differences in WSS were visible in low shear rate regions. Blood flow is on average laminar in the aorta (Table 1.1): despite high values of Re in the AAo, high Wo values make the flow not develop full turbulence. Blood flow is generally assumed to be laminar and pulsatile.

Another important assumption is related to the vascular wall, modellable as rigid or deformable. Deformable wall is more accurate to model not physiological fluid dynamic conditions, e.g. aortic dissection [120] or stenosis [88], to better capture local variations of WSS. However, rigid wall assumption is mostly taken for physiological blood flow studies, assuming null wall displacement. Wall is also modelled with the condition of no-slip and no-penetration: with the first condition, fluid and wall are supposed to present the same velocity at their interface (null if wall is rigid); on the other hand, the second condition guarantees fluid migration outside or inside the domain through the wall [121].

Boundary conditions (BCs) are crucial elements for CFD simulations, representing the input of the fluid dynamic problem, defined to reflect its physical conditions. CFD BCs are usually applied to inlet, wall and outlet boundaries [122], and they are usually Dirichlet-type, (a specific value is chosen to define the BC), or Neumann-type (a gradient normal to the boundary is defined) [123]. Inlet BCs are mainly Dirichlet type [124], and the most used in cardiovascular modelling are velocity-based and pressure-based: velocity-based BCs define the inlet velocity field, represented either with constant analytical shapes, e.g. linear, cubic, parabolic or plug [125] (Figure 2.5) or as time-varying patient-specific shape from 4DFlow MRI [126] (Figure 2.6); pressure-based BCs are generally obtained from more invasive measurements [127]. It was demonstrated that models with pressure-based inlet BCs showed higher WSS and lower inlet velocity, characterized by a blunt velocity profile [128]. Other comparative studies were conducted to assess the influence of inlet velocity profile: patient-specific profiles are more reliable for the modelling of healthy or pathological aortic fluid dynamics, capturing more complex haemodynamic phenomena. However, ideal shapes can be chosen as a sufficient approximation for the study of DAo haemodynamic patterns [129] [130].

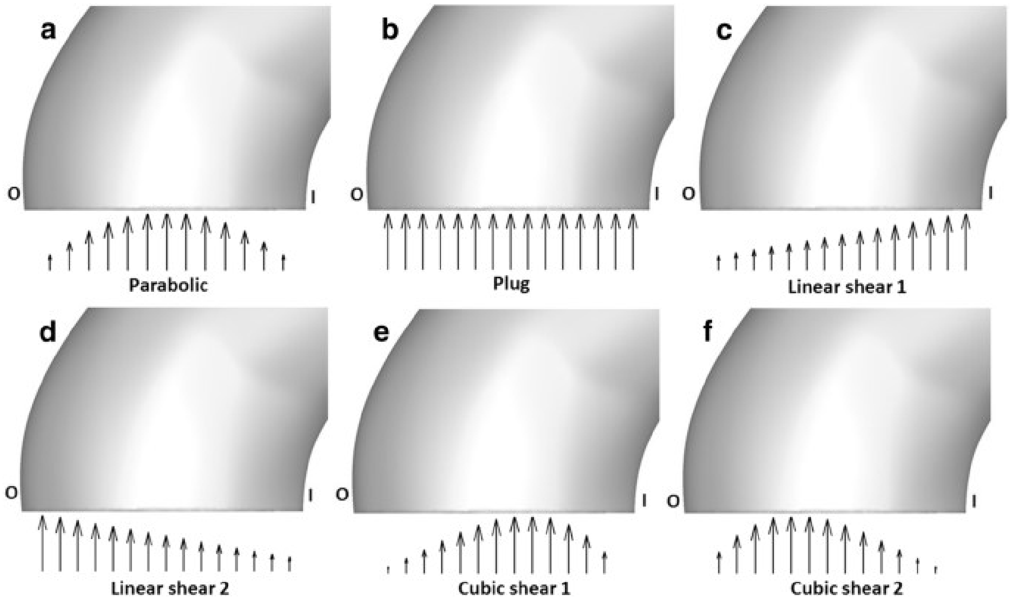

Figure 2.5: ideal shapes for inlet velocity profile [125]. I and O indicate inner and outer AoArch curve. Figure **a** shows a parabolic profile (maximum velocity is set in the central point and null velocity is measured at the inlet boundary), figure **b** a plug profile (the mean velocity is equally distributed in the whole inlet surface), figures **c** and **d** a linear shear profile (velocity increases or decreases linearly from the inner curve to the outer) and figures **e** and **f** a cubic shear profile (velocity increases or decreases with a cubic law from the inner to the outer curve).

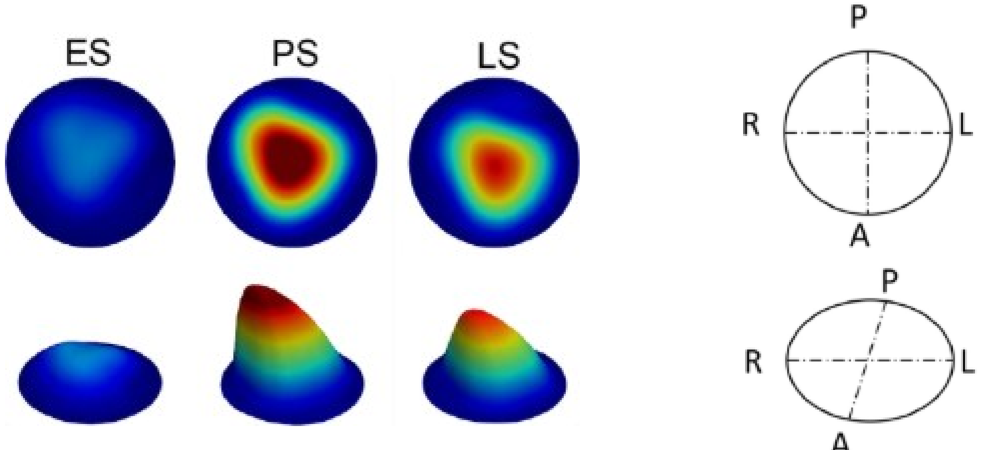

(A)

(B)

Figure 2.6: patient-specific velocity profile from 4DFlow MRI [126]. 2D color maps and 3D representation of the velocity vector field are shown for early (ES), peak (PS) and late systole (LS) in figure A, while figure B represents plane orientations (R: right, P: posterior, L: left, A: anterior). Unlike parabolic profile, velocity peak is displaced in the R-A quarter.

Outlet BCs can be either Dirichlet type or Neumann type: in the report written by Pirola et al. in 2017 [131], five configurations of outlet BCs are considered, either Dirichlet, e.g. null pressure at the outlet or prescribed flow or pressure waveforms, or Neumann, e.g. the 3-Element Windkessel Model (3-EWKM): this condition appeared to be the best for outlet modelling, giving a good flow split control and reproduction of realistic pressure waveforms. Windkessel model represents the effect of the air chamber (English translation of the German term windkessel) in converting a pulsatile flow into a rather constant flow. In cardiovascular modelling, the air chamber is represented by the elastic artery, paired with a distal resistance to guarantee a constant peripheral flow, characteristic of arterioles and capillaries [132] (Figure 2.7).

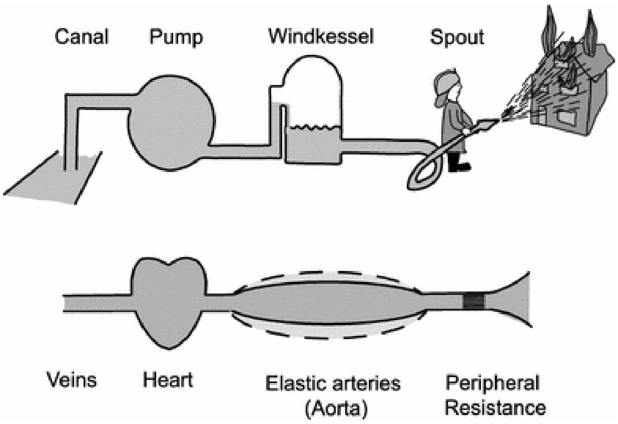

Figure 2.7: Concept of Windkessel [132]. Arterial compliance acts as an air chamber, converting a pulsatile flow given by the heart into a constant flow, given by the distal pressure given by arterioles and capillaries.

This first formulation was represented as a lumped parameter model (LPM) with one resistance and one compliance, the 2-element Windkessel Model (2-EWKM) or RC model. However, to improve this modelling other formulations are considered: 3-EWKM adds a hydraulic impedance upstream the RC model, while 4-Element Windkessel model (4-EWKM) adds to the 3-EWKM an inertance in parallel with the hydraulic impedance (Figure 2.8). The hydraulic impedance and the inertance are crucial to, respectively, describe the pressure-flow relationship during systole and to increase the accuracy for low frequencies. However, 3-EWKM is shown to be the best of the three alternatives, representing the necessary improvement to the 2-EWK [132].

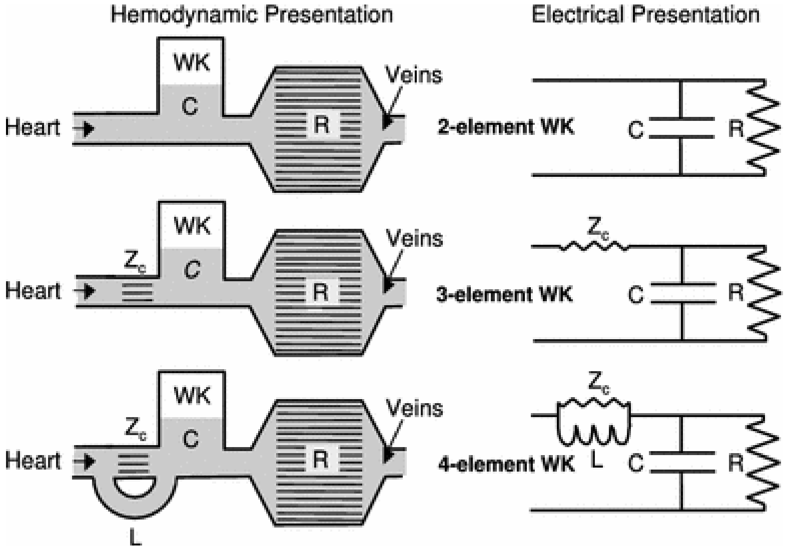

Figure 2.8: modelling of 2-EWKM, 3-EWKM and 4-EWKM [132], with haemodynamic and electrical representations. 2-EWKM is the simplest model, considering the arterial compliance (C) and the distal resistance (R). 3-EWKM adds a proximal hydraulic impedance (Z_C). 4-EWKM adds an inertance (L) in parallel to the impedance.

The definition of the parameters can be based on different rules: the most used in CFD simulations are the ones proposed by Pirola et al. [131].

Total outlet resistance is the sum of proximal and distal resistances, as assumed by LaDisa et al. [133] and reported in the Equation (2.2), which is computed as ratio between Mean Arterial Pressure (MAP) and the mean flow rate entering the outlet, as assumed by Les et al. [134] and reported in the Equation (2.3).

$$R_t = R_p + R_d \tag{2.2}$$

$$R_t = \frac{MAP}{\overline{Q}_i} = \frac{P_d + \frac{1}{3}(P_s + P_d)}{\overline{Q}_i} \tag{2.3}$$

Proximal resistance is obtained as ratio between the product of blood density ρ and PWV and the cross-sectional area of the vessel A, as theorized by Xiao et al. [135], reporting this formula in Equation (2.4). PWV is determined using the empirical correlation proposed by Reymond et al. [136] and written in the Equation (2.5), where r is the outlet vessel radius.

$$R_p = \frac{\rho \cdot PWV}{A} \tag{2.4}$$

$$PWV = \frac{13.3}{(2r)^{0.3}} \tag{2.5}$$

Compliance is obtained from the relationship between the time constant and the total resistance: the formula, which is reported in Equation (2.6), is theorized by Xiao et al. [135]. τ is assumed to be 1.79s for DAo and supra-aortic trunks.

$$C = \tau \cdot R_t \tag{2.6}$$

Distal resistance is obtained as difference between total and proximal resistances, by using the Equation (2.2).

This method is highly reliable for the DAo and supra-aortic arteries proximal sections, but not for smaller arteries. Another criticality is its dependence on population-based or empirically defined parameters. Another method is based on the use of Reduced-Order Models (ROM), in particular LPMs, to obtain an extremely quick tool for estimation of fluid dynamic measurements that can be coupled to the 3D simulation to define the lower-order twin that can be used to tune the outlet BCs [137].

Another crucial aspect of CFD simulation is the temporal discretization of the time domain. Courant-Friedrichs-Lewy (CFL) coefficient, computed as in the Equation (2.7), is an index of how fine the time domain must be discretized with respect to the spatial discretization to guarantee solution stability. CFL coefficient depends on u (velocity magnitude), Δt (timestep size) and Δx (cell dimension). It can be observed that CFL, which represents the stability coefficient of the simulation, decreases when Δt decreases or Δx increases, meaning that a simulation with coarser mesh or finer time discretization is more stable [138].

$$\mathrm{CFL} = \frac{u\Delta t}{\Delta x} \tag{2.7}$$

NS equation is numerically solved as an advection-diffusion problem [139]: the advection term is represented by the convective acceleration term of the vectorial equation, and the diffusion term is represented by the viscous term. The advection-diffusion problem can be solved with either explicit or implicit methods, like Forward Euler Method (FEuM) or Backward Euler Method

(BEuM): the first is easier to implement but requires to be correctly defined ($\mathtt{CFL} \leq 1$) to avoid instability problems; the second, despite the more difficult implementation, is always stable [140]. CFD simulations are generally performed in a tri-dimensional domain, requiring more complex methods like Finite Difference Method (FDM), FEM and Finite Volume Method (FVM): the first one is based on the approximation of derivatives as discrete differences; the second one consists of approximating the solution of the entire model by computing it element-by-element; the last one computes the numerical solution using a control-volume approach [141].

2.2. Particle Tracking

CFD post-processing is the last important step, performed by extracting raw data from simulation to interpret results or validate the model [85]. Model validation phase is performed by qualitatively and quantitatively comparing the results with clinical data, e.g. 4DFlow MRI information [142]: colour maps distribution of the interested parameter and the computation of indexes or coefficients are two examples of, respectively, qualitative and quantitative comparison.

In 2014, Shadden and Arzani enhanced the potential of the use of CFD result to study how the biomechanical factors affecting the blood haemodynamic behaviour by interpolating the velocity data to perform a Lagrangian Particle Tracking (LPT), where particles position, described by Lagrangian spheres, are obtained by sampling of velocity data interpolation [143]. This approach is based on the Maxey – Riley equation (2.8) [144], describing the force to which the particle is subjected. This is equal to the sum of five contributes: the sum of hydrodynamic forces an equivalent fluid sphere would experience, the buoyancy force, the drag force caused by mass effect, the steady drag force and the force given by diffusion of vorticity. These latter three terms include the Laplacian of the fluid velocity, called also Faxen corrections, to account local non-uniformity of velocity field [143].

$$\begin{gathered} m_p \frac{d\mathbf{v}}{dt} = m_p \frac{D\mathbf{u}}{Dt} + \left(m_p - m_f\right)\mathbf{g} - \frac{m_f}{2}\left[\frac{d\mathbf{v}}{dt} - \frac{D}{Dt}\left[\mathbf{u} - \frac{a}{10}\nabla^2\mathbf{u}\right]\right] + \\ -6\pi a\mu\left[\mathbf{v} - \mathbf{u} - \frac{a^2}{6}\nabla^2\mathbf{u}\right] - \frac{6\pi a^2\mu}{\sqrt{\pi\nu}}\int_0^t \frac{1}{\sqrt{t-\tau}}\left[\frac{d\mathbf{v}}{d\tau} - \frac{D}{Dt}\left[\mathbf{u} - \frac{a}{10}\nabla^2\mathbf{u}\right]\right] d\tau \end{gathered} \tag{2.8}$$

LPT can be numerically performed with two main integration methods to approximate the particle position: explicit FEuM, a first-order method, and Runge-Kutta algorithm, a fourth-order method [145].

2.3. Previous studies

Embolic stroke causes and outcomes are studied in the last years to predict which are the factor that can lead to this event, and which are their consequences and impairments. Either experimental or statistical methods have been used, and so they are shown in the first paragraph of this subchapter. However, the most relevant models for this study are the CFD one. They are presented in the second paragraph of the subchapter, and they can involve either the whole AoArch or only the cerebral arteries, with higher or lower grade of complexity. The aim of this panoramic is to show how the prediction of embolic stroke is performed and to define the study that guided this work.

2.3.1. Experimental and statistical models

An experimental study for the prediction of cardiogenic stroke risk had been conducted in Ireland in 2019 by Malone et al. [146]. The 3D structure of the anatomy had been extracted from an image dataset of the type II AoArch of 77-year-old male patient with atrial fibrillation and distal occlusion of right M1 vessel (M1 segment of the right middle cerebral artery). The model stereolithography, after being smoothed and extruded to increase the length of AAo and DAo, had been 3D-printed in silicone. Rheological blood properties had been replicated with a mixture of 40% of glycerine and 60% of water, while particles had been modelled by embolus analogues and clots from bovine blood. These particles had been inserted into the circulation to estimate the risk of stroke for healthy and fibrillating blood flow. However, the analysis only concerned a type II arch, and it is certainly consuming in terms of resources.

Another study for the simulation of embolic stroke has been published in 2023 by Hague et al [147]. This approach was more focused on providing a probabilistic map and finding the relationship between lesion volume and embolus diameter, so it was a statistical model that can give predictions and outcomes of this catastrophic event, not a study aimed to examinate the aortic fluid dynamics role.

2.3.2. CFD models

An analogue study was conducted during 2024 by Politecnico di Milano (Polimi) alumnus Flaminia Stentella [148]. Her MSc thesis project was based on unsteady CFD simulations with rigid wall of three aortic arch models, each one characterized by a different AoArch type and from three patients over the age of 65 who had undergone cardiovascular surgery, such as stenting or arteriotomy, and with BCs derived from morphological and 4D Flow MRI analysis. Post-processing consisted of performing PT analyses of particles of mixed-dimension and mixed-density to evaluate which factors are more likely to influence cardiogenic embolic stroke risk.

A CFD-based study on embolic travel trajectories had been carried out in 2014 in England by Fabbri et al. [149], consisting of steady simulations on the cerebrovascular network. A more recent study conducted in 2024 in the University of Teheran by Talebibarmi et al. [150] was based on FSI, introducing also the deformability of the embolus and comparison between Newtonian and non-Newtonian blood behaviour. However, these models are fundamentally limited to cerebral arteries, not considering haemodynamic behaviour of the blood in the AoArch to perform the PT. The first model [149] appears to be too simple for a reliable study, despite sharing the rigid wall assumption with Stentella’s CFD simulations [148]. On the other hand, Talebibarmi et al. model [150], due to the use of FSI analysis, and the introduction of non-Newtonian blood behaviour and particles deformability, appeared to be limiting in terms of complexity for a fluid dynamic analysis involving the AoArch.

2.4. Aim of the thesis

As stated in subchapter 1.2.1 (TAVI-related strokes), the occurrence of TAVI-related CVE is a relevant problem because of possible death, caused by stroke, or cognitive impairment, caused by SBI, which are more frequent and undetectable, occurring for more than 70% of the patient [151]. The use of CPDs is not a suitable solution for all the patients undergoing TAVI. It has been demonstrated that the anatomy of the AoArch may have an influence on the risk of acute and periprocedural stroke, observing a higher propensity to this event for bovine AoArch [152] and for curvature angle lower than 90°, especially in cases of atrial fibrillation [153]. As stated in the Introduction, AoArch morphology, dependent on its type, can lead to haemodynamic patterns developing aortic pathological conditions, so it is reasonable to assume that aortic fluid dynamics can influence plaque debris embolization and transport to the brain.

The study aims to revisit the workflow defined in Stentella's thesis [148] accordingly to the aim of the work, which consists of proposing a predictive model for the cardiogenic emboli stroke risk assessment in different AoArch types. Anatomical models are taken from a cohort of five patients that have undergone cardiovascular surgery, comprising two type I, two type III and one type II arches, all characterized by a normal branching configuration (Figure 1.9). The long-term goal of this work is to define a universal framework for a real-time assessment of CVE risk for patients that will undergo TAVI.

3 Materials and Methods

The aim of the study is to perform haemodynamic analyses within different AoArch anatomies, with a particular focus on supra-aortic branches. A workflow was defined to perform CFD simulations and particle tracking analyses (Figure 3.1). The main procedure phases are:

1. Reconstruction of the aortic arch from diagnostic images (CT scans, 4DFlow MRI and its resulting PC-MRA).
2. Pre-processing: mesh generation and data extraction for BCs definition.
3. CFD simulations with SimVascular (SV) FSI solver [154].
4. Post-processing: model validation and particle tracking.

The entire workflow (Figure 3.1) was applied to three different anatomies, while two additional models from Stentella's thesis work [148] were added to make the analysis more comprehensive.

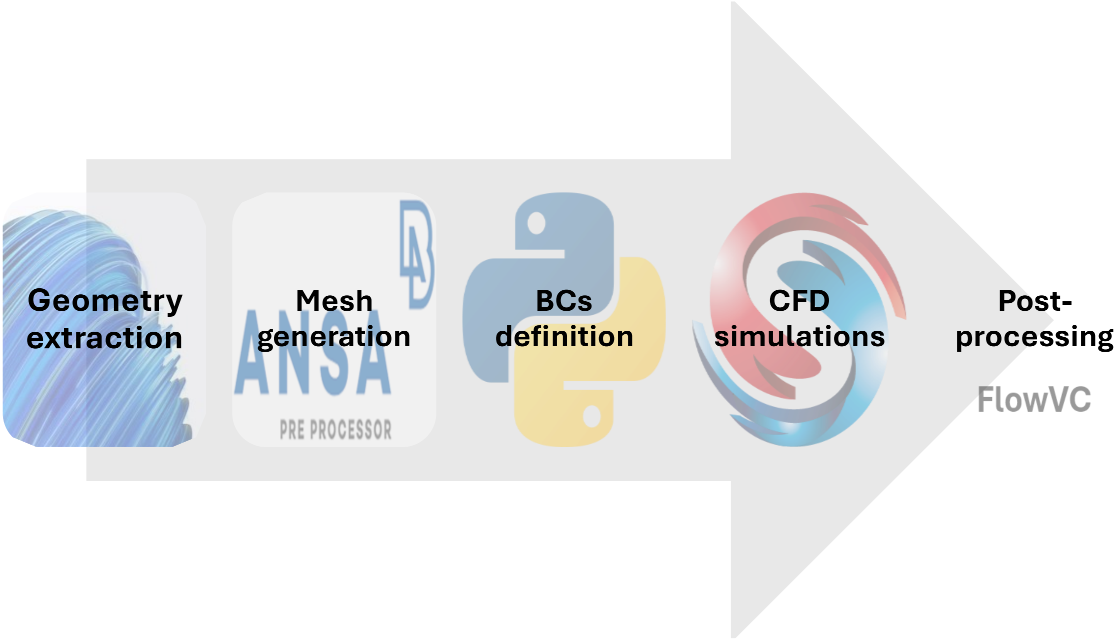

Figure 3.1: proposed workflow. For each phase, the mainly used software or tool is reported in background.

3.1. Geometry Extraction

Three patients over the age of 65 characterised by a different type of AoArch were selected from a clinical database. They had undergone cardiovascular surgery, e.g. stenting or arteriotomy, at IRCCS Policlinico San Donato (San Donato Milanese, MI). MRI and CT scans had been respectively acquired with a 1.5T MAGNETOM AERA scanner (Siemens Healthcare, Erlangen, Germany) and a SOMATOM Definition AS CT scanner (Siemens Healthcare, Erlangen, Germany) (Table 3.1).

Table 3.1: MRI and CT scans imaging parameters for each patient.

MRI Parameters					
Patient number	P24	P55	P14	P16	P45
Cubic voxel side dimension [mm]	2.05	2.04	2.05	2.05	2.05
Field of view (FOV) %	82.5	82.5	82.5	82.5	82.5
Flip angle [°]	7	7	7	7	7
Repetition time (TR) [ms]	40.8	40.8	40.8	40.6	40.8
Echo time (TE) [ms]	2.36	2.36	2.36	2.34	2.36
CT Parameters					
Patient number	P24	P55	P14	P16	P45
Isotropic quadratic pixel spacing [mm]	0.40	0.47	0.43	0.42	0.48
Slice thickness [mm]	1.0	1.0	1.0	1.0	0.75

The rough geometries were extracted using Materialise Mimics (v18, Materialise, Leuven, Belgium), a commercial software for the segmentation of medical images. The chosen segmentation method was the dynamic region growing, a semi-automatic method which, after manually selecting a point, collects all voxels with similar greyscale to create a mask (coloured CT scans regions in Figure 3.2).

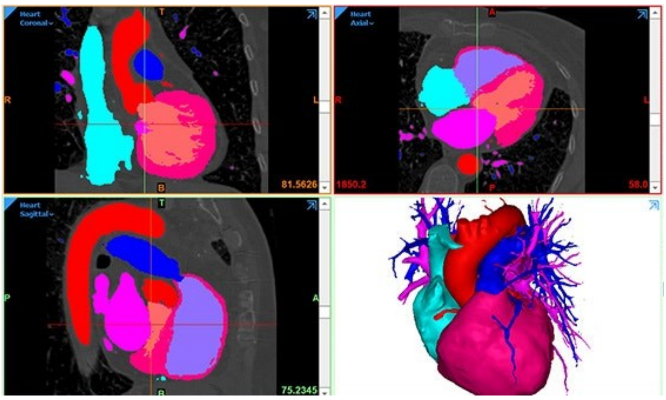

Figure 3.2: Materialise Mimics segmentation of a heart CT scan [155]. The upper left window shows the CT scan from the coronal point of view, the upper right window from the axial point of view, the lower left window from the sagittal point of view and the lower right window the 3D reconstruction of the segmentation masks shown in the other three windows. Masks are identified with colours, and they can be unified to create a unique and comprehensive model.

The method was applied to the CT scans and, whenever necessary to extend the vascular tree model, to the PC-MRA of each patient, which are inputted to Mimics as DICOM files. PC-MRA had been extracted from 4DFlow MRI data: the adopted method had been implemented by the Polimi alumnus Daniele Russo in his MSc Thesis [156] and it combined velocity-encoded and reference scans to generate angiograms to improve the vessel visualization and facilitate its segmentation. PC-MRA temporal datum was generated as product of the signal magnitude and Cartesian velocity components, with a correction factor of $\gamma = 0.2$ allowing a more similar visualization of high and low flow regions, as reported in the Equation (3.1). This formula was obtained by the method proposed by Bustamante et al. [83] and the processing leads to the conversion of DICOM images into Visualization Toolkit (VTK) file to improve 3D visualization.

$$\mathrm{PCMRA}(t) = M(t) \times \left(V_x^2(t) + V_y^2(t) + V_z^2(t)\right)^{\gamma} \tag{3.1}$$

The structure obtained by the combination of CT scans and PC-MRA segmentation was then processed in Materialise 3-Matic (v15.0, Materialise, Leuven, Belgium), where the vascular tree was further isolated from elements that had been included, e.g. parts of bones or small vessels arising from the interested ones, and then smoothed. Wrapping was applied to close the holes, then planar cut and extrusion were applied to inlet and outlet surfaces to create planar caps. The anatomy was saved as Stereolithography (STL) file. Other two anatomical models, coming from Stentella's MSc Thesis [148], were added to increment the cohort from three to five patients (Figure 3.3). However, inlet section of type I AoArch from Stentella's study [148] was corrected (Figure 3.4) with a coarse AR reconstruction obtained by filtering the points of VTK 4DFlow image, considering the ones with velocity module higher than zero.

Patient 1A – type I (A)
Patient 2A – type II (B)
Patient 3A – type III (C)

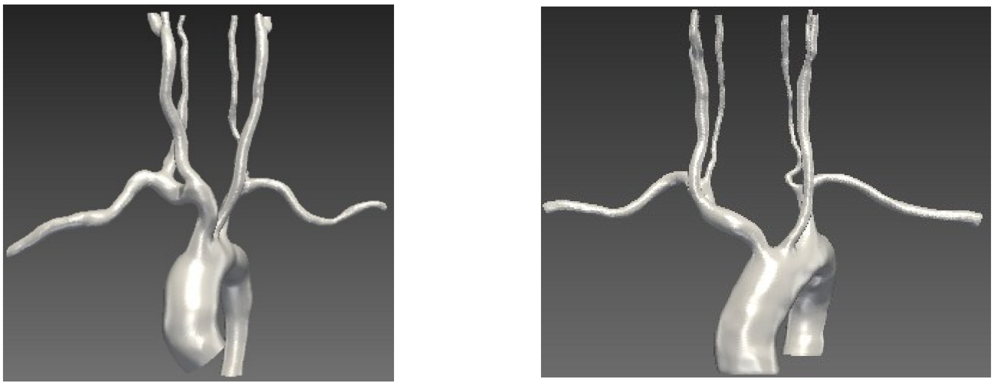

Patient 1B – type I (D)
Patient 3B – type III (E)

Figure 3.3: Anatomies analysed in the study. A, B and C anatomies come from the segmentation of CT scans and PC-MRA. D and E models come from Stentella's work [148].

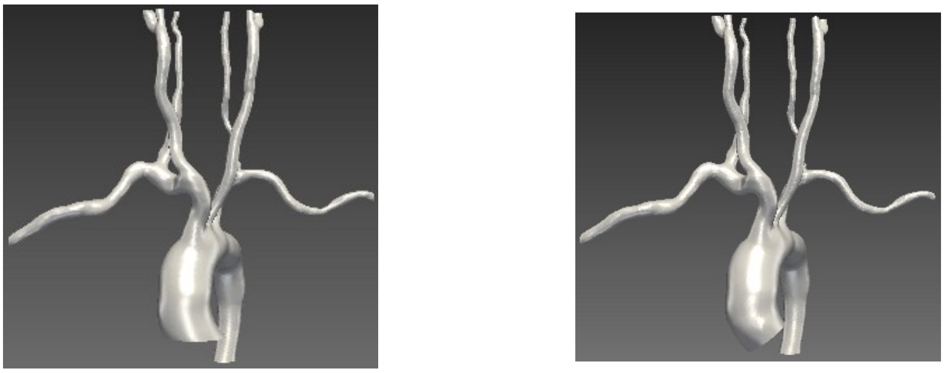

(A) (B)

Figure 3.4: Model correction for the Patient 1B AoArch. Figure A shows the anatomy analysed in Stentella's work [148], while Figure B shows the modified model. AAo inlet surface has been made orthogonal to the local aorta axis.

3.2. Mesh generation and Mesh Sensitivity Analysis

The mesh generation was performed using ANSA (v.25.0.1, BETA CAE Systems, Root, Canton of Lucerne, Switzerland), a commercial CAD software utilized in industry to build or pre-process FEM models. It proved to be a very useful tool for generating flexible meshes, particularly thanks to the Python interface called ANSA API, which allowed the process to be automated by writing scripts and functions. Algorithm 1 describes the synthetical phases of the proposed method, utilized to automatically recognize the two main topological regions and separately mesh them, analogously to the differentiated mesh proposed by Kenneth et al. [109] (Figure 2.3B). The resulting meshes were tetrahedral to guarantee the compatibility with the solver, and their strengths and weaknesses are discussed in Section 2.1.2 (Meshing).

Algorithm 1: mesh generation algorithm

1. Retrieval of information relating to the AoArch type and patient number
2. Remeshing of the segmented models to regularise the discretization
3. Recognition of the perimeters of aortic and supra-aortic caps
4. Perimeter renaming, computation of their barycentres and point saving in a text file
5. Planar cut for the distinction of AoArch from supra-aortic vessels
6. Request of an integer number as keyboard input for the generation of three mesh configurations (1: medium, 2: coarse, 3: fine)
7. Properties definition for AoArch and supra-aortic vessels (the two main regions of the models)
8. Surface mesh generation for the two main regions
9. Volume detection and volume mesh generation
10. Saving the volume mesh as Visualization Toolkit Unstructured grid (VTU) file

The perimeter renaming was performed by knowing the relative positions of each cap. The x, y and z axes correspond to the transverse, sagittal and longitudinal directions, respectively. x increases toward the left and y toward the posterior (back) direction, because these axes are reversed. With this convention, the aortic caps have barycentres at the lowest z-values. The AAo cap barycentre has a smaller y-coordinate than the DAo cap barycentre. Among the supra-aortic branches, the right subclavian artery shows the smallest x-coordinate, whereas the left subclavian artery shows the largest x-coordinate. The recognition of carotid and vertebral arteries perimeters was not obvious, and required a more complex process, explainable in two phases:

- **Distinction of right-sided and left-sided arteries**: for every model except the 3A anatomy (Figure 3.3C) one vertebral artery and two carotid arteries are recognizable, forming a group of three ipsilateral vessels. The two groups were distinguished basing on the x barycentre coordinate: right-sided arteries exhibit the three lowest values, while left-sided exhibit the three highest. For 3A anatomy, the groups were composed by only two ipsilateral vessels, distinguished in an analogous way.

- **Specific distinction of the vessels**: vertebral artery is located behind the carotid arteries, so its perimeter barycentre generally exhibits a higher y-value. Internal and external carotids, not distinguishable for 3A anatomy, were determined by considering their barycentre x-coordinate value: left internal has a higher value than left external and vice versa for the right carotid arteries.

Defining the property was another key step to distinguish the main topological regions and enable region-specific discretization. After applying the planar cut, all elements below the plane were assigned to the AoArch, whereas all elements above the plane were assigned to the supra-aortic vessels, independently of which specific supra-aortic branch they belonged to. The different properties are viewable as chromatic regions, and the elements of the chosen property can be extracted to be manipulated and meshed separately from the others (Figure 3.5). A detail of the differentiated discretization, showing the difference in terms of AoArch and supra-aortic meshing, is reported (Figure 3.6).

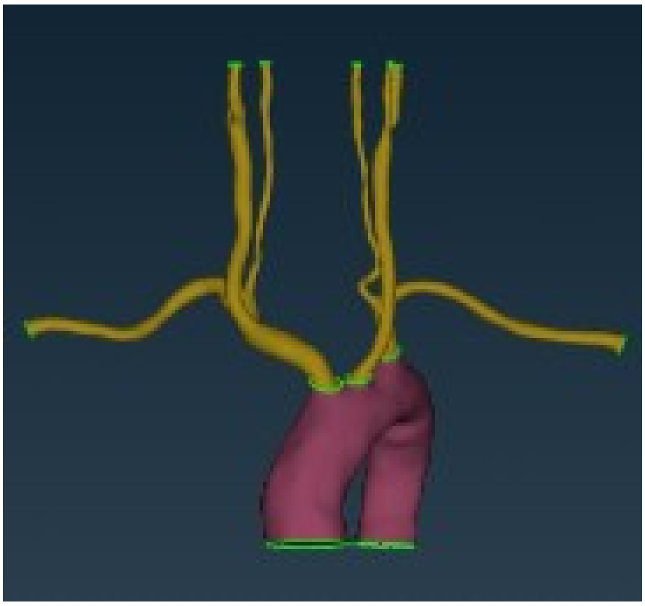

Figure 3.5: property distinction. The purple region is the AoArch, while the yellow elements are the supra-aortic branches. Green lines are the perimeters and the ones that separate the two distinguished regions are obtained by the planar cut.

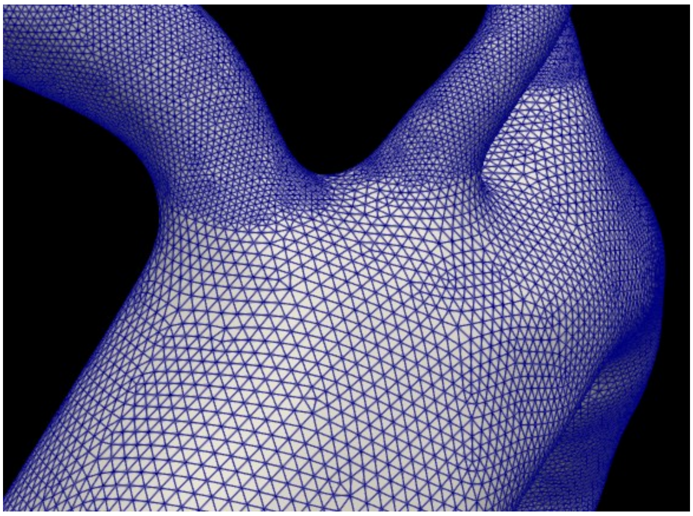

Figure 3.6: mesh differentiation obtained in ANSA. AoArch has higher-dimensional elements, while supra-aortic branches exhibit a finer discretization. The distinction of these two macro-regions obtained by planar cut is recognizable.

Three meshing configurations (Table 3.2) were generated on the anatomy 3B (Figure 3.3). The choice of using a type III AoArch had been taken because of its sharp curvature, which may provoke haemodynamic disturbances [10]. For each mesh, a steady-state CFD simulation was executed to perform a Mesh Sensitivity Analysis (MSA).

Table 3.2: Mesh features for each investigated mesh type (coarse, medium and fine).

	Coarse	**Medium**	**Fine**
Edge size variation for aortic arch [mm]	1-2	0.5-1	0.25-0.5
Edge size variation for supra-aortic branches [mm]	0.25-1	0.125-0.5	0.125-0.5
N° of Elements	253,776	1,079,002	2,176,937
N° of Nodes	58,209	224,257	438,260
Mesh Type	Tetrahedral	Tetrahedral	Tetrahedral

For each simulation, average velocity and pressure and maximum velocity and pressure were calculated for five cross-sections located in the AAo, DAo and in the three supra-aortic trunks (Figure 3.7). The extraction of the five slices and the calculation of the four parameters was executed in Paraview (v5.12.1, Kitware, Clifton Park, New York, USA), an open-source application for post-processing analyses. The program is equipped with a Python script editor, used to automize the work.

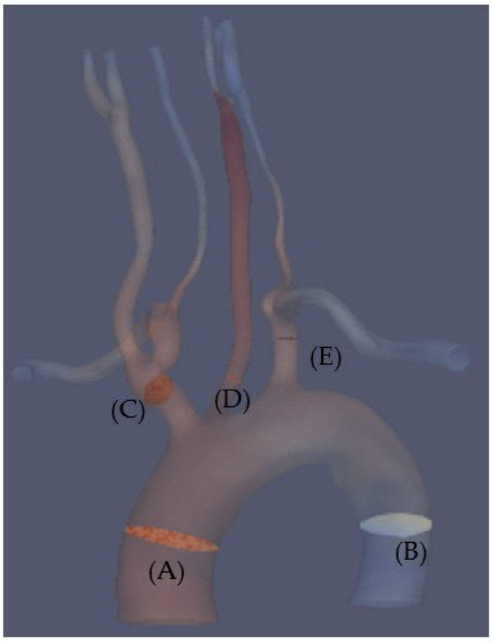

Figure 3.7: slices location for the MSA (A: AAo, B: DAo, C: BCT, D: LCCA, E: LSVA).

GCI method's framework described in Roache's study [103] was followed. GCI coefficients were computed for fine-to-medium ($\mathrm{GCI}_{1,2}$) and medium-to-coarse ($\mathrm{GCI}_{2,3}$) mesh pairs, providing an estimate of the fractional error in the variables of interest f (mean velocity, maximum velocity, mean pressure, maximum pressure) and predicting how much it would change with the grid refinement. The refinement, which is defined as the ratio between two couples edge sizes, is set as $r = 2$ and the convergence order, defined as p, was computed with the formula in Equation (3.2). A safety factor called F_s, assumed to be 1.25 accordingly to Roache recommendation, was applied to the errors E_1 and E_2 (Equation (3.3)) to obtain GCI, reported in the Equation (3.4). k was computed with the formula in Equation (3.5) and a near-to-1 value for this coefficient shows the reaching of asymptotic convergence range

$$p = \frac{\ln\left(\frac{f_3 - f_2}{f_2 - f_1}\right)}{\ln(r)} \tag{3.2}$$

$$E_1 = \frac{f_2 - f_1}{f_1(r^p - 1)} \quad E_2 = \frac{f_3 - f_2}{f_2(r^p - 1)} \tag{3.3}$$

$$\mathrm{GCI}_{1,2} = F_s \cdot |E_1| \quad \mathrm{GCI}_{2,3} = F_s \cdot |E_2| \tag{3.4}$$

$$k = r^{-p} \cdot \frac{\mathrm{GCI}_{2,3}}{\mathrm{GCI}_{1,2}} \tag{3.5}$$

Results of the MSA are shown in Results section (chapter 4), where it was demonstrated that the defined medium mesh (Table 3.2) was the best compromise for computational time and solution accuracy, extending this configuration to the other anatomical models.

3.3. Boundary Condition Definition

CFD simulations BCs are applied to the vessel lumen and are defined for wall, inlet and outlets. Wall BCs is a Dirichlet condition representing wall displacement and in the presented simulations is set at zero (rigid and still in space aortic wall).

Inlet BC is a Dirichlet-type BC representing the time-variable velocity of blood flow entering the AoArch. Stentella had chosen a parabolic velocity profile with values determined by 4DFlow [148]. However, a plug and patient-specific 4DFlow profile were considered for this work to assess the model feasibility for study centres where 4DFlow MRI is not available or clinically used. Main steps of this process are shown in Algorithm 2. Following the procedure adopted in Section 3.1 (Geometry Extraction), a coarse reconstruction of the AoArch was obtained by filtering the VTK-derived 4DFlow MRI dataset to facilitate registration of each computational model to measured velocity field. The reconstructed flow-rate wave form was then interpolated to enforce zero flow at the beginning and end of the cardiac cycle. Finally, the single-cycle waveform was periodically repeated to generate a three-cycle inlet condition, providing sufficient time for the numerical solution to reach a stable periodic regime.

```
Algorithm 2: inlet BC definition
1:  Arch reconstruction by filtering VTK 4DFlow data
2:  Alignment of the volumetric mesh (VTU file format) to the 4DFlow VTK files
3:  Registration of the velocity field on the inlet cap for twenty VTK data
4:  Flow rate interpolation along the entire cardiac period
5:  Single-cycle wave flow rate replication to generate a three-cycle wave
6:  Scaling from $cm^3/s$ to $mm^3/s$ and saving as Visualization Toolkit PolyData (VTP) file
7:  Computation of the number of time steps, number of inlet surface points and flow rate along the time to write the .flow file
```

Outlet sections, located in the distal ends of the DAo and of the supra-aortic branches, were characterized by 3-EWKM BCs (Neumann-type) (Figure 3.8). Knowing the limits in terms of flow split estimation of Pirola et al. method [131], the use of LPM (Figure 3.9) was proposed to determine a physiological split in the main arteries of the supra-aortic trunks. This method involved the use of SimVascular Zero-Dimensional Solver (svZeroDSolver) (Ubuntu-24-2025-07-02 version, Stanford University, Stanford, California, USA) [157], a toolkit able to solve ROM simulations. This solution provides a much faster outlet BCs calibration, due to solution algorithm implemented with the programming language C++, and so allowing to replace time-consuming iterative trials on 3D models. The synthetical steps of the outlet BC definition are reported in Algorithm 3. Centerlines (CL) were extracted with the ROM Simulation section of SV graphical user interface as the lines connecting the AAo inlet to each outlet (Figure 3.10). CLs are equipped with indexes and parameters that can allow the recognition of branches and bifurcation [158]. svZeroDSolver input files are JavaScript Object Notation (JSON) type, a light-weight, human-readable and language-independent file format, and they were generated by reading the CL, recognizing branches and bifurcations by their ID and computing internal branch resistances with Poiseuille's law, reported in Equation (3.6).

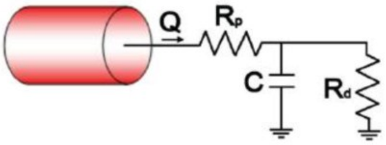

Figure 3.8: 3-EWKM representation [159]. R_p represents the proximal hydraulic impedance, R_d the distal resistance and C the arterial compliance.

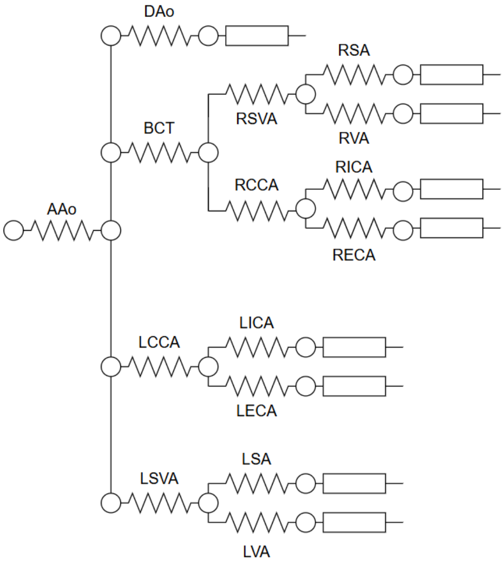

Figure 3.9: LPM general representation of the analysed models. The main branches recognized are: Ascending Aorta (AAo), Descending Aorta (DAo), Brachiocephalic Trunk (BCT), Right proximal Subclavian Artery (RSVA), Right distal Subclavian Artery (RSA), Right Vertebral Artery (RVA), Right Common Carotid Artery (RCCA), Right Internal Carotid Artery (RICA), Right External Carotid Artery (RECA), Left Common Carotid Artery (LCCA), Left Internal Carotid Artery (LICA), Left External Carotid Artery (LECA), Left proximal Subclavian Artery (LSVA), Left distal Subclavian Artery (LSA), Left Vertebral Artery (LVA). The rectangles at the end of the outlet vessels represent the outlet BCs (Figure 3.8), where compliance (C) was neglected for steady ROM simulations. For patient 3B (Figure 3.3C), outlet BCs of carotid arteries are appended directly to the LCCA and RCCA resistances.

```
Algorithm 3: outlet BC definition
1:      CL extraction and preliminary outlet BCs definition
2:      3D steady simulation
3:      JSON file generation for 0D simulation
4:      Internal circuit calibration
5:      Outlet BC calibration
6:      3-EWKM parameter computation
```

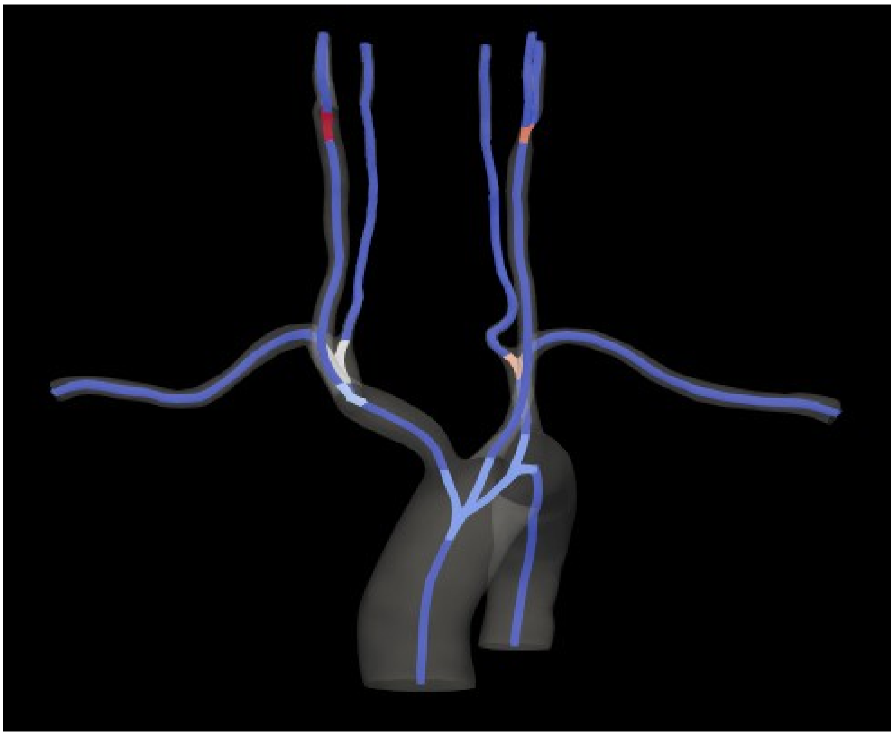

Figure 3.10: CL of the vascular tree. Blue elements are the branches, while light blue, white, orange and red elements are the bifurcation.

$$R = \frac{8\mu L}{\pi r^4} \tag{3.6}$$

JSON files contain four main information: simulations parameter, vessels, junctions and BCs. Vessels are identified by name and IDs and they are characterized by a resistance, length and, if terminal, a BC; junctions are identified by their name and they are characterized by junction type, IDs of inlet and outlet vessels, their interface surfaces and tangents and the lengths connecting the inlet to each outlet. Arbitrary names are assigned to the BCs, which are described by type (e.g. FLOW for flow rates, RESISTANCE for terminal resistances) and values (e.g. for FLOW BCs, the time period and the flow rate curve must be defined, while for RESISTANCEs resistance value and distal pressure must be specified). svZeroDSolver is not programmed to solve steady simulations, so the steady state was enforced by the application of a constant flow rate curve for two timesteps describing a unitary cardiac cycle.

Preliminary outlet BCs definition was performed by using the state-of-the-art method [131] presented in CFD models paragraph (subchapter 2.1.3): outlet flow rate in the DAo was estimated directly from the 4DFlow MRI data. Specifically, the mean velocities on two slices, one located in the middle of the DAo and one at the DAo outlet, was computed and converted into flow rates; the final DAo outlet flow rate was taken as the average of these two values. For the supra-aortic branches, 4DFlow MRI measurements were not available. Therefore, their flow rates were prescribed using an area-based split at the bifurcation: the total flow was distributed among the branch outlets in proportion to each outlet's cross-sectional area, as described in Equation (3.7). This assumption is a consequence of the resistance partition reported in Equation (3.8), and had been applied to the aortic models studied in the MSc Thesis of Polimi alumnus Valentina Scarponi [160] and to some SV examples [159].

$$\overline{Q}_i = \frac{A_i}{\sum_k A_k} \overline{Q}_{tot} \tag{3.7}$$

$$R_i = \frac{\sum_k A_k}{A_i} R_{tot} \tag{3.8}$$

For each patient, a 3D steady simulation was carried out using a plug inlet velocity profile prescribed to match the mean flow rate measured by 4DFlow MRI, together with preliminary outlet BCs. The internal parameters of the LPM circuit were first tuned to match the cap pressures predicted by the 3D simulation. The circuit was then refined to update the outlet BCs to (i) achieve the desired flow split among outlets and (ii) bring the simulated inlet pressure into agreement with the MAP. Internal circuit calibration was obtained by an iterative process involving the use of linear least-squares algorithm with Tikhonov regularization for each iteration. This method could allow to modify the internal resistances with the nearest-to-1 possible multiplication coefficient, without drastically increasing or decreasing the internal resistance of a vessel. Another iterative process was adopted for outlet BCs optimization, relying on the Limited-memory Broyden–Fletcher–Goldfarb–Shanno with bound constraints (L-BFGS-B) algorithm. This method allowed to minimize the squared error between current and target inlet pressure. Adjustment of flow split, performed after the inlet pressure optimization for each iteration, was obtained by the inverse proportionality of flow rate and resistance with respect to a constant difference of pressure, as reported in the Equations (3.9) and (3.10). The ratio between the target and simulated flow rate, reported in Equation (3.11), was inverted to calibrate the resistance, as it can be observed in Equation (3.12).

$$\Delta \mathrm{P} = \mathrm{Q} \cdot \mathrm{R} \tag{3.9}$$

$$\mathrm{Q_{target}} \cdot \mathrm{R_{target}} = \mathrm{Q_{sim}} \cdot \mathrm{R_{sim}} \tag{3.10}$$

$$\frac{\mathrm{Q_{target}}}{\mathrm{Q_{sim}}} = \frac{\mathrm{R_{sim}}}{\mathrm{R_{target}}} = \mathrm{k} \tag{3.11}$$

$$\frac{\mathrm{R_{target}}}{\mathrm{R_{sim}}} = \frac{1}{\mathrm{k}} \tag{3.12}$$

Physiological flow split for the vessels was defined by following real measurements or conventionally used percentages (Table 3.3). DAo, BCT, LCCA, LSVA trunks and coronary arteries flow rate represent 69%, 15.4%, 3.9%, 7.7% and 4% of inlet flow rate, respectively [161]. However, coronary arteries flow percentage was excluded, rescaling the others to obtain a sum of 100%. BCT branches into the right common carotid artery and the right proximal subclavian artery. The known percentages for LCCA and LSVA were similarly rescaled to obtain a sum of 100%: then, right common carotid and right proximal subclavian arteries receive 34% and 66% of the BCT flow rate, respectively. Proximal subclavian arteries further bifurcate into vertebral and distal subclavian arteries: a mean flow rate of 51mL/min [162] for the left vertebral artery and a baseline mean flow rate of 355mL/min [163] for the LSVA were measured, and it was assumed the remaining 304mL/min entering the distal subclavian artery. Therefore, it was inferred that, for both sides, vertebral and distal subclavian arteries receive 14% and 86% of parent branch flow rate respectively. For every model except 3A, common carotid arteries branch into the internal and external carotid arteries. Previous studies had assumed mean flow rates of 4.5mL/s and 1.5mL/s for internal and external respectively, and 6mL/s for the common carotid artery [136]. Therefore, the internal and external carotid arteries receive 75% and 25% of common carotid flow rate, maintaining this percentages for both sides. After determining the final outlet resistances, RCR parameters were defined. State-of-the-art formulas [131] were applied only for the DAo, while supra-aortic vessels parameters were obtained by considering their normalized values (Table 3.4) and conversion to absolute values proposed by Tricarico et al. non-invasive estimation [164], reported in the Equation (3.13).

Table 3.3: Percentages of blood flow rate through each model branch computed with the considered assumptions. Vessel names are the same of LPM network reported in Figure 3.9.

AAo	**BCT**	**LCCA**	**LSVA**	**DAo**
100%	16.0%	4.1%	8.0%	71.9%
RSVA	**RCCA**	**LECA**	**LICA**	**LSA**
10.7%	5.39%	1.02%	3.05%	6.90%
LVA	**RECA**	**RICA**	**RSA**	**RVA**
1.12%	1.35%	4.05%	9.16%	1.49%

Table 3.4. Normalized values for the 3-EWKM of supra-aortic outlets.

	$\mathbf{R_p}$	**C**	$\mathbf{R_d}$
Carotid arteries	0.1	0.46	0.9
Subclavian arteries	0.03	1.91	0.97
Vertebral arteries	0.18	0.47	0.82

$$R_p = R_{p,norm} \cdot R_{tot} \quad R_d = R_{d,norm} \cdot R_{tot} \quad C = \frac{C_{norm} \cdot T}{R_{tot}} \tag{3.13}$$

Final 3-EWKM parameters are reported in the Appendix B: tables (Table 7.1).

3.4. CFD Simulations

CFD simulations were performed using SimVascular FSI (svFSI), an open-source command-line software for fluid dynamic, electromechanical and FSI analyses of cardiovascular models. This software can perform simulations on externally generated meshes and with externally generated BCs by writing an input file (.inp) containing simulation and equation parameters, mesh volume and surfaces file paths and BCs values or file paths [165]. Simulations were performed using Polimi Cluster, a High-Performance Computing (HPC) system capable of performing CFD simulations. The mesh surface extraction was performed in Python, where also IDs were assigned to facilitate the recognition of points and cells during the simulation. The code main steps are shown in Algorithm 4.

Algorithm 4: IDs assignation and mesh surface extraction

```
1:  Reading of the VTU file
2:  Assignement of the GlobalNodeID to each point and the GlobalElementID and ModelRegionID to each cell
3:  Computation of surface cells normals
4:  Distinction of inlet and outlet surface by considering similar normals and connectivity
5:  Wall isolation
6:  Saving of the surfaces as VTP files
```

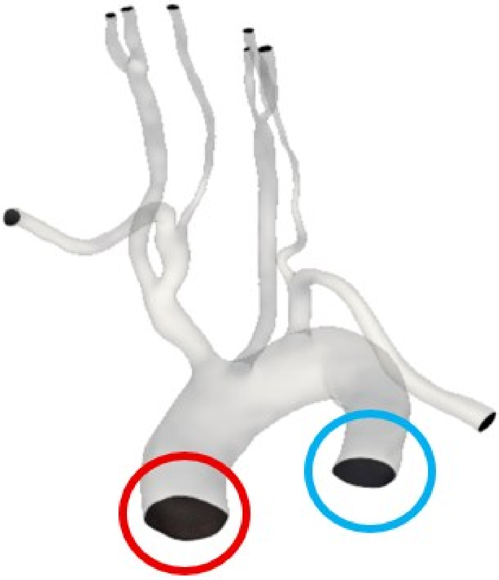

Figure 3.11: surface distinction. Black surfaces are the caps, while the white transparent surface is the wall. The red-circled black surface is the AAo section, where inlet BC was applied. Outlet BCs are applied to DAo section (blue-circled surface) and supra-aortic caps (non-circled surfaces).

Two simulations per AoArch model were executed, one for each inlet velocity profile considered as BC. Time step equal to 1ms was chosen to balance the reduced dimensions of the elements of supra-aortic vessels with respect to the characteristic edge length of Stentella's meshes [148], resulting in lower-than-1 CFL coefficients.

4DFlow profile inlet BC was generated during the BCs definition phase (Algorithm 2) as a single VTP file containing the velocity distribution for each timestep, while plug profile inlet BC was defined as a text file including flow rate values for each timestep. Both their file path must be reported in the input file to make svFSI read them and, for the idealized profile, the shape must be specified in the BC block. Wall displacement and RCR parameters for wall and outlet BCs are specified in the corresponding BC blocks.

The NS equation was added to the input file as "fluid" and solved with the assumptions of blood as Newtonian and incompressible fluid, so density and viscosity, respectively $0.00106\mathrm{g/mm^3}$ and $0.004\mathrm{Pa \cdot s}$, were set as constants. svFSI solves a stabilized weak form of NS FEM problem [166], providing an iterative solution of each timestep. The number of iterations can be set by the user: for this study, a minimum of 3 and a maximum of 20 iterations were set. The solver passes to the following timestep when the current timestep residual, i.e. the local error of the solution, is lower than a tolerance threshold, set as 10^{-3}. The proposed spatial and temporal discretization had made all the timesteps work for 3-4 iterations, confirming the goodness of the simulation definition. CFD results were saved every 5 timesteps, so one saved instant and the following are separated by a timespan of 5ms.

CFD results of the third cardiac cycle, chosen because of its best solution stability, were validated with respect to 4DFlow imaging velocity data computing the Mean Absolute Error (MAE), Root Mean Squared Error (RMSE) and Pearson correlation coefficient. A qualitative comparison of velocity colour maps, vectorial fields was carried out, and the comparison of pressure and flow rate trends obtained by 4DFlow and plug profile simulations were further qualitatively compared.

3.5. PT analyses

CFD simulation results were post-processed with a PT analysis, performed with FlowVC, a LPT code developed in the Shadden Lab of University of California, Berkeley [167]. LPT is performed with the numerical approximation of Maxey-Riley show in Equation (3.14), where $\mathbf{v}(\mathbf{x}(t))$ is the particle velocity, $\mathbf{u}(\mathbf{x},t)$ the fluid velocity, $\mathbf{g}$ the gravitational acceleration, a the particle radius, μ the fluid viscosity, ρ_p and ρ_f the densities of particle and fluid respectively and $\mathbf{x}(t)$ represents the particle's position.

$$\begin{aligned}\left(\rho_p + \frac{1}{2}\rho_f\right)\frac{d\mathbf{v}(\mathbf{x}(t))}{dt} = \\ = (\rho_p - \rho_f)\mathbf{g} + \frac{3}{2}\rho_f\frac{D\mathbf{u}(\mathbf{x},t)}{Dt} - \frac{9}{2}\frac{\mu}{a^2}\big(\mathbf{v}(\mathbf{x}(t)) - \mathbf{u}(\mathbf{x},t)\big)\end{aligned} \tag{3.14}$$

For each CFD simulations, four density and three characteristic dimensions were considered. The chosen densities were $1.45\mathrm{g/cm^3}$, $1.22\mathrm{g/cm^3}$, $1.06\mathrm{g/cm^3}$ and $0.8\mathrm{g/cm^3}$, respectively representing calcific and fibrous plaque debris [168], thrombotic particles [169] and lipid or necrotic debris given by the disruption of atheromatous plaques [149]. The three dimensions considered were 325μm (small), 750μm (medium) and 1250μm (large), taken from the mean value between the upper and lower bounds of the intervals considered by Schmidt et al. [170]: in the study, small particles were defined for the dimensional interval of $150 - 500\mu m$, medium particles for $500 - 1000\mu m$ and large particles for $> 1000\mu m$. The highest dimension for large particles limiting the dimensional interval is assumed to be 1500μm to maintain a similar range wideness. 125 small particles, 27 medium particles and 8 big particles are tracked for each CFD simulation. These counts were defined as the perfect cube included between the third quartile and the maximum value of the upper whisker for the Lotus valve, the most debris-releasing valve, based on the box plots analysis reported by Schmidt et al. [170]. The seeds were defined as cubes of dimension 12mm and centre located on the CL 15mm far from the inlet surface (Figure 3.12).

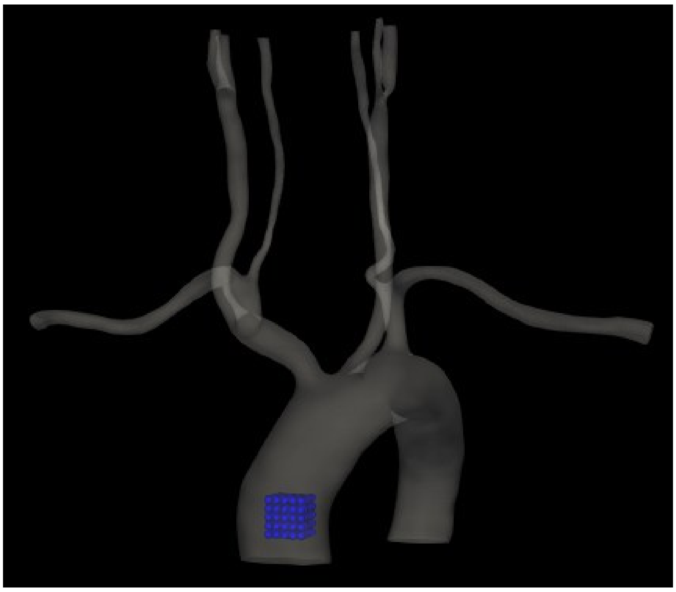

Figure 3.12: 5: Region defined to seed debris particles in the AAo (blue).

FlowVC is programmed in C++ and uses binary files (.bin) to describe the model velocity field and particles, so the velocity field and the mesh connectivity, adjacency and point coordinates must be input as binary files. However, for the visualization in software like Paraview, an extension called “bin2vtk” is provided with the program to convert the output binary files into VTK. Particles trajectories are computed for the entire cardiac cycle, neglecting the particles interaction, e.g. potential collisions, and velocity field was integrated with a time step of 20ms. Twenty particle positions had been saved for each PT analysis.

For each PT analysis, the percentage of particles going through supra-aortic vessels or remaining in the AoArch was computed to analyse the influence of AoArch type and density on cardiogenic embolic stroke risk. Both these analyses results were compared for the two different CFD inlet profile.

4 Results

This chapter reports the salient quantitative and qualitative results of the study. Results are reported in this order: MSA, CFD model validation and PT analysis. PT and CFD results were compared between the two simulation strategies.

4.1. Mesh Sensitivity Analysis

Mean and maximum velocity trend with respect to the elements number for AAo slice and LSVA slice are reported in Figure 4.1. It can be observed that these parameters presented a trend characterized by a progressive lowering of the percentual difference, which drops of one magnitude order from the coarse-to-medium refinement to the medium-to-fine refinement: this trend is globally observable and more recognizable for AAo mean velocity (Figure 4.1A2) and both the LSVA plots (Figure 4.1B1, Figure 4.1B2). GCI and k for each parameter are reported in Table 4.1. The GCI highest values are observable for maximum velocity of the AAo section ($\mathrm{GCI} = 0.14 - 0.25$), while the other values are one or two magnitude order lower. k coefficient is near to 1 ($k = 0.96 \div 0.99$): knowing that equal-to-1 k coefficient means the reaching of the asymptotic convergence, the parameters appeared to be close to it. The general goodness of MSA results ensured the possibility to use the medium mesh configuration (Table 3.2), representing the configuration that can ensure a good accuracy without much elongating the computational time. MSA results for mean and maximum pressure are reported in the Appendix A (Figure 6.1) and B (Table 7.2), and they are characterized by similar trend.

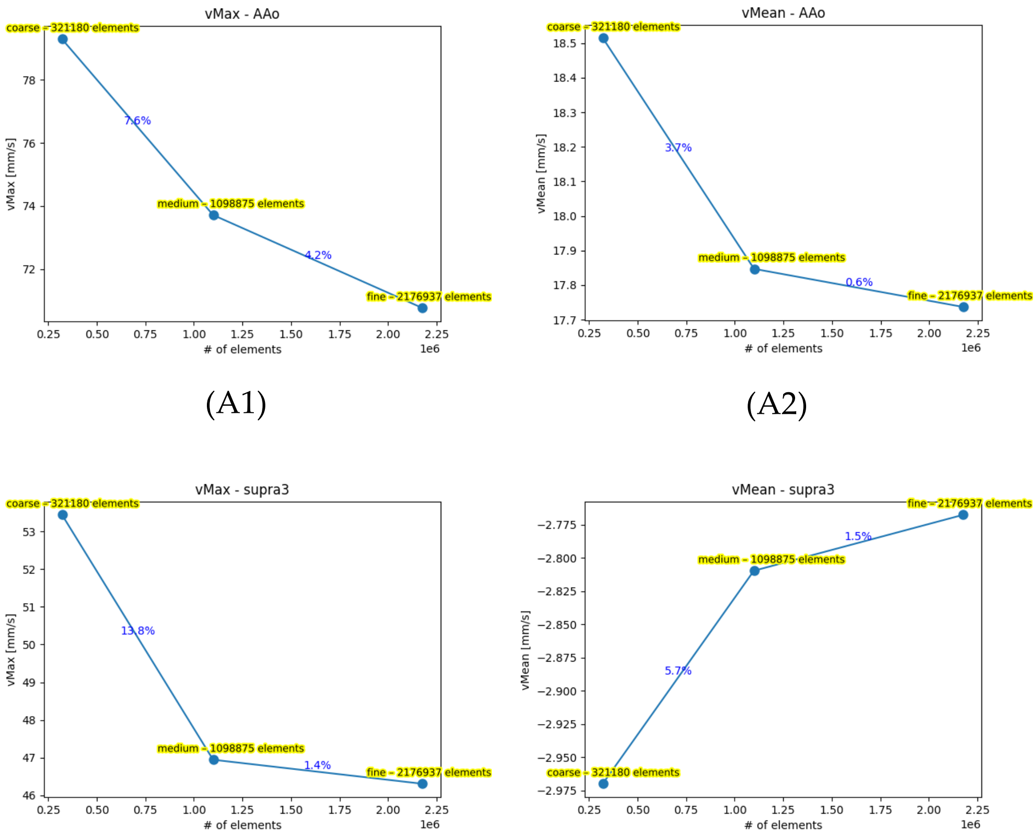

(A1) (A2)

(B1) (B2)

Figure 4.1: velocity plots with percentual differences trend with respect to the number of elements for AAo (A) and LSVA (supra3) (B). Figures 1 show the maximum velocity trend, while figures 2 the mean velocity trend.

Table 4.1: GCI and k computed for every parameter of the AAo and third supra-aortic artery (LSVA). $GCI_{1,2}$ is the medium-to-fine GCI, $GCI_{2,3}$ is the coarse-to-medium GCI, k is the index representing how close the mesh is to the asymptotic range.

$\mathbf{v_{Max}}$	**AAo**	**Supra3**	$\mathbf{v_{Mean}}$	**AAo**	**Supra3**
$\mathbf{GCI_{1,2}}$	0.140	0.005	$\mathbf{GCI_{1,2}}$	0.004	0.016
$\mathbf{GCI_{2,3}}$	0.255	0.045	$\mathbf{GCI_{2,3}}$	0.022	0.061
$\boldsymbol{k}$	0.960	0.986	$\boldsymbol{k}$	0.994	0.985

4.2. Validation of CFD results

In Table 4.2, flow split percentages with respect to the mean flow rate is compared between the two simulation modalities; target values are reported in Table 4.3. Target flow split appears to be correctly reproduced among the five anatomies, in particular for supra-aortic arteries, where values are really close to the target values ($\Delta < 1\%$ of the total mean flow rate), while higher but acceptable differences are observable for DAo percentages ($\Delta = 2 \div 5\%$ of the total mean flow rate), confirming the feasibility and the overall goodness of steady flow split calibration with LPM models.

Table 4.2: mean flow rate flow split computed for each patient and simulation modality (4DF: 4DFlow, Plug: plug). Patient 16 LCCA and RCCA percentages are reported within the ECA and ICA rows. Target percentages for the comparison are reported in Table 4.3.

Outlets	**1A 4DF [%]**	**1A Plug [%]**	**2A 4DF [%]**	**2A Plug [%]**	**1B 4DF [%]**	**1B Plug [%]**	**3B 4DF [%]**	**3B Plug [%]**	**3A 4DF [%]**	**3A Plug [%]**
DAo	74.1	74.2	75.2	75.2	74.0	74.0	74.1	74.1	76.6	76.7
LECA	0.92	0.92	0.90	0.90	0.93	0.93	0.98	0.98	3.30	3.30
LICA	2.77	2.77	2.69	2.69	2.79	2.79	2.29	2.29		
LSA	6.40	6.41	6.19	6.19	6.41	6.41	6.54	6.54	6.11	6.12
LVA	1.01	1.02	0.69	0.69	1.01	1.01	1.02	1.02	0.88	0.88
RECA	1.28	1.28	1.19	1.19	1.24	1.24	1.27	1.27	4.35	4.34
RICA	3.69	3.68	3.58	3.57	3.70	3.70	3.74	3.74		
RSA	8.55	8.52	8.26	8.25	8.60	8.60	8.67	8.66	7.55	7.54
RVA	1.24	1.23	1.28	1.28	1.34	1.34	1.38	1.38	1.16	1.16

Table 4.3: target flow split for each outlet for the comparison term with Table 4.2 results. Target percentages for LCCA and RCCA are the sum of respective ICA and ECA percentages.

	DAo	**LECA**	**LICA**	**LSA**	**LVA**	**RECA**	**RICA**	**RSA**	**RVA**
$\%_{target}$ **[%]**	71.9	1.02	3.05	6.90	1.12	1.35	4.05	9.16	1.49

Pressure difference from the AAo inlet to the DAo outlet is computed along the entire cardiac cycle and compared between the two simulation modalities in Figure 4.2, where maximum ΔP for each anatomy is reported (Figure 4.2B) and the extended curve for patient 1B is reported (Figure 4.2A). The pressure difference trend along the entire cardiac cycle appears to be almost equal, showing an absolute maximum peak in the first quarter of the period: a good agreement in terms of maximum pressure difference is observed for each patient, especially for 1A, 1B and 3A, where the values couple are almost the same. Only patient 2A and 3B manifested a more different pressure difference if comparing the two inlet profiles. However, the difference between them is about $2-3$mmHg, so physically tolerable. Plug profile appears to produce slightly higher differences of pressure.

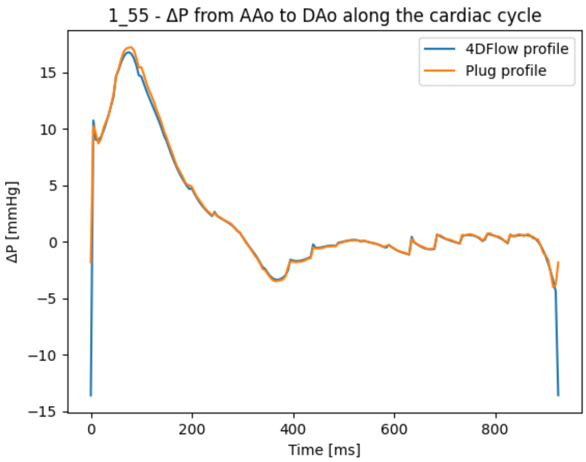

(A)

ΔP_{max} [mmHg]	4DFlow	Plug
1A	11.8	12.2
1B	16.8	17.3
2A	17.3	21.0
3A	17.0	17.4
3B	20.0	22.1

(B)

Figure 4.2: comparison of the pressure difference [mmHg] from the inlet to the DAo outlet of patient 1B between the two simulation strategies (A) and maximum ΔP values for each patient and simulation strategy (B).

CFD-based and 4DFlow-based velocity fields for each part of the AoArch are reported for each patient during peak systole to give a qualitative overview of velocity patterns (Figure 4.3, Figure 4.4, Figure 4.5, Figure 4.6, Figure 4.7). A good agreement in terms of velocity patterns, e.g. high-velocity regions representation, can be observed especially for DAo slice (green coloured) and similarities can be observed also in regions with high haemodynamic disturbances, e.g. within the AoArch (blue slice) or at the isthmus (black slice). The only difference is observable on the velocity magnitude colour maps, where CFD simulations presented a general overestimation of the velocity field, with difference of maximum $100-300$mm/s $= 10-30$cm/s. This result suggests that, despite the good fluid dynamic pattern reconstruction, patients may not exhibit the assumed physiological flow split or the not correct reproduction of physiological flow split. Patient 3B (Figure 4.7) appears to be patient with the most globally similar velocity maps. For the other models, the best visual agreement is observed in the DAo slice, while the worst visual concordance where observable in the in AAo slice, probably because of a not fully developed flow in this region, and in the isthmus. The punctual velocity difference has effects on the mean velocity curves (Figure 4.8): for every slice except the AAo (Figure 4.8A), despite the good reproduction of systolic and diastolic phases, a difference of $100 - 300\text{mm/s} = 10 - 30\text{cm/s}$ in the peak values is observable, confirming the velocity overestimation obtained by the simulations, especially in the isthmus region (Figure 4.8C). Similar outcomes are observed for the other mean velocity curves, reported in the Appendix A: figures (Section 6.2). Observing the velocity vector representation (Figure 4.9), velocity direction of simulation results are coherent with the 4DFlow data, despite a lower 4DFlow data vector length in the AoArch, isthmus and DAo slices, which may be researched in the errors of flow split assumptions or reproduction. Influence of inlet velocity profile is clearer in the AAo, while progressively moving to the outlet, and so making the flow develop, differences progressively reduce, explaining the general good agreement of the results on the DAo slice.

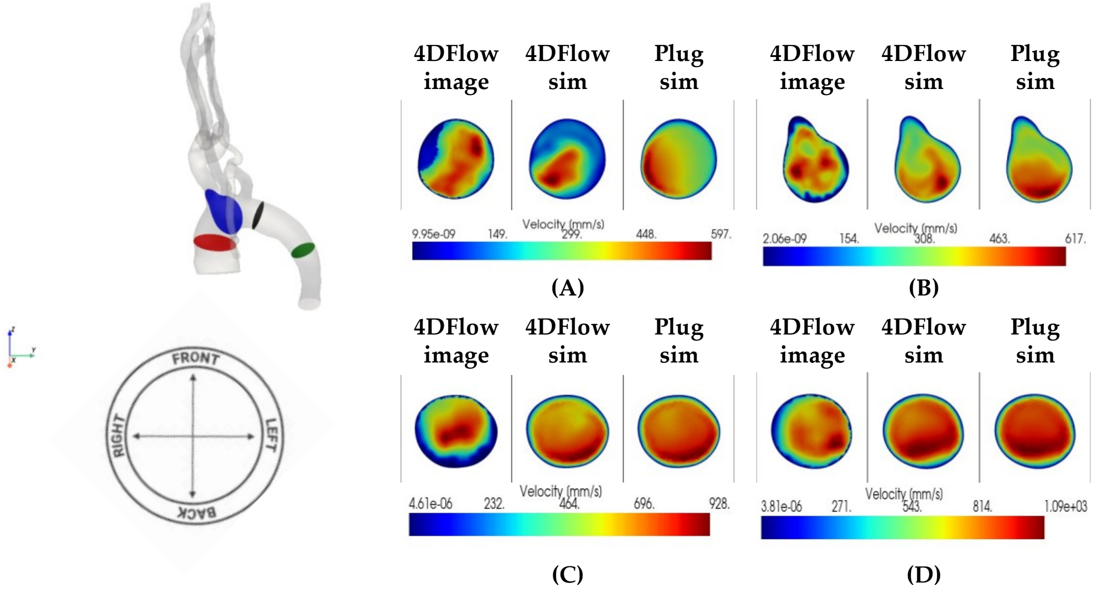

Figure 4.3: slices visualization for patient 1B. Top left: slices location (A: middle AAo - red, B: middle AoArch - blue, C: isthmus - black, D: middle DAo - green). Right: colour map comparison for each slice. Bottom left: direction map. Front and back directions are oriented towards the extrados and intrados, respectively.

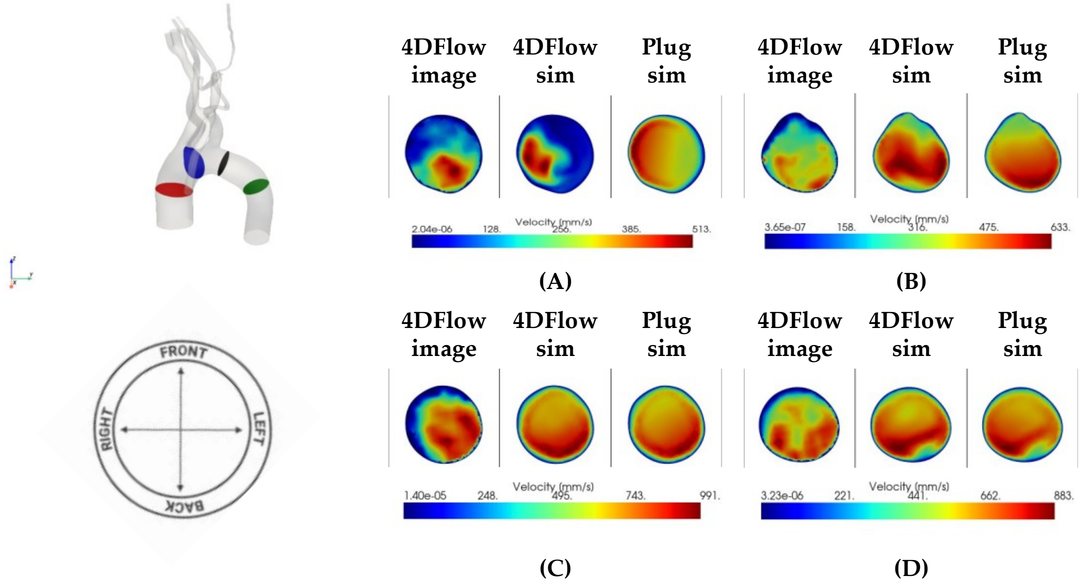

Figure 4.4: slices visualization for patient 1A. Top left: slices location (A: middle AAo - red, B: middle AoArch - blue, C: isthmus - black, D: middle DAo - green). Right: color map comparison for each slice. Bottom left: direction map. Front and back directions are oriented towards the extrados and intrados, respectively.

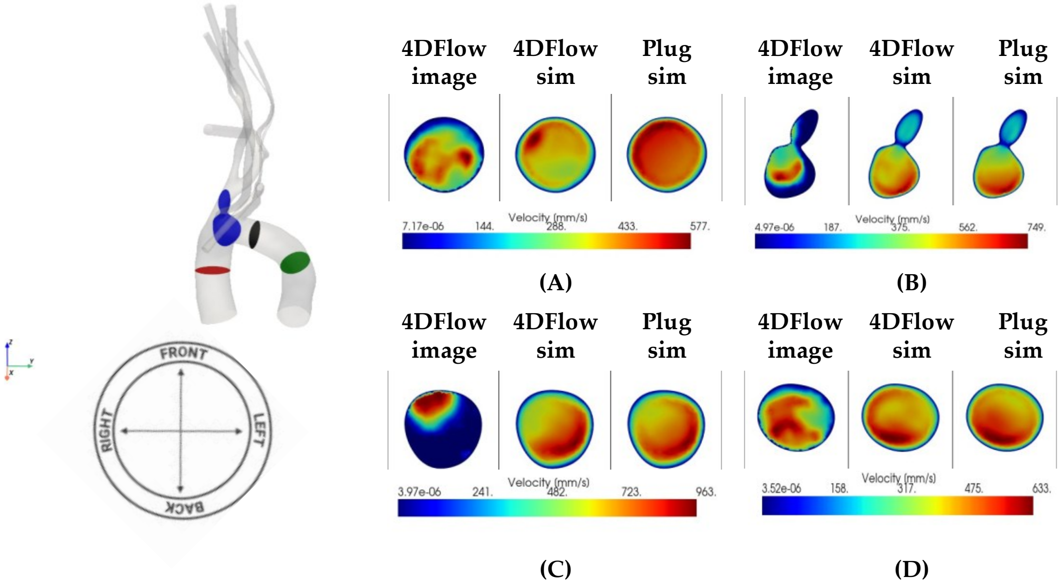

Figure 4.5: slices visualization for patient 2A. Top left: slices location (A: middle AAo - red, B: middle AoArch - blue, C: isthmus - black, D: middle DAo - green). Right: color map comparison for each slice. Bottom left: direction map. Front and back directions are oriented towards the extrados and intrados, respectively.

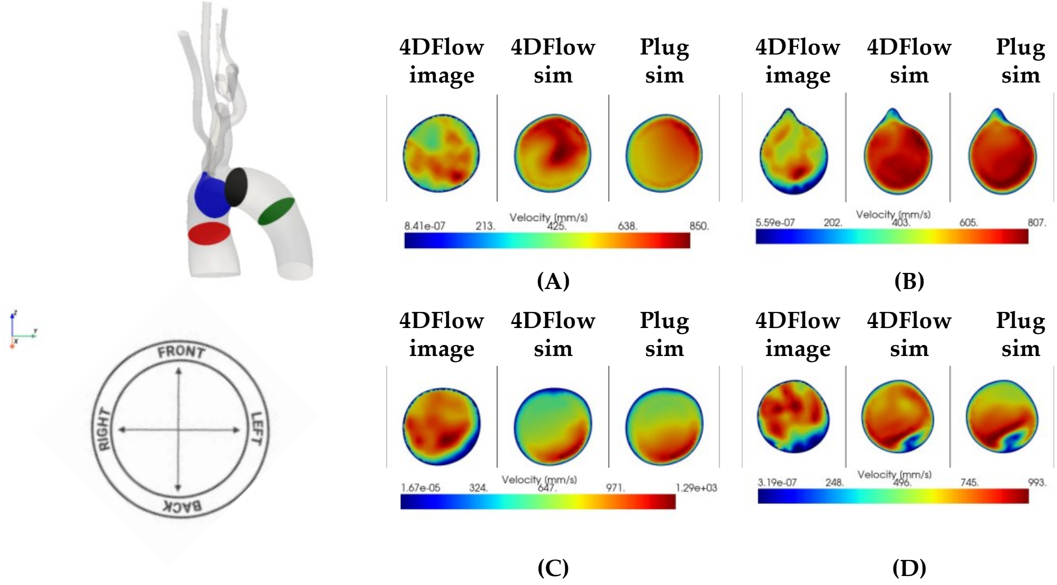

Figure 4.6: slices visualization for patient 3A. Top left: slices location (A: middle AAo - red, B: middle AoArch - blue, C: isthmus - black, D: middle DAo - green). Right: color map comparison for each slice. Bottom left: direction. Front and back directions are oriented towards the extrados and intrados, respectively.

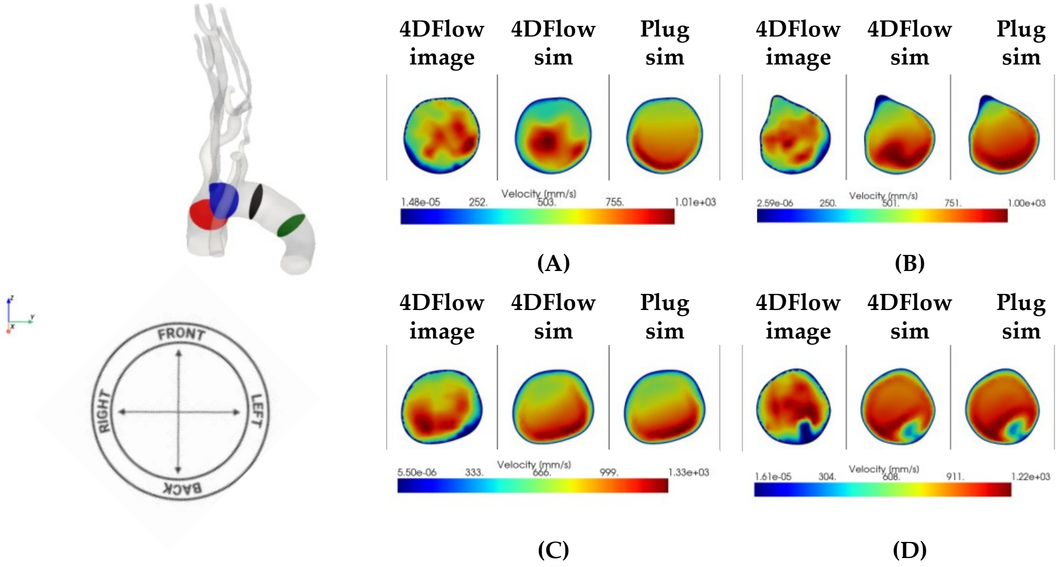

Figure 4.7: slices visualization for patient 3B. Top left: slices location (A: middle AAo - red, B: middle AoArch - blue, C: isthmus - black, D: middle DAo - green). Right: color map comparison for each slice. Bottom left: direction map. Front and back directions are oriented towards the extrados and intrados, respectively.

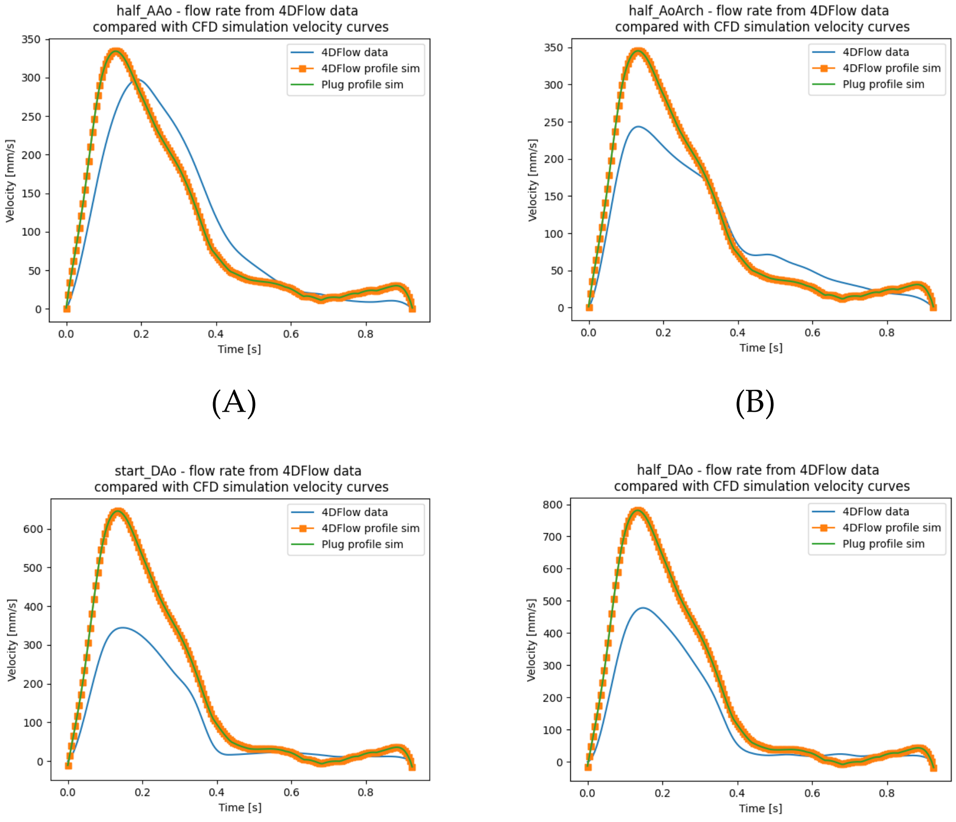

(A) (B)

(C) (D)

Figure 4.8: mean velocity curves from 4DFlow data (blue) and from CFD simulations (orange: 4DFlow profile, green: plug profile) comparison (patient 1B). Letters correspond to the slice viewable in Figure 4.3.

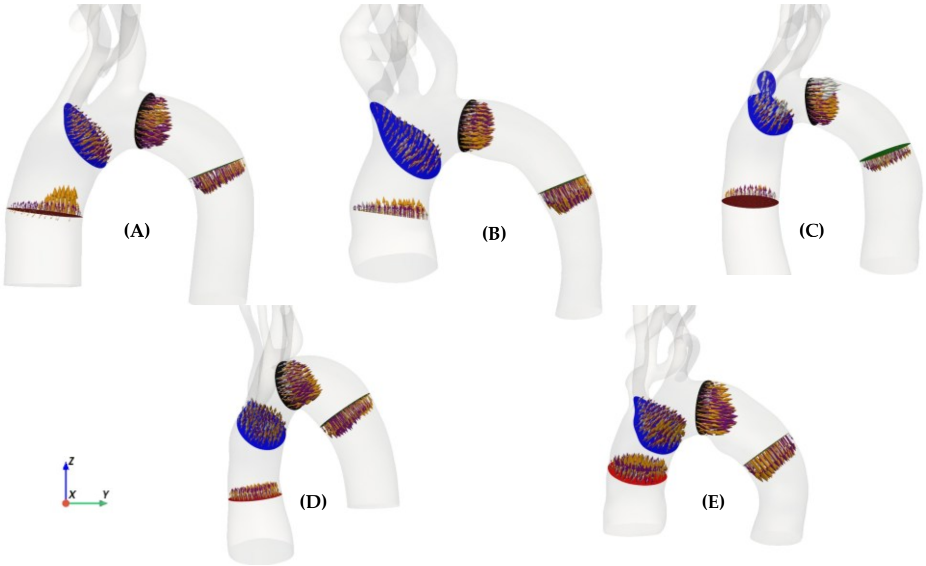

Figure 4.9: vectorial representation of velocity field for each model slice (red: middle AAo, blue: middle AoArch, black: isthmus, green: middle DAo) (A: 1A, B: 1B, C: 2A, D: 3A, E: 3B). White arrows are 4DFlow data velocities, orange arrows are 4DFlow simulation velocities and purple arrows are plug profile simulation velocities.

MAE, RMSE and Pearson correlation coefficient are computed for each patient (Table 4.4): an excellent correlation (r ~ 1) between simulation results for both the profiles and the 4DFlow data is observed. The lowest MAE and RMSE values are obtained for the AAo slice, while, knowing the complex haemodynamic phenomena occurring at the isthmus level, its errors are the highest. Patient 2A exhibits the lowest MAE values and, except for the isthmus slice, the lowest RMSE values: these coefficients are overall consistent with the MAE trend, despite higher due to the influence of the highest errors. DAo errors, as stated before, may be researched in the not sufficiently patient-specific flow split assumption or in its not perfect reproduction.

Table 4.4: MAE, RMSE and r (Pearson correlation coefficient) for each patient and simulation strategy (A: 4DFlow profile, B: plug profile). 1, 2, 3 and 4 are half-AAo, half-AoArch, isthmus and half-DAo results respectively.

A	$\mathbf{MAE_{4D}}$ **[mm/s]**				$\mathbf{RMSE_{4D}}$ **[mm/s]**				$\mathbf{r_{4D}}$ **[−]**			
	1	**2**	**3**	**4**	**1**	**2**	**3**	**4**	**1**	**2**	**3**	**4**
1A	44.8	72.5	124	89.4	56.4	101	169	144	0.99	0.98	0.99	0.97
1B	24.9	29.8	82.5	82.7	33.9	40.3	128	128	0.95	0.98	0.99	0.99
2A	14.2	35.3	88.6	38.6	15.8	45	145	59.9	1	1	0.98	0.95
3A	45.2	52.5	79.9	81.9	70.8	81.2	127	129	0.99	0.99	0.99	0.97
3B	44.2	64.3	70.8	71.1	72.2	108	137	125	0.99	0.99	0.99	0.98

B	$\mathbf{MAE_{PLUG}}$ **[mm/s]**				$\mathbf{RMSE_{PLUG}}$ **[mm/s]**				$\mathbf{r_{PLUG}}$ **[−]**			
	1	**2**	**3**	**4**	**1**	**2**	**3**	**4**	**1**	**2**	**3**	**4**
1A	44.7	72.7	124	90.1	56.3	102	170	145	0.99	0.98	0.99	0.97
1B	25	29.9	82.6	82.8	33.9	40.3	128	129	0.95	0.98	0.99	0.99
2A	14.2	35.4	88.7	38.6	15.8	45.1	146	60	1	1	0.98	0.95
3A	45.2	52.5	79.8	81.7	70.8	81.2	127	128	0.99	0.99	0.99	0.97
3B	44.2	64.5	71.1	71.4	72.1	108	137	125	0.99	0.99	0.99	0.98

The last figure (Figure 4.10), showing the comparison of the flow rate temporal variation and the pressure temporal variation during the cardiac cycle, represents another indicator of how much CFD results obtained with two different inlet velocity profile modelling are similar if not identical. Pressure is overall comprised into the physiological range ($80 - 120\text{mmHg} \sim 10.7 - 16\text{kPa}$), assessing the goodness of inlet pressure calibration.

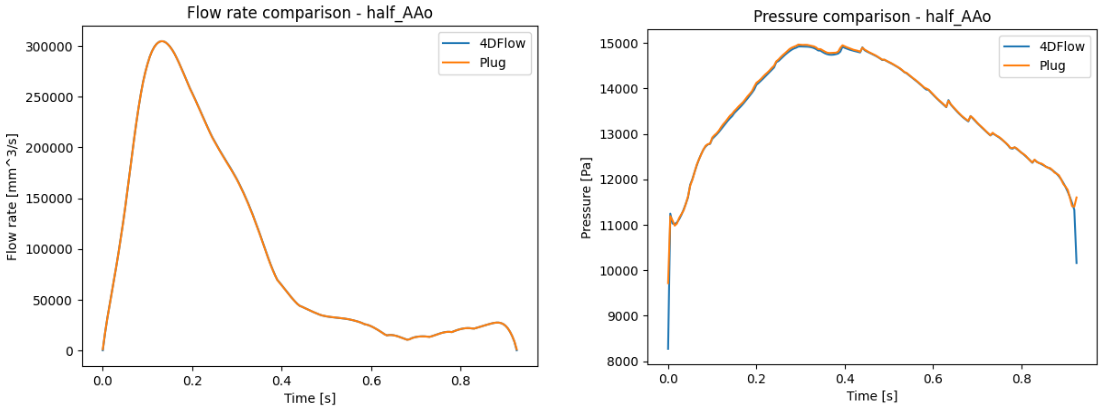

(A) (B)

Figure 4.10: flow rate and pressure comparison between 4DFlow (blue) and plug (orange) profile simulations for patient 1B (type I) in the middle of the AAo.

4.3. Particle Tracking analyses

Results from PT analyses are aimed to study the influence of the anatomical features and particles characteristics on the risk of cardiogenic embolic stroke, which can be assessed in terms of percentual number of particles reaching the supra-aortic vessels. As stated in the introduction of this chapter, results are compared between the two simulation strategies to find how the inlet profile influences the evaluation of how many particles reach the supra-aortic vessels.

4.3.1. AoArch type influence

Particles percentages comparison among the different anatomies are shown in Figure 4.11, where small thrombotic particles (seed of 125 particles with diameter of $325\mu\text{m}$ and density of 1.06g/cm^3) are located. Bar plots are reported to give an overview on the percentages, while values are reported in Table 4.5. The main vessels are the AoArch and the supra-aortic insertions, i.e. BCT, LCCA and LSVA, including their branches. The latter one is the entire left subclavian trunk, so both the left distal subclavian artery and the left vertebral artery are included. A qualitative overview of bar plots results for each anatomy is reported in Figure 4.12.

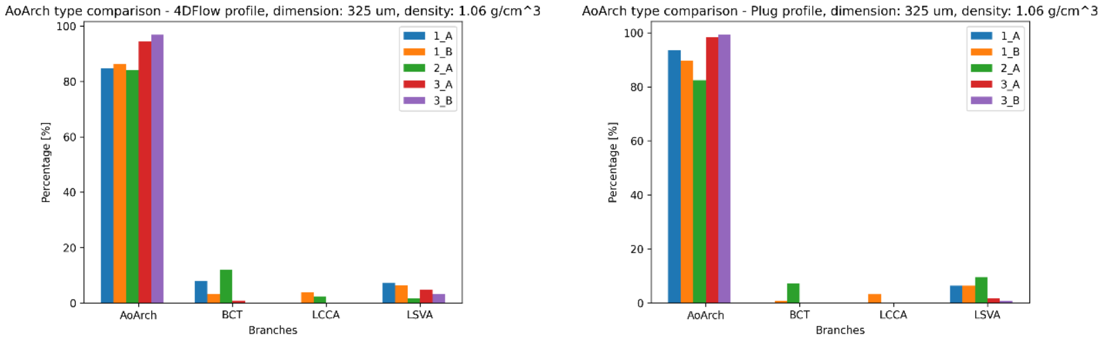

(A) (B)

Figure 4.11: AoArch type comparison for small thrombotic particles (dimension: 325µm, density: 1.06g/cm^3, total amount: 125) for 4DFlow (A) and plug simulations (B). Anatomies are codified as in Figure 3.3. Percentage values are reported in Table 4.5.

Table 4.5: arch-type-based comparison for percentual values of particles remaining in the AoArch or migrating to the supra-aortic vessels for the plots in Figure 4.11. Results for the two inlet profiles are compared. The total particle number is 125.

Patient	Profile	% AoArch	% BCT	% LCCA	% LSVA
1A	**4DFlow**	84,8	8	0	7,2
	Plug	93,6	0	0	6,4
1B	**4DFlow**	86,4	3,2	4	6,4
	Plug	89,6	0,8	3,2	6,4
2A	**4DFlow**	84	12	2,4	1,6
	Plug	82,4	7,2	0	9,6
3A	**4DFlow**	94,4	0,8	0	4,8
	Plug	98,4	0	0	1,6
3B	**4DFlow**	96,8	0	0	3,2
	Plug	99,2	0	0	0,8

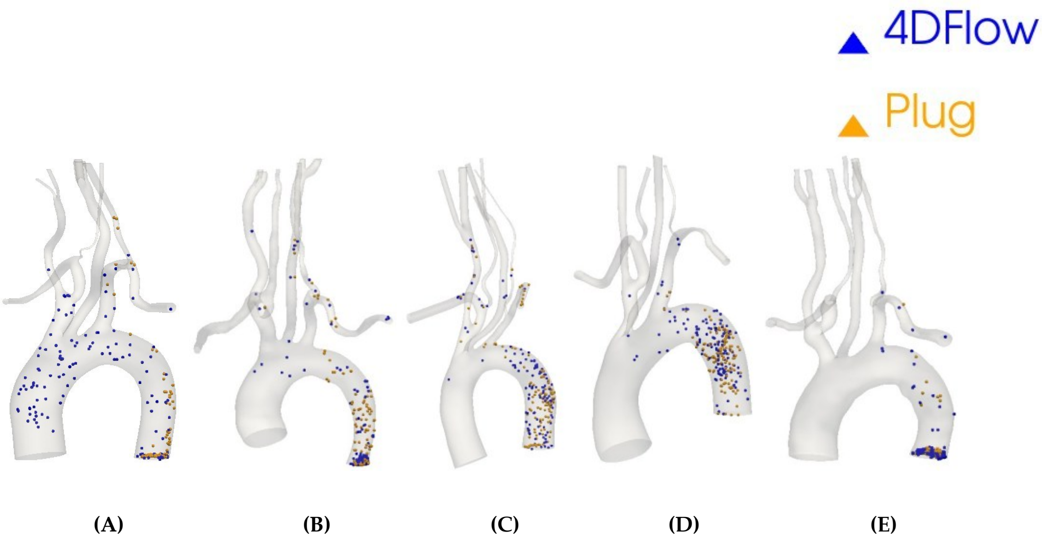

Figure 4.12: Qualitative overview of Figure 4.11 plots. Particle end position is represented in blue for 4DFlow profile and orange for plug profile. Figure A shows the patient 1A (type I), figure B patient 1B (type I), figure C patient 2A (type II), figure D patient 3A (type III) and figure E patient 3B (type III).

It is possible to observe that type II may be the AoArch type most prone to cardiogenic embolic stroke risk because of the lowest percentage of particles remaining in the AoArch ($< 85\%$), observing that particles moving to the supra-aortic arteries are principally settled in the BCT. No great difference is observed in terms of particle remaining in the AoArch between the 4DFlow simulation velocity field and the plug simulation velocity field (84% vs 82.4%), while plug profile appears to overestimate the particle percentage in the LSVA and underestimate particle percentage in the LCCA. Type III AoArch appears to be the least prone to CVE risk: in this case, particles percentage remaining in the AoArch is the highest among the three types ($> 94\%$) and the particles transported to the supra-aortic arteries are mainly concentrated in the LSVA. No great differences are visible for the two type III anatomies, and the only difference is determined by the higher percentage of particles transported to the LSVA by 4DFlow simulated velocity field, probably because of a better modelling of isthmus recirculation during the diastolic phase. Type I appears to be in the middle because of their percentual values of particles remaining in the arch, but results for the two anatomies of this type are interesting: patient 1B exhibited a particle split among the three supra-aortic vessels, which is visible for both the simulation, while patient 1A particle split did not involve the LCCA. Plug profile for type I AoArch appears to underestimate the BCT particles accumulation, but no other differences are visible for patient 1B, while for patient 1A particles accumulation in the AAo is clearly visible. Anatomical features of these two anatomies, e.g. the AAo shape or the supra-aortic vessels different course or higher tortuosity, which was observable for patient 1A LCCA, could have led to different PT results and different outcomes in testing the plug profile.

4.3.2. Density influence

The bar plot for the comparison of different densities of small particles (125 particles, dimension 325µm) is reported in the Figure 4.13. As in the previous subchapter, values (Table 4.6) and a qualitative overview of particle ending position for each simulated density are reported (Figure 4.14). Despite a not clear monotonical increase with respect to the density increase, it is observable that higher density debris are more prone to remain in the AoArch, while lower density debris are more prone to be transported to the supra-aortic vessels: this result was expected because of the gravity effect, which had been modelled in the FlowVC algorithm. Trend is clearer for plug profile: it is possible that 4DFlow profile may have introduced complex haemodynamic effects influencing particle path independently on their density. However, percentages are very similar because density values are quite similar.

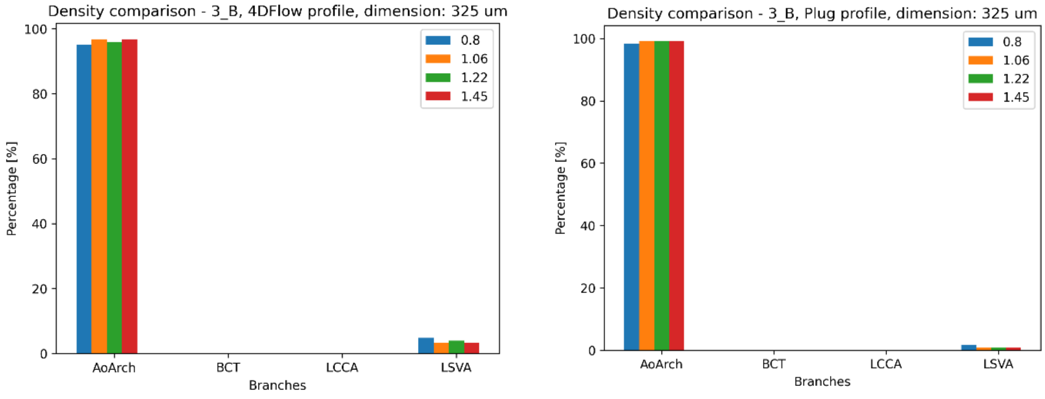

(A) (B)

Figure 4.13: density comparison for small particles (dimension: 325µm, total amount: 125) position in the patient 3B (type III arch) for 4DFlow (A) and plug simulation (B) results. Values are reported in Table 4.6.

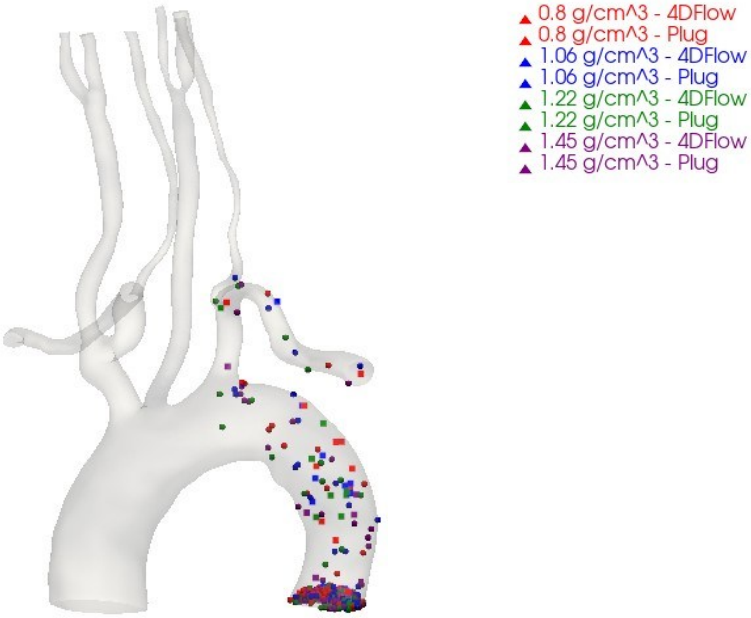

Figure 4.14: qualitative overview of Figure 4.13 plots. Simulated particles are small (dimension: 325µm, number: 125) and represent necrotic (red particles, 0.8g/cm^3), thrombotic (blue particles, 1.06g/cm^3), fibrous plaque (green, 1.22g/cm^3) and calcified plaque (purple, 1.45g/cm^3). 4DFlow simulation particles are spherical, while plug simulation particles are squared.

Table 4.6: density-based comparison for percentual values of particles remaining in the AoArch or migrating to the supra-aortic vessels for the plots in Figure 4.13. Results for the two inlet profiles are compared, and percentages are computed with respect to the total number of particles (125).

Density [g/cm^3]	Profile	% AoArch	% BCT	% LCCA	% LSVA
0.8	**4DFlow**	95,2	0	0	4,8
	Plug	98,4	0	0	1,6
1.06	**4DFlow**	96,8	0	0	3,2
	Plug	99,2	0	0	0,8
1.22	**4DFlow**	96	0	0	4
	Plug	99,2	0	0	0,8
1.45	**4DFlow**	96,8	0	0	3,2
	Plug	99,2	0	0	0,8

5 Conclusion

The final comments of the study are reported in this section. The achieved results, shown in the homonymous chapter, are discussed to define the conclusions of the work. The new relevant aspects of the study are summarized in the second subsection as starting points for the future developments, which are reported in the last paragraph.

5.1. Discussion on results and conclusions

MSA demonstrated the feasibility of introducing differentiating meshes configuration with the definition of coarser discretization regions and other finer regions. Despite the high errors for the AAo slice, the asymptotic convergence range has been reached. Lower errors for the LSVA slice confirmed the suitability of its finer discretization: this had been defined to increase the solution accuracy for the supra-aortic vessels, which represent the first embolization paths for particles originating from the AV.

CFD model validation results demonstrated the feasibility of another important aspect introduced in this work, the LPM calibration of outlet BCs. Differences in terms of resulted percentual values with respect to the target may be researchable in the impossibility of the LPM to be a perfect twin of the 3D model, although a reliable reduced-order representation can be obtained. Comparison between the two inlet profiles showed encouraging results for the application of an idealized profile instead of a patient-specific one. Haemodynamic patterns appeared to be similarly reproduced between the two simulation strategies, although differences are mainly observed in the AAo because of the not fully development of the flow. Comparison between CFD simulations and 4DFlow results confirm the goodness in terms of inlet BC definition and the strong correlation of simulated mean velocity trend with 4DFlow mean velocity data, although values were demonstrated to be quite different between simulation and patient-specific data in the DAo regions, influence by the not fully correct assumption or reproduction of physiological flow split for DAo. However, vectorial and velocity vectors comparison demonstrated the globally correct reproduction of haemodynamic patterns.

PT results confirmed the initial assumption of this study: the AoArch anatomical features might be a factor to be taken into account for the assessment of cardiogenic embolic stroke risk. Arch-type-dependent results may give an initial indication on the influence of this aspect to the CVE risk, but the introduction of another patient for the type I and type III arches highlighted the “patient-specific feature” factor: this was more viewable for type I arches, where percentage distribution and, surprisingly, particle distribution in the AoArch was different. Density influence suggests that not every particle can have the same behaviour, but it can vary basing on their characteristics. In this case, the inlet velocity profile had introduced some effects, which are researchable in the particle distribution among the supra-aortic vessels for the type I and type II anatomies or the potential backflow modelling made by the 4DFlow profile in the III anatomies. However, the global percentages of particles remaining in the AoArch and being transported to the supra-aortic vessels appeared to be generally very similar. 4DFlow profile is the gold-standard of this research because of its patient-specific measure, but plug had shown potentially good results in predicting how many particles are transported to the DAo or to all the three supra-aortic vessels.

It is concluded that cardiogenic embolic stroke risk may be influenced by more than one factor, e.g. the debris density or the AoArch anatomy. These outcomes reinforce the necessity to adopt a patient-specific TAVI planning to improve its safety. PT results, obtained as post-processing of CFD simulations, gave important clinical implications on the CVE risk, which appears to be the highest for type II AoArch and the lowest for type III, as confirmed by the previous work [148]. For every patient, the percentage of particles being transported to the LSVA appeared to be always different from zero and for some anatomies the highest, suggesting that it can be indicated as one of the most likely embolic pathways. However, the only clinically used device, the Sentinel®, covers only BCT and LCCA, lacking on LSVA protection (Figure 1.14A), suggesting that studying the most likely potential pathways is a fundamental aspect for TAVI-planning. CFD-based models demonstrated a great potential in terms of predicting haemodynamic patterns: the integration with a PT post-processing can make them become a tool for the risk assessment of many pathologies. The comparison between idealized and patient-specific profile did not exhibit great differences in CFD simulations and PT results were not affected in terms of how many particles remain in the AoArch or are transported through all the three supra-aortic vessels, suggesting the possibility to use the 4DFlow data only as a gold-standard for simulation results or even the possibility to estimate the patient-specific flow rate without this technology, to extend the model feasibility. This study, that involved the use of differentiated mesh and LPM, showed interesting outcomes for the optimization and the improvement of fluid dynamic analyses, suggesting new methods and innovation for cardiovascular modelling.

5.2. New relevant model innovation

Some interesting innovations have been introduced to improve the previous master's Thesis work [148]. They are briefly introduced in the previous subchapter to discuss on the results, but here they are summarized.

Differentiated mesh generation with CAD software: meshes are generated with the CAD software ANSA. Its potential is known in the biomedical engineering field, but it was further confirmed in this study: the mesh improvement is clear and confirmed by the MSA. ANSA gives also the possibility of writing scripts for the automatization of the mesh generation, allowing to define potentially infinite custom meshing pipelines.

Inlet velocity profile comparison: the blood flow velocity profile in the first segments of the TA changes along the cardiac cycle, while an idealized profile maintains its shape, changing only its values. A flat profile and a time-dependent profile from patient-specific 4DFlow imaging have been compared to verify the reasonability of idealizing the inlet profile instead of reconstructing it by the imaging sampling. Plug profile CFD and global PT results are proven to be generally similar to the 4DFlow profile results, suggesting that the model may be applied to centres without 4DFlow imaging.

LPM for outlet BCs definition: the state-of-the-art method appears to be reliable for great vessels like the DAo or the supra-aortic insertions, but it lacks on the 3-EWKM definition for smaller vessels like vertebral or carotid arteries. LPM calibration proposed in this work, which is based on pairing the 0D model with the 3D steady simulation results, is proved to be an interesting strategy that can be paired to the known methods to obtain the right modelling of smaller arteries. Despite the expectable differences between 3D and 0D results, the potential reproduction of every desired flow split is clear, introducing a fundamental improvement for state-of-the-art methods.

Realistic particles number for PT analysis: differently from Stentella's Thesis [148], particles number was much reduced basing on how many particles have been captured by the CPDs. This choice can give a more realistic estimation of debris released after the valve expansion during the TAVI procedure.

All these innovations, added to an inherently advanced model, made it possible to introduce or suggest model simplifications necessary to increase its accuracy or expand its usefulness. As already mentioned, 4DFlow MRI is not always available. Therefore, demonstrating the possible application of an inlet BC with ideal velocity profile and flow rate values obtained with more economical imaging techniques was a necessary step in model feasibility improvement.

5.3. Limitations and future development

Despite the interesting innovations, some limitations emerged from this work. Although reduced, the computational time is still too long to use this model as a real-time TAVI planning tool. It is suggested to explore ANSA potentialities to further optimize these models and to improve the efficiency of the differentiated mesh generation algorithm.

LPM calibration is an important tool to define customized BCs for 3D simulations, but, although the target flow split has been globally reproduced, it did not reproduce a patient-specific condition. It is suggested to integrate this new method with the state-of-the-art method [131], more reliable on the DAo and supra-aortic insertions, with the aim of adjusting the assumed flow split with patient-specific information. svZeroDSolver potentialities are suggested to be studied to provide a more accurate or also time-dependent calibration, to improve CFD simulation accuracy and reliability.

PT analyses can be further improved: the particles number had been estimated from how many particles had been captured by filters put in supra-aortic vessels. However, particles mainly originate from the AV so it is proposed to provide a particles number assumption based on the number of particles released during TAVI procedure, despite it may be difficult to estimate the particles number. Particles had been modelled as Lagrangian spheres, but debris may not be perfectly spherical, so another possible recommendation can be the enlargement of possible particle shapes.

The achievements that are shown in this study have given an initial indications on the morphology influence on the risk of cardiogenic embolic stroke and the possibility to assume idealized inlet profiles, but they must be confirmed, so it is suggested to expand the analysis to many other anatomies, introducing also odds branch patterns, e.g. the bovine AoArch. Dynamic region growing method is a simple technique, like the other manual segmentation methods, but it is much time-consuming, and it sometimes requires part-by-part reconstruction and continuous manual intervention: these weaknesses may be acceptable if few cases are segmented, but it is not suitable when more than three anatomies must be modelled. An automatic segmentation method can be introduced or developed to reconstruct AoArch models with extended supra-aortic branches, facilitating the increase of the patient cohort. The enlargement of the patient cohort is fundamental to define more comprehensive anatomical criteria for the patient-specific assessment of cardiogenic embolic stroke risk observing its AoArch imaging instead of performing much time-consuming CFD simulations. This is the long-term goal of the study, and this knowledge level will be reached by simulating more cases.

Bibliography

[1] A. Postolache, S. Sperlongano and P. Lancellotti, "TAVI after More Than 20 Years," *Journal of Clinical Medicine,* vol. 12, no. 17, p. 5645, 30 August 2023.

[2] T. Pilgrim and S. Windecker, "Expansion of transcatheter aortic valve implantation: new indications and socio-economic considerations," *European Heart Journal,* vol. 39, no. 28, pp. 2643-2645, 26 April 2018.

[3] S. Blankenberg, M. Seiffert, R. Vonthein, H. Baumgartner, S. Bleiziffer, M. A. Borger, Y.-H. Choi and et al., "Transcatheter or Surgical Treatment of Aortic-Valve Stenosis," *The New England Journal of Medicine,* vol. 390, no. 17, 8 April 2024.

[4] D. N. Nikas, "Stroke in Transcatheter Aortic Valve Implantation (TAVI): A Comprehensive Review," *Journal of Clinical Medicine,* vol. 14, no. 19, p. 6754, 24 September 2025.

[5] Y. Jobanputra, B. M. Jones, D. Mohananey, B. Fatima, K. Kandregula and S. R. Kapadia, "Cerebral protection devices for transcatheter aortic valve replacement," *Expert Review of Medical Devices,* vol. 14, no. 7, pp. 529-543, 13 July 2017.

[6] S. Voss, C. Campanella, M. Burri, T. Trenkwalder, K. Sideris, M. Erlebach, H. Ruge, M. Krane, K. Vitanova and R. Lange, "Anatomical reasons for failure of dual-filter cerebral embolic protection application in TAVR: A CT-based analysis," *Journal of Cardiac Surgery,* vol. 36, no. 12, pp. 4537-4545, 27 September 2021.

[7] V. H. Thourani, S. M. O'Brien, J. J. Kelly, D. J. Cohen, E. D. Peterson, M. J. Mack, D. M. Shahian, F. L. Grover, J. D. Carroll, J. M. Brennan, J. Forcillo, S. V. Arnold, S. Vemulapalli, S. Fitzgerald, D. R. Holmes, J. E. Bavaria and F. H. Edwards, "Development and Application of a Risk Prediction Model for In-Hospital Stroke After Transcatheter Aortic Valve Replacement – A Report from the Society of Thoracic Surgeons/American

College of Cardiology Transcatheter Valve Therapy Registry," *Annals of Thoracic Surgery,* vol. 107, no. 4, pp. 1097-1103, 7 December 2018.

[8] A. Berkovitch, A. Segev, E. Maor, A. Sedaghat, A. Finkelstein, M. Saccocci, R. Kornowski, A. Latib, J. M. De La Torre Hernandez, L. Søndergaard, D. Mylotte, N. Van Royen, A. G. Zaman, P. Robert, J.-M. Sinning, A. Steinvil, F. Maisano, K. Orvin, G. Iannopollo, D.-H. Lee, O. De Backer, F. Mercanti, K. van der Wulp, J. Shome, D. Tchétché and I. M. Barbash, "Clinical Predictors for Procedural Stroke and Implications for Embolic Protection Devices during TAVR: Results from the Multicenter Transcatheter Aortic Valve Replacement In-Hospital Stroke (TASK) Study," *Journal of Personalized Medicine,* vol. 12, no. 7, p. 1056, 28 June 2022.

[9] M. Foley, K. Hall, J. P. Howard, Y. Ahmad, M. Gandhi, S. Mahboobani, J. Okarof, H. Rahman, N. Hadjiloizou, N. Ruparelia, G. Mikhail, I. Malik, G. Kanaganayagam, N. Sutaria, B. Rana, B. Ariff, E. Barden, J. Anderson, J. Afoke, R. Petraco, R. Al-Lamee and S. Sen, "Aortic Valve Calcium Score Is Associated With Acute Stroke in Transcatheter Aortic Valve Replacement Patients," *Journal of the Society for Cardiovascular Angiography & Interventions,* vol. 1, no. 4, p. 100349, 12 May 2022.

[10] M. M. Marrocco-Trischitta and F. Sturla, "Blood flow helical pattern in type III arch configuration as a potential risk factor for type B aortic dissection," *European Journal of Cardio-Thoracic Surgery,* vol. 61, no. 1, pp. 132-139, 10 August 2021.

[11] C. R. T. di Gioia, A. Ascione, R. Carletti and C. Giordano, "Thoracic Aorta: Anatomy and Pathology," *Diagnostics (Basel),* vol. 13, no. 13, p. 2166, 25 June 2023.

[12] S. A. Alexander and G. D. Rubin, "Imaging the Thoracic Aorta: Anatomy, Technical Considerations, and Trauma," *Seminars in Roentgenology,* vol. 44, no. 1, pp. 8-15, 7 December 2008.

[13] D. A. Berdajs, "Aortic root morphology: a paradigm for successful reconstruction," *Interactive CardioVascular and Thoracic Surgery,* vol. 22, no. 1, pp. 85-91, 21 October 2015.

[14] D. Berdajs, S. Mosbahi, Z. Forro, C. Gerber, E. Ferrari, D. Charbonnier and L. K. von Segesser, "Numerical analysis of the 3-dimensional aortic root morphology during the cardiac cycle," *European Journal of Cardio-Thoracic Surgery,* vol. 49, no. 4, pp. 1213-1221, 9 September 2015.

[15] S.-B. Bae, E.-J. Kang, K.-S. Choo, J. Lee, S.-H. Kim, K.-J. Lim and H. Kwon, "Aortic Arch Variants and Anomalies: Embryology, Imaging Findings, and Clinical Considerations," *Journal of Cardiovascular Imaging,* vol. 30, no. 4, pp. 231-262, 2022.

[16] X. Wang, H. J. Carpenter, M. H. Ghayesh, A. Kotousov, A. C. Zander, M. Amabili and P. J. Psaltis, "A review on the biomechanical behaviour of the aorta," *Journal of the Mechanical Behavior of Biomedical Materials,* vol. 144, p. 105922, 13 June 2023.

[17] J. Jones, F. Deng, S. Hapugoda and e. al., "Thoracic aorta," *Radiopaedia.org,* 2 May 2008.

[18] J. Jones, A. Thurin, R. Sharma and et al., "Aortic isthmus," *Radiopaedia.org,* 29 September 2025.

[19] S. Iddawela, A. Ravendren and A. Harky, "Bio-chemo-mechanics of the thoracic aorta," *Vascular Biology,* vol. 3, no. 1, pp. R25-R33, 12 January 2021.

[20] J. Concannon, P. Dockery, A. Black, N. Hynes, P. E. McHugh, K. M. Moerman and J. P. McGarry, "Quantification of the regional bioarchitecture in the human aorta," *Journal of Anatomy,* vol. 236, no. 1, pp. 142-155, 2019.

[21] B. Mensel, A. Quadrat, T. Schneider, J.-P. Kühn, M. Dörr, H. Völzke, W. Lieb, K. Hegenscheid and R. Lorbeer, "MRI-based Determination of Reference Values of Thoracic Aortic Wall Thickness in a General Population," *European Radiology,* vol. 24, pp. 2038-2044, 2014.

[22] M. Myneni, R. L. Sridhar, K. R. Rajagopal and C. C. Benjamin, "Experimental Investigation of the Anisotropic Mechanical Response of the Porcine Thoracic Aorta," *Annals of Biomedical Engineering,* vol. 50, pp. 452-466, 28 February 2022.

[23] C. M. Garcia-Herrera, F. J. Rojo, G. Guinea and D. J. Celentano, "Mechanical behaviour and rupture of normal and pathological human ascending aortic wall," *Medical & Biological Engineering & Computing,* vol. 50, no. 6, pp. 559-566, June 2012.

[24] H. G. Bogren, R. H. Mohiaddin, P. J. Kilner, L. J. Jimenez-Borreguero, G. Z. Yang and D. N. Firmin, "Blood flow patterns in the thoracic aorta

studied with three-directional MR velocity mapping: The effects of age and coronary artery disease," *Journal of Magnetic Resonance Imaging,* vol. 7, no. 5, pp. 784-793, 17 November 2005.

[25] A. F. Stalder, A. Frydrychowicz, M. F. Russe, J. G. Korvink, J. Henning, K. Li and M. Markl, "Assessment of flow instabilities in the healthy aorta using flow-sensitive MRI," *Journal of Magnetic Resonance Imaging,* vol. 33, no. 4, pp. 839-846, 29 March 2011.

[26] Y. Weerakkody, L. Silverstone and S. Raymond Chieng, "Right-sided aortic arch," *Radiopaedia.org,* 22 December 2024.

[27] Y. Weerakkody, B. Rasuli and A. Murphy, "Double aortic arch," *Radiopaedia.org,* 29 May 2025.

[28] V. Tatco, H. Knipe and S. Hapugoda, "Cervical aortic arch," *Radiopaedia.org,* 27 June 2018.

[29] "Right Aortic Arch," Cleveland Clinic, [Online]. Available: https://my.clevelandclinic.org/health/diseases/right-aortic-arch.

[30] "Double Aortic Arch," Cleveland Clinic, 2022. [Online]. Available: https://my.clevelandclinic.org/health/diseases/23432-double-aortic-arch.

[31] D. D'Souza, C. Hacking and L. Silverstone, "Variant anatomy of the aortic arch," *Radiopaedia.org,* 2 May 2008.

[32] M. Lahlouh, Y. Chenoune, R. Blanc, J. Szewczyk and N. Passat, "Aortic arch anatomy characterization from MRA: A," *International Symposium on Biomedical Imaging (ISBI),* pp. 1-5, 16 January 2022.

[33] D. Kotelis, M. S. Bischoff, B. Jobst, H. von Tengg-Kobligk, U. Hinz, P. Geisbüsch and D. Böckler, "Morphological risk factors of stroke during thoracic," *Langenbeck's Archives of Surgery,* vol. 397, pp. 1267-1273, 8 September 2012.

[34] K. Natsis, M. Piagkou, N. Lazaridis, T. Kalamatianos, D. Chytas, D. Manatakis, N. Anastasopoulos and M. Loukas, "A systematic classification of the left-sided aortic arch variants based on cadaveric studies' prevalence," *Surgical and Radiologic Anatomy,* vol. 43, pp. 327-345, 2 January 2021.

[35] J. Dumfarth, A. S. Chou, B. A. Ziganshin, R. Bhandari, S. Peterss, M. Tranquilli, H. Mojibian, H. Fang, J. A. Rizzo and J. Elefteriades, “Atypical aortic arch branching variants: A novel marker for thoracic,” *The Journal of Thoracic and Cardiovascular Surgery,* vol. 149, no. 6, pp. 1586-1592, 6 June 2015.

[36] Z. R. Y. Celikyak, A. E. Koner, F. Celikyay, C. Denız, B. Acu and M. M. Firat, “Frequency and imaging findings of variations in human aortic arch anatomy based on multidetector computed tomography data,” *Clinical Imaging,* vol. 37, no. 6, pp. 1011-1019, 9 August 2013.

[37] M. Sidiq, E. Scheidecker, A. Potreck, U. Neuberger, C. S. Weyland, S. Mundiyanapurath, M. Bendszus, M. A. Möhlenbruch and F. Seker, “Aortic Arch Variations and Supra-aortic Arterial Tortuosity in Stroke Patients Undergoing Thrombectomy,” *Clinical Neuroradiology,* vol. 33, no. 1, pp. 49-56, 13 June 2022.

[38] C. M. Otto and B. Prendergast, “Aortic-Valve Stenosis — From Patients at Risk to Severe Valve Obstruction,” *The New England Journal of Medicine,* vol. 371, no. 8, pp. 744-756, 21 August 2014.

[39] S. H. Pujari and P. Agasthi, “Aortic Stenosis,” in *StatPearls*, 2023.

[40] R. Verma, G. Cohen, J. Colber and P. W. M. Fedak, “Bicuspid aortic valve associated aortopathy: 2022 guideline update,” *Current Opinion in Cardiology,* vol. 38, no. 2, pp. 61-67, 1 March 2023.

[41] A. P. Peng, A. A. Ferrando, W. Lee, J. P. Morris 4th, L. B. Silverman, C. Sanchez-Irizarry, S. C. Blacklow, A. T. Look and J. C. Aster, “Activating mutations of NOTCH1 in human T cell acute lymphoblastic leukemia,” *Science,* vol. 306, no. 5694, pp. 269-271, 8 October 2004.

[42] M. Banovic, L. Athithan and G. P. McCann, “Aortic stenosis and diabetes mellitus: An ominous combination,” *Diabetes & Vascular Disease Research,* vol. 16, no. 4, pp. 310-323, 9 January 2019.

[43] S. C. Larsson, A. Wolk and M. Bäck, “Alcohol consumption, cigarette smoking and incidence of aortic valve stenosis,” *Journal of Internal Medicine,* vol. 282, no. 4, pp. 332-339, 11 May 2017.

[44] C. T. Rice, S. Barnett, S. P. O'Connel, E. Akowuah, C. E. Appleby, J. B. Chambers, B. N. Shah and D. J. Blackman, “Impact of gender, ethnicity

and social deprivation on access to surgical or transcatheter aortic valve replacement in aortic stenosis: a retrospective database study in England," *Open Heart,* vol. 10, no. 2, p. e002373, 10 September 2023.

[45] O. A. Akinseye, A. Pathak and U. N. Ibebuogu, "Aortic Valve Regurgitation: A Comprehensive Review," *Current Problems in Cardiology,* vol. 43, no. 8, pp. 315-334, 10 July 2018.

[46] "Surgical Aortic Valve Replacement," Cleveland Clinic, [Online]. Available: https://my.clevelandclinic.org/health/treatments/25057-aortic-valve-replacement.

[47] C. Howard, L. Jullian, M. Joshi, A. Noshirwani, M. Bashir and A. Harky, "TAVI and the future of aortic valve replacement," *Journal of Cardiac Surgery,* vol. 34, no. 12, pp. 1577-1590, 10 October 2019.

[48] M. El-Mawardy, M. Abdel-Wahab and G. Richardt, "Transcatheter aortic valve implantation: Technique, complications and perspectives," *Expert Review of Cardiovascular Therapy,* vol. 12, no. 8, July 2014.

[49] J. Parmley, "TAVR Approaches," 2016. [Online]. Available: http://www.jessicaparmley.com/portfolio/medical-illustration/tavr-approaches/.

[50] J.-C. Laborde, S. J. Brecker, D. Roy and M. Jahangiri, "Complications at the Time of Transcatheter Aortic Valve Implantation," *Methodist Debakey Cardiovascular Journal,* vol. 8, no. 2, pp. 38-41, April-June 2012.

[51] "Embolic Stroke," Cleveland Clinic, [Online]. Available: https://my.clevelandclinic.org/health/diseases/embolic-stroke.

[52] P. Reddy, I. Merdler, I. Ben-Dor, L. F. Satler, T. Rogers and R. Waksman, "Cerebrovascular events after transcatheter aortic valve implantation," *EuroIntervention,* vol. 20, no. 13, pp. e793-e805, July 2024.

[53] J. D. Carrol, M. J. Mack, S. Vemulapalli, H. C. Herrmann, T. G. Gleason, G. Hanzel, M. G. Deeb, V. H. Thourani, D. J. Cohen, N. Desai, A. J. Kirtane, S. Fitzgerald, J. Michaels, C. Krohn, F. A. Masoudi, R. G. Brindis and J. E. Bavaria, "STS-ACC TVT Registry of Transcatheter Aortic Valve Replacement," *Journal of the American College of Cardiology,* vol. 76, no. 21, 2020.

[54] M. J. Mack, M. B. Leon, V. H. Thourani, R. Makkar, S. K. Kodali, M. Russo, S. R. Kapadia, C. Malaisrie, D. J. Cohen, P. Pibarot, J. Leipsic, R. T. Hahn, P. Blanke, M. R. Willams, J. M. McCabe, D. L. Brown, V. Babaliaros, S. Goldman, W. Y. Szeto, P. Genereux, A. Pershad, S. J. Pocock, M. C. Alu, J. G. Webb and C. R. Smith, "Transcatheter Aortic-Valve Replacement with a Balloon-Expandable Valve in Low-Risk Patients," *The New England Journal of Medicine,* vol. 380, no. 18, pp. 1695-1705, 2019.

[55] O. De Backer, J. H. Butt, Y.-H. Wong, C. Torp-Pedersen, C. J. Terkelsen, H. Nissel, E. L. Fosbøl, L. Køber and L. Søndergaard, "Early and late risk of ischemic stroke after TAVR as compared to a nationwide background population," *Clinical Research in Cardiology,* vol. 109, pp. 791-801, 30 October 2019.

[56] C. D. Maida, M. Daidone, G. Pacinella, R. L. Norrito, A. Pinto and A. Tuttolomondo, "Diabetes and Ischemic Stroke: An Old and New Relationship an Overview of the Close Interaction between These Diseases," *International Journal of Molecular Sciences,* vol. 23, no. 4, p. 2397, 21 February 2022.

[57] V. A. Jimenez Diaz, R. Estevez Loureiro, J. A. Baz Alonso, P. J. Salvadores, G. Bastos Fernandez, B. Caneiro Queija, C. Veiga Garcia and A. Iñiguez Romo, "Stroke prevention during and after transcatheter aortic valve implantation: From cerebral protection devices to antithrombotic management," *Frontiers in Cardiovascular Medicine,* vol. 9, p. 958732, 17 October 2022.

[58] J. P. Fanning, A. J. Wesley, D. L. Walters, A. A. Wong, A. G. Barnett, W. E. Strugnell, D. G. Platts and J. F. Fraser, "Topographical distribution of perioperative cerebral infarction associated with transcatheter aortic valve implantation," *American heart journal,* vol. 197, pp. 113-123, 8 December 2017.

[59] S. Haussig, N. Mangner, M. G. Dwyer, L. Lehmkuhl, C. Lücke, F. Woitek, D. M. Holzhey, F. W. Mohr, M. Gutberlet, R. Zivadinov, G. Schuler and A. Linke, "Effect of a Cerebral Protection Device on Brain Lesions Following Transcatheter Aortic Valve Implantation in Patients With Severe Aortic Stenosis: The CLEAN-TAVI Randomized Clinical Trial," *JAMA,* vol. 316, no. 6, pp. 592-601, 9 August 2016.

[60] P. M. Ndunda, M. R. Vindhyal, T. M. Muutu and Z. Fanari, "Clinical Outcomes of Sentinel Cerebral Protection System Use During

Transcatheter Aortic Valve Replacement: A Systematic Review and Meta-Analysis," *Cardiovascular revascuarization medicine: including molecular intervention,* vol. 21, no. 6, pp. 717-722, 25 April 2019.

[61] S. R. Kapadia, S. Kodali, R. Makkar, R. Mehran, R. M. Lazar, R. Zivadinov, M. G. Dwyer, H. Jilaihawi, R. Virmani, S. Anwaruddin, V. H. Thourani, T. Nazif, N. Mangner, F. Woitek, A. Krishnaswamy, S. Mick, T. Chakravarty, M. Nakamura, J. M. McCabe, L. Satler, A. Zajarias, W. Y. Szeto, L. Svensson, M. C. Alu, R. M. White, C. Kraemer, A. Parhizgar, M. B. Leon and A. Linke, "Protection Against Cerebral Embolism During Transcatheter Aortic Valve Replacement," *Journal of American College of Cardiology,* vol. 69, no. 4, pp. 367-377, 31 January 2017.

[62] A. Baumbach, M. Mullen, A. M. Brickman, S. K. Aggarwal, C. G. Pietras, J. K. Forrest, D. Hildick-Smith, S. M. Meller, L. Gambone, P. den Heijer, P. Margolis, S. Voros and A. J. Lansky, "Safety and performance of a novel embolic deflection device in patients undergoing transcatheter aortic valve replacement: results from the DEFLECT I study," *EuroIntervention,* vol. 11, no. 1, May 2015.

[63] M. Samim, B. van der Worp, P. Agostoni, J. Hendrikse, R. P. J. Budde, F. Nijhoff, F. Ramjankhan, P. A. Doevendans and P. R. Stella, "TriGuard™ HDH embolic deflection device for cerebral protection during transcatheter aortic valve replacement," *Catheterization and Cardiovascular Interventions,* vol. 89, no. 3, pp. 470-477, 15 February 2017.

[64] A. J. Lansky, J. Schofer, D. Tchetche, P. Stella, C. G. Pietras, H. Parise, K. Abrams, J. K. Forrest, M. Cleman, J. Reinöhl, T. Cuisset, D. Blackman, G. Bolotin, S. Spitzer, U. Kappert, M. Gilard, T. Modine, D. Hildick-Smith, M. Haude, P. Margolis, A. M. Brickman, S. Voros and A. Baumbach, "A prospective randomized evaluation of the TriGuard™ HDH embolic DEFLECTion device during transcatheter aortic valve implantation: results from the DEFLECT III trial," *European Heart Journal,* vol. 36, no. 31, pp. 2070-2078, 14 August 2015.

[65] A. J. Lansky, R. Makkar, T. Nazif, S. Messé, J. Forrest, R. Sharma, J. Schofer, A. Linke, D. Brown, A. Dhole, P. Horwitz, M. Zang, F. DeMarco, V. Rajagopal, M. G. Dwyer, R. Zivadinov, P. Stella, J. Rovin, H. Parise, S. Kodali, A. Baumbach and J. Moses, "A randomized evaluation of the TriGuard™ HDH cerebral embolic protection device to Reduce the Impact of Cerebral Embolic LEsions after TransCatheter Aortic Valve

ImplanTation: the REFLECT I trial," *European Heart Journal,* vol. 42, no. 27, pp. 2670-2679, 15 July 2021.

[66] T. M. Nazif, J. Moses, R. Sharma, A. Dhoble, J. Rovin, D. Brown, P. Horwitz, R. Makkar, R. Stoler, J. Forrest, S. Messé, S. Dickerman, J. Brennan, R. Zivadinov, M. G. Dwyer, A. J. Lansky and REFLECT II Trial Investigators, "Randomized Evaluation of TriGuard 3 Cerebral Embolic Protection After Transcatheter Aortic Valve Replacement: REFLECT II," *JACC: Cardiovascular Interventions,* vol. 14, no. 5, 8 March 2021.

[67] A. Latib, A. Mangieri, P. Vezzulli, P. Spagnolo, F. Sardanelli, G. Fellegara, M. Pagnesi, F. Giannini, A. Falini, R. Gorla, M. Montorfano, F. Bedogni, A. Colombo, J. Popma, W. M. Merhi and F. De Marco, "First-in-Man Study Evaluating the Emblok Embolic Protection System During Transcatheter Aortic Valve Replacement," *JACC: Cardiovascular Interventions,* vol. 13, no. 7, 13 April 2020.

[68] D. Mylotte, I. Narbute, A. Neylon, U. Schäfer, N. Werner, R. Virmani, F. Kolodgie, R. Zivadinov and A. Erglis, "TCT-43 First-in-human experience of a novel transradial device for embolic deflection during transcatheter aortic valve replacement," *Journal of the American College of Cardiology,* vol. 72, no. 13_Supplement, 17 September 2018.

[69] D. Jagielak, R. Targonski, C. Frerker, M. Abdel-Wahab, J. Wilde, N. Werner, M. Lauterbach, J. Leick, M. Grygier, M. Misterski, A. Erglis, I. Narbute, A. R. Witkowski, M. Adam, D. Frank, F. Gatto, T. Schmidt and A. J. Lansky, "Safety and performance of a novel cerebral embolic protection device for transcatheter aortic valve implantation: the PROTEMBO C Trial," *EuroIntervention,* vol. 18, no. 7, pp. 590-597, 20 September 2022.

[70] A. Vahanian, F. Beyersdorf, F. Praz, M. Milojevic, S. Baldus, J. Bauersachs, D. Capodanno, L. Conradi, M. De Bonis, R. De Paulis, V. Delgado, N. Freemantle, M. Gilard, K. H. Haugaa, A. Jeppsson, P. Jüni, L. Pierard, B. D. Prendergast, J. R. Sádaba, C. Tribouillot, W. Wojakowski, ESC/EACTS Scientific Document Group and ESC National Cardiac Societies, "2021 ESC/EACTS Guidelines for the management of valvular heart disease," *European Heart Journal,* vol. 43, no. 7, pp. 561-632, 14 February 2022.

[71] C. M. Otto, R. A. Nishimura, R. O. Bonow, B. A. Carabello, J. P. Erwin III, F. Gentile, H. Jneid, E. V. Krieger, M. Mack, C. McLeod, P. T. O'Gara, V. H. Rigolin, T. M. Sundt III, A. Thompson and C. Toly, "2020 ACC/AHA

Guideline for the Management of Patients With Valvular Heart Disease: A Report of the American College of Cardiology/American Heart Association Joint Committee on Clinical Practice Guidelines," *American Heart Journal,* vol. 143, no. 5, 2 February 2021.

[72] M. L. Carerj, D. Restelli, C. Poleggi, G. Di Bella, C. Zito, R. Manganaro, M. C. Piccione, G. Trimarchi, A. Farina, A. Micari and S. Carerj, "The Role of Imaging in Cardiovascular Prevention: A Comprehensive Review," *Journal of Cardiovascular Echography,* vol. 35, no. 1, pp. 8-18, January-March 2025.

[73] S. Omerovic and A. Jain, "Echocardiogram," in *StatPearls*, 2023.

[74] "Computed Tomography (CT)," National Institute of Biomedical Engineering and Bioengineering, 2025. [Online]. Available: https://www.nibib.nih.gov/science-education/science-topics/computed-tomography-ct.

[75] Í. C. de Macedo Pontes, C. Pinto Brito de Figueiredo Guimarães, E. K. Ururahy, N. Fonseca, M. Marques Almeida Silva, R. Sasdelli Neto and W. Y. Ishikawa, "Computed tomography angiography in the planning of transcatheter aortic valve replacement: a step-by-step approach," *Radiologia Brasileira,* vol. 55, no. 6, pp. 373-379, November - December 2022.

[76] "Magnetic Resonance Imaging (MRI)," National Institute of Biomedical Imaging and Bioengineering, [Online]. Available: https://www.nibib.nih.gov/science-education/science-topics/magnetic-resonance-imaging-mri.

[77] A. Chaturvedi, S. K. Hobbs, F. S. Ling, A. Chaturvedi and P. Knight, "MRI evaluation prior to Transcatheter Aortic Valve Implantation (TAVI): When to acquire and how to interpret," *Insights Imaging,* vol. 7, no. 2, pp. 245-254, 25 February 2016.

[78] J.-P. Wenzel, E. L. Petersen, J. Nikorowitsch, J. Senftinger, C. R. Sinning, M. Theissen, J. Petersen, H. Reichenspurner and E. Girdauskas, "Transthoracic echocardiographic reference values of the aortic root: results from the Hamburg City Health Study," *The International Journal of Cardiovascular Imaging,* vol. 37, pp. 3513-3524, December 2021.

[79] A. Abdrabou, R. Sharma, A. Murphy and et al., "CT angiography of the cerebral arteries (protocol)," *Radiopaedia.org,* 3 June 2025.

[80] C. Stöllberger, W. Kopsa and J. Finsterer, "Resolution of an aortic thrombus under anticoagulant therapy," *European Journal of Cardio-thoracic Surgery,* vol. 20, pp. 880-882, November 2001.

[81] R. Pfleger, J. Yap, Y. Mellam and et al., "Hybrid Imaging," *Radiopaedia.org,* 16 September 2025.

[82] A. J. Wheaton and M. Miyazaki, "Non-contrast enhanced MR angiography: Physical principles," *Journal of Magnetic Resonance Imaging,* vol. 36, no. 2, pp. 286-304, 17 July 2012.

[83] M. Bustamante, V. Gupta, C.-J. Carlhäll and T. Ebbers, "Improving visualization of 4D flow cardiovascular magnetic resonance with four-dimensional angiographic data: generation of a 4D phase-contrast magnetic resonance CardioAngiography (4D PC-MRCA)," *Journal of Cardiovascular Magnetic Resonance,* vol. 19, p. 47, 23 June 2017.

[84] K. D. Kurz, G. Ringstad, A. Odland, R. Advani, E. Farbu and M. W. Kurz, "Radiological imaging in acute ischaemic stroke," *European Journal of Neurology,* vol. 23, no. S1, pp. 8-17, 13 November 2015.

[85] M. Y. Sikkandar, N. M. Sudharsan, S. S. Begum and et al., "Computational Fluid Dynamics: A Technique to Solve Complex Biomedical Engineering Problems - A Review," *WSEAS TRANSACTIONS on BIOLOGY and BIOMEDICINE,* vol. 16, pp. 2224-2902, 2019.

[86] B. Chung and J. R. Cebral, "CFD for Evaluation and Treatment Planning of Aneurysms: Review of Proposed Clinical Uses and Their Challenges," *Annals of Biomedical Engineering,* vol. 43, pp. 122-138, 4 September 2014.

[87] S. Li, B. W. Karney and G. Liu, "FSI research in pipeline systems – A review of the literature," *Journal of Fluids and Structures,* vol. 57, pp. 277-297, August 2015.

[88] V. Carvalho, D. Lopes, J. Silva, H. Puga, R. A. Lima, J. Teixeira and F. C. F. Teixeira, "Comparison of CFD and FSI Simulations of Blood Flow in Stenotic Coronary Arteries," in *Applications of Computational Fluid Dynamics Simulation and Modeling*, 2022.

[89] K. Capellini, “Development of new simulation strategies to investigate aorta hemodynamics by integrating in-vivo data and RBF mesh morphing approach,” 4 November 2022. [Online]. Available: https://hdl.handle.net/20.500.14242/216687.

[90] E. I. Basri, A. A. Basri, N. V. Riazuddin, S. F. Shahwir, M. Zuber and K. A. Ahmad, “Computational Fluid Dynamics Study in Biomedical Application: A Review,” *International Journal of Fluids and Heat Transfer,* vol. 1, no. 2, 9 June 2016.

[91] A. Fedorov, R. Beichel, J. Kalpathy-Cramer, J. Finet, J.-C. Fillion-Robin, S. Pujol, C. Bauer, D. Jennings, F. Fennessy, M. Sonka, J. Buatti, S. Aylward, J. V. Miller, S. Pieper and R. Kikinis, “3D Slicer as an image computing platform for the Quantitative Imaging Network,” *Magnetic Resonance Imaging,* vol. 30, no. 9, pp. 1323-1341, 30 November 2021.

[92] T. Chen, Y.-T. Que, Y.-H. Zhang, F.-Y. Long, Y. Li, X. Huang, Y.-N. Wang, Y.-F. Hu, J. Yu and G.-X. Li, “Using Materialise's interactive medical image control system to reconstruct a model of a patient with rectal cancer and situs inversus totalis: A case report,” *World Journal of Clinical Cases,* vol. 8, no. 4, pp. 806-814, 26 February 2020.

[93] “ITK: The Insight Toolkit,” [Online]. Available: https://pypi.org/project/itk/.

[94] S. M. Khaniabadi, H. Ibrahim, I. A. Huqqani, F. M. Khaniabadi, H. A. M. Sakim and S. S. Teoh, “Comparative Review on Traditional and Deep Learning Methods for Medical Image Segmentation,” in *2023 IEEE 14th Control and System Graduate Research Colloquium (ICSGRC)*, 2023.

[95] J. Wasserthal, H.-C. Breit, M. T. Meyer, M. Pradella, D. Hinck, A. W. Sauter, T. Heye, D. T. Boll, J. Cyriac, S. Yang, M. Bach and M. Segeroth, “TotalSegmentator: Robust Segmentation of 104 Anatomic Structures in CT Images,” *Radiology: Artificial Intelligence,* vol. 5, no. 5, 5 July 2023.

[96] S. Saitta, F. Sturla, A. Caimi, A. Riva, M. C. Palumbo, G. Nano, E. Votta, A. Della Corte, M. Glauber, D. Chiappino, M. M. Marrocco-Trischitta and A. Redaelli, “A Deep Learning-Based and Fully Automated Pipeline for Thoracic Aorta Geometric Analysis and Planning for Endovascular Repair from Computed Tomography,” *Journal of Digital Imaging,* vol. 35, pp. 226-239, 26 January 2022.

[97] N. S. Cepero and S. C. Shadden, "SeqSeg: Learning Local Segments for Automatic Vascular Model Construction," *Annals of Biomedical Engineering,* vol. 53, no. 1, pp. 158-179, 18 September 2024.

[98] "Extending the Inlets and Outlets for a CFD Simulation," SimScale, [Online]. Available: https://www.simscale.com/knowledge-base/extending-the-inlets-and-outlets-for-a-cfd-simulation/.

[99] N. Bray, "Notes on Mesh Smoothing," 18 October 2004. [Online]. Available: https://www.ljll.fr/~frey/papers/meshing/Bray%20N.,%20Notes%20on%20mesh%20smoothing.pdf.

[100] G. Taubin, "Curve And Surface Smoothing Without Shrinkage," Yorkton Heights, NY 10598, 1995.

[101] "The Importance of Meshing in CFD: Accuracy and Best Practices for Mesh Studies," Simularge, [Online]. Available: https://www.simularge.com/blog/the-importance-of-meshing-in-cfd-accuracy-and-bestpractices-for-mesh-studies.

[102] H. Wang and Z. Zhai, "Analyzing grid independency and numerical viscosity of computational fluid dynamics for indoor environment applications," *Building and Environment,* vol. 52, pp. 107-118, 30 December 2011.

[103] P. J. Roache, "Perspective: A Method for Uniform Reporting of Grid Refinement Studies," *Journal of Fluid Engineering,* vol. 116, no. 3, pp. 405-413, 1 September 1994.

[104] SimScale, "SimScale Documentation," SimScale, [Online]. Available: https://www.simscale.com/docs/simulation-setup/meshing/mesh-quality/.

[105] M. López-Pachón and J. Marcé-Nogué, "The crucial role of meshing in computational fluid dynamics simulations for organic geometries in paleobiology: Describing fluid dynamics performance through best practices," *Methods in Ecology and Evolution,* vol. 16, no. 10, pp. 2170-2194, 29 August 2025.

[106] Symscape, "Polyhedral, Tetrahedral, and Hexahedral Mesh Comparison," Symscape, [Online]. Available:

https://www.symscape.com/polyhedral-tetrahedral-hexahedral-mesh-comparison.

[107] A. M. Al-Jumaily, M. Al-Rawi, D. Belkacemi, R. A. Sascău, C. Stătescu, F.-E. Țurcanu and L. Anghel, "Computational Modeling Approach to Profile Hemodynamical Behavior in a Healthy Aorta," *Bioengineering (Basel),* vol. 11, no. 9, p. 914, 12 September 2024.

[108] N. Bappoo, L. J. Kelsey, L. Parker, T. Crough, C. M. Moran, A. Thomson, M. C. Holmes, C. S. Wyrwoll and B. J. Doyle, "Viscosity and haemodynamics in a late gestation rat feto-placental arterial network," *Biomechanics and Modeling in Mechanobiology,* vol. 16, pp. 1361-1372, 16 August 2017.

[109] K. Tran, W. Yang, A. Marsden and J. T. Lee, "Patient-specific computational flow modelling for assessing hemodynamic changes following fenestrated endovascular aneurysm repair," *JVS - Vascular Science,* vol. 2, pp. 53-69, 3 March 2021.

[110] "SimVascular Mesh Generation," Stanford University, [Online]. Available: https://simvascular.github.io/documentation/meshing.html.

[111] L. Shadid, J. Rice, H. Berhane, C. Rigsby, J. Robinson, L. Griffin, M. Markl and A. Roldán-Alzate, "Enhanced 4D Flow MRI-Based CFD with Adaptive Mesh Refinement for Flow Dynamics Assessment in Coarctation of the Aorta," *Annals of Biomedical Engineering,* vol. 50, no. 8, pp. 1001-1016, 27 May 2022.

[112] A. Ramella, F. Migliavacca, J. F. Rodriguez Matas, F. Heim, F. Dedola, S. Marconi, M. Conti, S. Allievi, T. J. Mandigers, D. Bissaco, M. Domanin, S. Trimarchi and G. Luraghi, "Validation and Verification of High-Fidelity Simulations of Thoracic Stent-Graft Implantation," *Annals of Biomedical Engineering,* vol. 50, pp. 1941-1953, 19 July 2022.

[113] D. M. Marin Castrillon, "Segmentation of the aorta from 4D flow MRI for biomarkers computation," Dijon, 2022.

[114] N. C. Ohalete, O. Ayo-Farai, C. Onwumere, C. P. Maduka and T. O. Olorunsogo, "Navier-stokes equations in biomedical engineering: A critical review of their use in medical device development in the USA and Africa," *World Journal of Advanced Research and Reviews,* vol. 21, no. 01, pp. 1115-1131, 11 January 2024.

[115] "Navier-Stokes Equation – viscous fluid flow, pressure & inertia explained," Turn 2 Engineering, [Online]. Available: https://turn2engineering.com/equations/navier-stokes-equation.

[116] S. A. Wajihah and D. S. Sankar, "A review on non-Newtonian fluid models for multi-layered blood rheology in constricted arteries," *Archive of Applied Mechanics,* vol. 93, pp. 1771-1796, 31 January 2023.

[117] E. Jessen, M. C. Steinbach, C. Debbaut and D. Schillinger, "Branching exponents of synthetic vascular trees under different optimality principles," April 2023. [Online]. Available: https://www.researchgate.net/publication/370227322_Branching_exponents_of_synthetic_vascular_trees_under_different_optimality_principles.

[118] G. Fragomeni, "Newtonian and non-Newtonian blood model, a comparative study on large and small vessels," 2023. [Online]. Available: https://www.cal-tek.eu/proceedings/i3m/2023/iwish/007/pdf.pdf.

[119] H. Liu, L. Lan, J. Abrigo, H. L. Ip, Y. Soo, D. Zheng, K. S. Wong, D. Wang, L. Shi, T. W. Leung and X. Leng, "Comparison of Newtonian and Non-newtonian Fluid Models in Blood Flow Simulation in Patients With Intracranial Arterial Stenosis," *Frontiers of Physiology (section: Computational Physiology and Medicine),* vol. 12, 2021.

[120] Y. Zhu, S. Mirsadraee, U. Rosendahl, J. Pepper and X. Y. Xu, "Fluid-Structure Interaction Simulations of Repaired Type A Aortic Dissection: a Comprehensive Comparison With Rigid Wall Models," *Frontier of Physiology (section: Computational Physiology and Medicine),* vol. 13, 14 June 2022.

[121] M. A. Day, "The no-slip condition of fluid dynamics," *Erkenntnis,* vol. 33, pp. 285-296, November 1990.

[122] "CFD Simulation - Beta Version," Stanford University, [Online]. Available: https://simvascular.github.io/documentation/cfd_simulation.html#boundary_conditions.

[123] C. Greenshields and H. Weller, Notes on Computational Fluid Dynamics: General Principles, Chicago (Naperville), USA, 2022.

[124] "Exploring Inlet Boundary Conditions in CFD: Types and Applications," Simularge, [Online]. Available: https://www.simularge.com/blog/exploring-inlet-boundary-conditions-in-cfd.

[125] S. Madhavan and E. M. C. Kemmerling, "The effect of inlet and outlet boundary conditions in image-based CFD modeling of aortic flow," *BioMedical Engineering OnLine,* vol. 17, no. 66, 30 May 2018.

[126] S. Saitta, L. Maga, C. Armour, E. Votta, D. P. O'Regan, M. Y. Salmasi, T. Athanasiou, J. W. Weinsaft, X. Y. Xu, S. Pirola and A. Redaelli, "Data-driven generation of 4D velocity profiles in the aneurysmal ascending aorta," *Computer Methods and Programs in Biomedicine,* vol. 233, p. 107468, 13 March 2023.

[127] P. Xu, X. Liu, H. Zhang, D. Ghista, D. Zhang, C. Shi and W. Huang, "Assessment of boundary conditions for CFD simulation in human carotid artery," *Biomechanics and Modeling in Mechanobiology,* vol. 17, pp. 1581-1597, 7 July 2018.

[128] B. Liu, J. Zheng, R. Bach and D. Tang, "Influence of model boundary conditions on blood flow patterns in a patient specific stenotic right coronary artery," *BioMedical Engineering Online,* vol. 14 (Suppl 1), no. S6, 9 January 2015.

[129] S. Pirola, O. A. Jarral, D. P. O'Regan, G. Asimakopoulos, J. R. Anderson, J. R. Pepper, T. Athanasiou and X. Y. Xu, "Computational study of aortic hemodynamics for patients with an abnormal aortic valve: The importance of secondary flow at the ascending aorta inlet," *APL Bioengineering,* vol. 2, no. 2, p. 026101, 16 March 2016.

[130] P. Youssefi, A. Gomez, C. Arthurs, R. Sharma, M. Jahangiri and C. A. Figueroa, "Impact of Patient-Specific Inflow Velocity Profile on Hemodynamics of the Thoracic Aorta," *Journal of Biomechanical Engineering,* vol. 140, no. 1, p. 011002 (14 pages), 19 October 2017.

[131] S. Pirola, Z. Cheng, O. A. Jarral, D. P. O'Regan, J. R. Pepper, T. Athanasiou and X. Y. Xu, "On the choice of outlet boundary conditions for patient-specific analysis of aortic flow using computational fluid dynamics," *Journal of Biomechanics,* vol. 60, pp. 15-21, 1 August 2017.

[132] N. Westerhof, J.-W. Lankhaar and B. E. Westerhof, "The arterial Windkessel," *Medical & Biological Engineering & Computing,* vol. 47, pp. 131-141, 10 June 2008.

[133] J. F. LaDisa, A. Figueroa, I. E. Vignon-Clementel, H. J. Kim, N. Xiao, L. M. Ellwein, F. P. Chan, J. A. Feinstein and C. A. Taylor, "Computational Simulations for Aortic Coarctation: Representative Results From a Sampling of Patients," *Journal of Biomechanical Engineering,* vol. 33, no. 9, p. 091008 (9 pages), 14 October 2011.

[134] A. S. Les, S. C. Shadden, A. Figueroa, J. M. Park, M. M. Tedesco, R. J. Herfkens, R. L. Dalman and C. A. Taylor, "Quantification of Hemodynamics in Abdominal Aortic Aneurysms During Rest and Exercise Using Magnetic Resonance Imaging and Computational Fluid Dynamics," *Annals of Biomedical Engineering,* vol. 38, pp. 1288-1313, 9 February 2010.

[135] N. Xiao, J. Alastruey and C. A. Figueroa, "A systematic comparison between 1-D and 3-D hemodynamics in compliant arterial models," *International Journal for Numerical Methods in Biomedical Engineering,* vol. 30, no. 2, pp. 204-231, 24 September 2013.

[136] P. Reymond, F. Merenda, F. Perren, D. Rüfenacht and N. Stergiopulos, "Validation of a one-dimensional model of the systemic arterial tree," *American Journal of Physiology - Heart and Circulatory Physiology,* vol. 297, no. 1, pp. H208-H222, 2009.

[137] Z. Li and W. Mao, "A fast approach to estimating Windkessel model parameters for patient-specific multi-scale CFD simulations of aortic flow," *Computers and Fluids,* vol. 259, p. 105894, 2023.

[138] G. Caminha, "The CFL Condition and How to Choose Your Timestep Size," SimScale, 11 March 2024. [Online]. Available: https://www.simscale.com/blog/cfl-condition/.

[139] H. Sakamoto, T. Hattori, A. Tada and V. Nguyen, "Analysis of Navier-Stokes Equation from the Viewpoint of Advection Diffusion," *Journal of Robotics Networking and Artificial Life,* vol. 1, no. 4, p. 265, February 2015.

[140] B. N. Biswas, S. Chatterjee, S. P. Mukherjee and S. Pal, "A DISCUSSION ON EULER METHOD: A REVIEW," *Electronic Journal of Mathematical Analysis and Applications,* vol. 1, no. 2, pp. 294-317, July 2013.

[141] P. G. Dake, J. Mukherjee, K. C. Sahu and A. B. Pandit, “Computational Fluid Dynamics in Cardiovascular Engineering: A Comprehensive Review,” *Transactions of the Indian National Academy of Engineering,* vol. 9, 10 April 2024.

[142] M. Al-Rawi, D. Belkacemi, E. T. A. Lim and M. Khashram, “Investigation of Type A Aortic Dissection Using Computational Modelling,” *Biomedicines,* vol. 12, no. 9, p. 1973, 1 September 2024.

[143] S. C. Shadden and A. Arzani, “Lagrangian Postprocessing of Computational Hemodynamics,” *Annals of Biomedical Engineering,* vol. 43, pp. 41-58, 25 July 2014.

[144] M. R. Maxey and J. J. Riley, “Equation of motion for a small rigid sphere in a nonuniform flow,” *Physics of Fluids,* no. 26, p. 883–889, 1983.

[145] P. Vallés, M. Morales-Hernàndez, V. Roeber, P. Garcìa-Navarro and D. Caviedes-Voullième, “SERGHEI v2.1: a Lagrangian model for passive particle transport using a two-dimensional shallow water model (SERGHEI-LPT),” *Geosci. Model Dev.,* vol. 18, pp. 7399-7416, 17 October 2025.

[146] F. Malone, E. McCarthy, P. Delassus, J.-H. Buhk, J. Fiehler and L. Morris, “Investigation of the Hemodynamics Influencing Emboli Trajectories Through a Patient-Specific Aortic Arch Model,” *American Stroke Association - a division of American Heart Association,* vol. 50, no. 6, 16 April 2019.

[147] J. P. Hague, J. Keelan, L. Beishon, D. Swienton, T. G. Robinson and E. M. L. Chung, “Three-dimensional simulations of embolic stroke and an equation for sizing emboli from imaging,” *Scientific Reports,* vol. 13, no. 3021, 21 February 2023.

[148] F. Stentella, “"Image-based computational fluid dynamics to assess the effect of aortic arch morphology on cardiogenic embolic transport to the brain",” 11 December 2024. [Online]. Available: https://hdl.handle.net/10589/231365.

[149] D. Fabbri, Q. Long, S. Das and M. Pinelli, “Computational modelling of emboli travel trajectories in cerebral arteries: influence of microembolic particle size and density,” *Biomechanics and Modelling in Mechanobiology,* vol. 13, no. 2, pp. 289-302, 2 March 2014.

[150] P. Talebibarmi, B. Vahidi and M. Ebad, "In silico analysis of embolism in cerebral arteries using fluid-structure interaction method," *Heliyon,* vol. 10, no. 9, p. e30443, 1 May 2024.

[151] K. Woldendorp, B. Indja, P. G. Bannon, J. P. Fanning, B. T. Plunkett and S. M. Grieve, "Silent brain infarcts and early cognitive outcomes after transcatheter aortic valve implantation: a systematic review and meta-analysis," *European Heart Journal,* vol. 42, no. 10, pp. 1004-1015, 1 February 2021.

[152] G. V. Lo Russo, H. S. Alarouri, A. Al-Abcha, B. Vogl, A. Mahayni, A. Sularz, H. Hatoum, J. Collins, J. A. Crestanello and A. Mohamad, "Association of Bovine Arch Anatomy With Incident Stroke After Transcatheter Aortic Valve Replacement," *Journal of the American Heart Association,* vol. 13, no. 4, 13 February 2024.

[153] H. W. Choi, T. Luo, J. A. Navia and G. S. Kassab, "Role of Aortic Geometry on Stroke Propensity based on Simulations of Patient-Specific Models," *Scientific Reports,* vol. 7, p. 7065, 1 August 2017.

[154] A. Updegrove, N. M. Wilson, J. Merkow, H. Lan, A. L. Marsden and S. C. Shadden, "SimVascular: An Open Source Pipeline for Cardiovascular Simulation," *Annals of Biomedical Engineering,* vol. 45, no. 3, pp. 525-541, 2017.

[155] "Materialise Launches Integrated Mimics Platform to Accelerate Adoption of Personalized Medical Care," Materialise Mimics, 10 December 2024. [Online]. Available: https://www.materialise.com/en/news/press-releases/integrated-mimics-platform-accelerate-personalized-care.

[156] D. Russo, "Influence of aortic arch type on aortic fluid dynamics: an in vivo quantitative analysis based on 4D Flow MRI," 19 December 2023. [Online]. Available: https://hdl.handle.net/10589/215650.

[157] K. Menon, J. Richter, M. R. Pfaller, J. Pham, E. M. Mathew, K. E. Harold, N. C. Dorn, A. Verma and A. L. Marsden, "svZeroDSolver: A modular package for lumped-parameter cardiovascular simulations," *The Journal of Open Source Software,* vol. 109, no. 7595, pp. 8-10, 2025.

[158] M. R. Pfaller, J. Pham, A. Verma, L. Pegolotti, N. M. Wilson, D. W. Parker, W. Yang and A. L. Marsden, "Automated generation of 0D and 1D

reduced-order models of patient-specific blood flow," *International Journal for Numerical Methods in Biomedical Engineering,* vol. 38, no. 10, p. e3639, 14 August 2022.

[159] "Coronary Normal," Stanford University, [Online]. Available: https://simvascular.github.io/clinical/coronary.html.

[160] V. Scarponi, "Hemodynamic changes due to valve sparing surgery in ascending thoracic aortic aneurysm correction : a tailored multi-patient analysis exploiting the coupled momentum method for fluid-solid interaction," 28 April 2021. [Online]. Available: https://hdl.handle.net/10589/173112.

[161] A. Ruggeri, M. Magliocco, B. Pane, M. Canepa, S. Seitun, G. Pratesi, C. Menna, S. Morganti, G. Spinella and M. Conti, "Patient-specific computational fluid hemodynamics in the ascending aorta before and after thoracic endovascular repair," *Computers in Biology and Medicine,* vol. 194, p. 110493, 3 June 2025.

[162] S. O. Oktar, C. Yücel, D. Karaosmanoglu, K. Akkan, H. Ozdemir, N. Tokgoz and T. Tali, "Blood-Flow Volume Quantification in Internal Carotid and Vertebral Arteries: Comparison of 3 Different Ultrasound Techniques with Phase-Contrast MR Imaging," *American Journal of Neuroradiology,* vol. 27, no. 2, pp. 363-369, February 2006.

[163] B. Hennen, T. Markwirth, B. Scheller, H. -J. Schäfers and O. Wendler, "Do Changes in Blood Flow in the Subclavian Artery Affect Flow Volume in IMA Grafts After Complete Arterial Revascularization with the T-Graft Technique?," *The Thoracic and Cardiovascular Surgeon,* vol. 49, no. 2, pp. 84-88, 2001.

[164] R. Tricarico, S. A. Berceli, R. Tran-Son-Tay and Y. He, "Non-invasive estimation of the parameters of a three-element windkessel model of aortic arch arteries in patients undergoing thoracic endovascular aortic repair," *Front Bioeng Biotechnol.,* no. 11:1127855, (2023).

[165] "svFSI master," Stanford University, [Online]. Available: https://github.com/SimVascular/svFSI/blob/master/svFSI_master.inp.

[166] "svMultiphysics," Stanford University, [Online]. Available: https://simvascular.github.io/documentation/multi_physics.html#numerical_linear_algebra.

[167] S. C. Shadden, FlowVC (Version 1) [Computer software], 2010.

[168] D. Rahdert, W. Sweet, F. Tio, C. Janicki and D. Duggan, “Measurement of density and calcium in human atherosclerotic plaque and implications for arterial brachytherapy,” *Cardiovascular Radiology and Medical Physics,* vol. 1, no. 4, pp. 358-367, 1999.

[169] J. McLester, Applied Biomechanics: Concepts and Connections, Belmont, CA: Cengage Learning, 2007.

[170] T. Schmidt, M. B. Leon, R. Mehran, K.-H. Kuck, M. C. Alu, R. E. Braumann, S. Kodali, S. R. Kapadia, A. Linke, R. Makkar, C. Naber, M. E. Romero, R. Virmani and C. Frerker, “Debris Heterogeneity Across Different Valve Types Captured by a Cerebral Protection System During Transcatheter Aortic Valve Replacement,” *JACC,* vol. 11, no. 13, pp. 1262-1273, 2018.

6 Appendix A: figures

6.1. Mesh Sensitivity Analysis

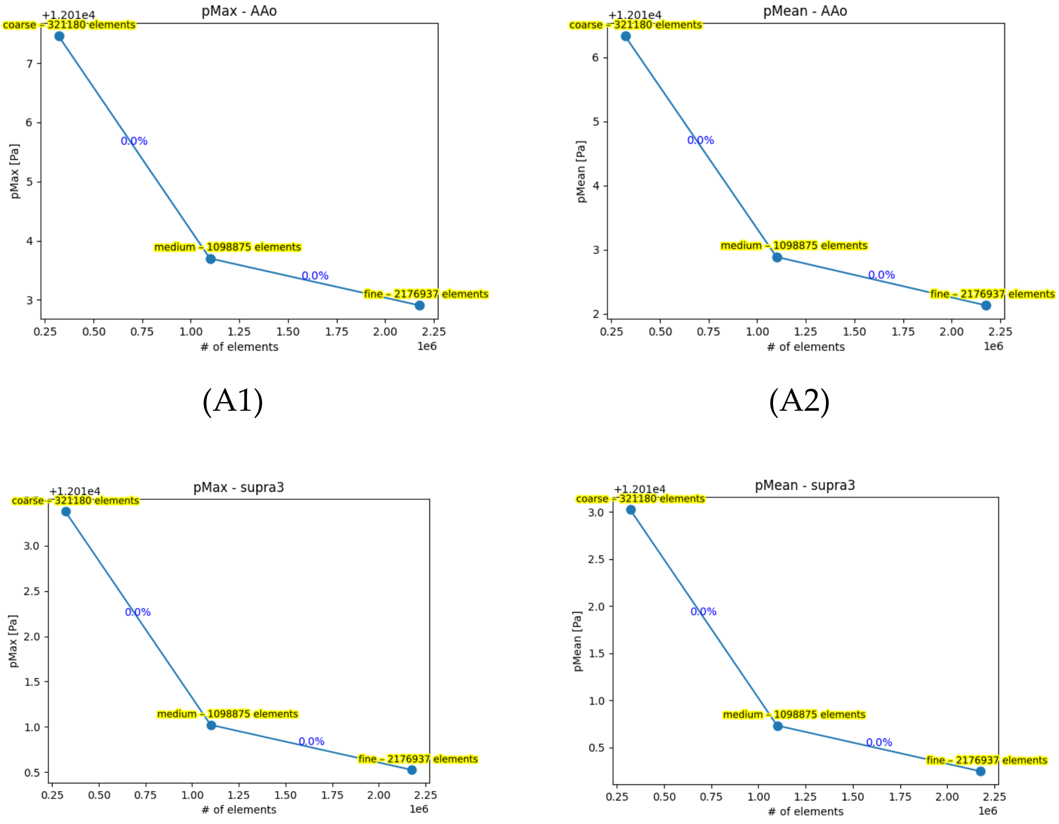

(A1) (A2)

(B1) (B2)

Figure 6.1: pressure plots with percentual differences trend with respect to the number of elements for AAo (A) and LSVA (supra3) slice (B). Figures 1 show the maximum pressure trend, while figures 2 the mean pressure trend.

6.2. Mean velocity curves comparison

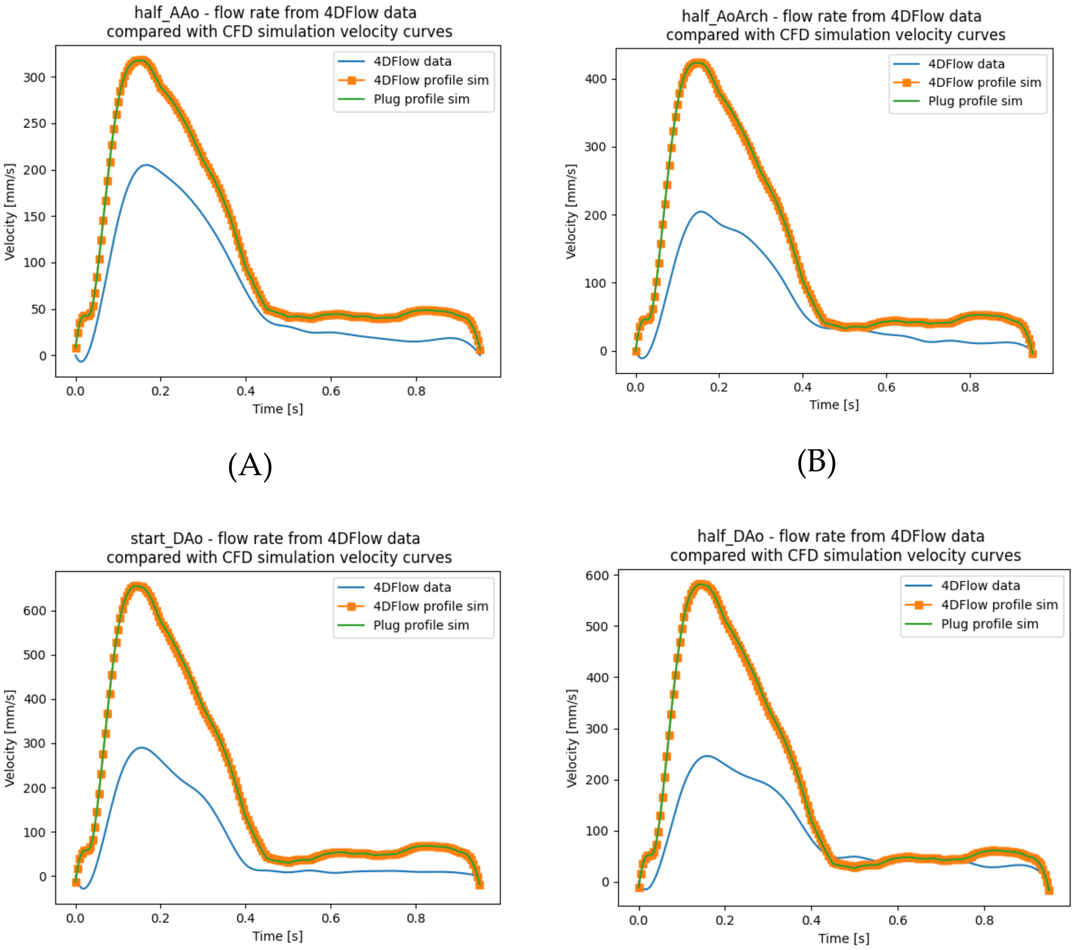

(A)

(B)

(C)

(D)

Figure 6.2: mean velocity curves from 4DFlow data (blue) and from CFD simulations (orange: 4DFlow profile, green: plug profile) comparison (patient 1A).

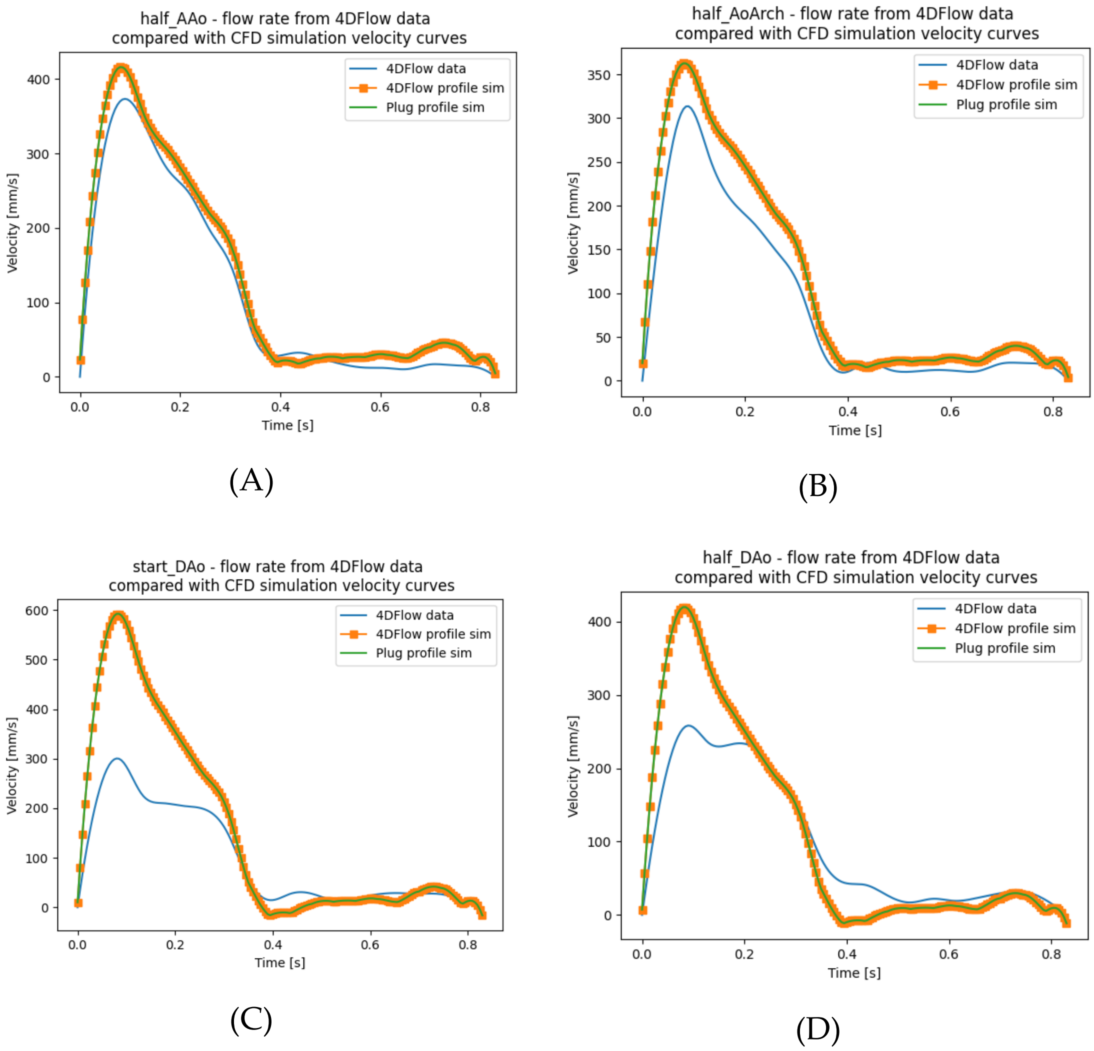

(A) (B)

(C) (D)

Figure 6.3: mean velocity curves from 4DFlow data (blue) and from CFD simulations (orange: 4DFlow profile, green: plug profile) comparison (patient 2A).

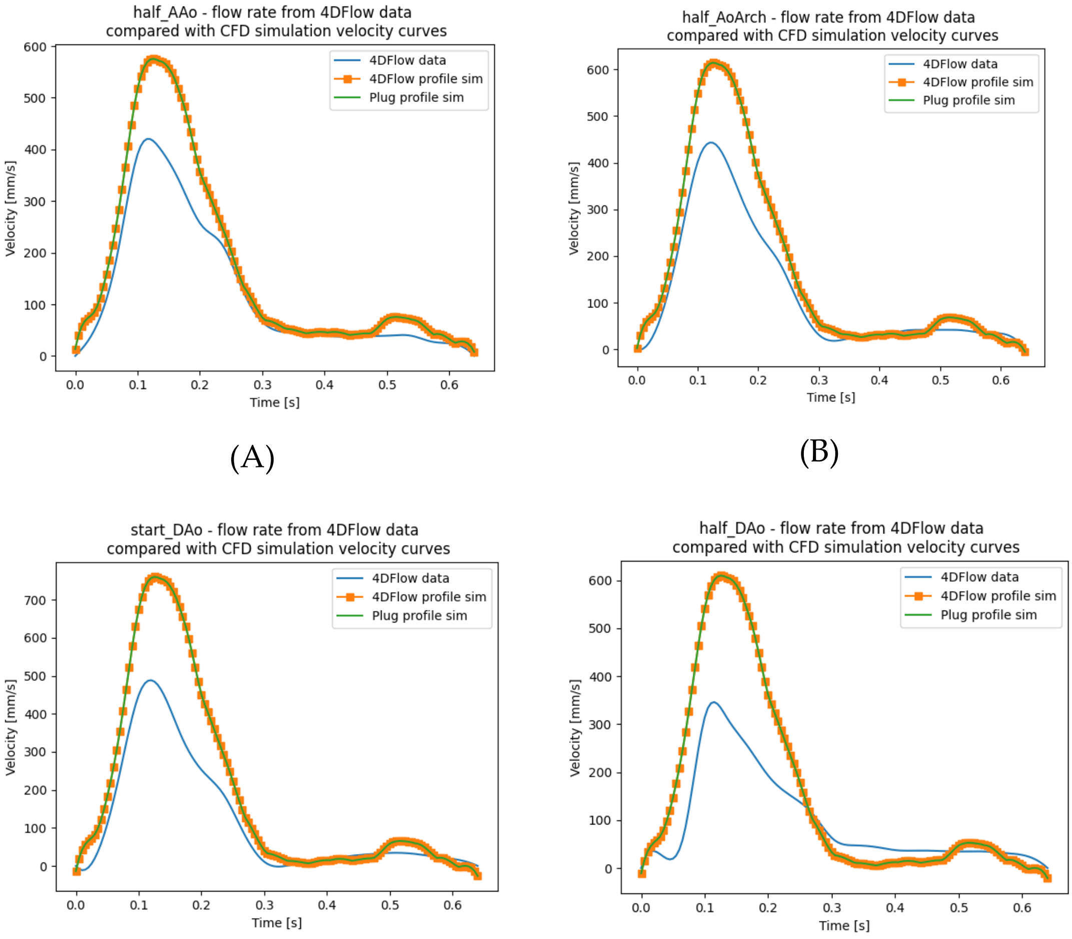

(A)

(B)

(C)

(D)

Figure 6.4: mean velocity curves from 4DFlow data (blue) and from CFD simulations (orange: 4DFlow profile, green: plug profile) comparison (patient 3A).

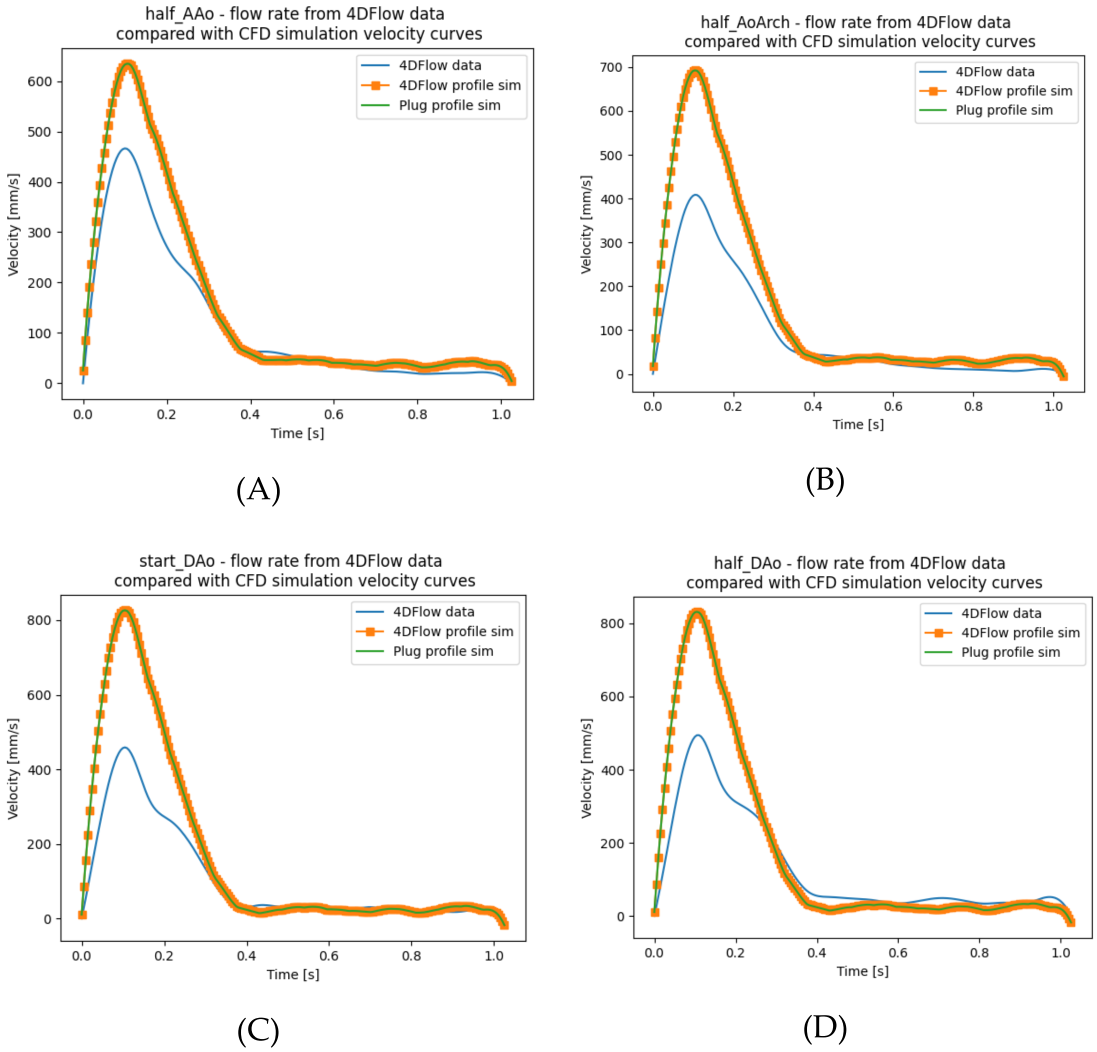

(A) (B)

(C) (D)

Figure 6.5: mean velocity curves from 4DFlow data (blue) and from CFD simulations (orange: 4DFlow profile, green: plug profile) comparison (patient 3B).

7 Appendix B: tables

7.1. 3-EWKM for CFD simulations

Table 7.1: RCR values for outlet BC simulations of each patient. Table A reports patient 1A, 1B and 2A (type I, type I and type II), while table B (next page) reports parameters for patient 3A and 3B (both type III). Resistances are reported in $[\mathrm{Pa} * \mathrm{s}/\mathrm{mm}^3]$, while compliances in $[\mathrm{mm}^3/\mathrm{Pa}]$.

(A)	Patient 1A			Patient 1B			Patient 2A		
	R_p	C	R_d	R_p	C	R_d	R_p	C	R_d
DAo	7.354e-06	8.027	0.223	1.778e-05	7.551	0.237	7.0589e-06	5.808	0.308
LECA	1.572	0.055	14.149	1.673	0.05	15.057	2.134	0.035	19.206
LICA	0.524	0.164	4.715	0.557	0.15	5.014	0.72	0.104	6.479
LSA	0.068	0.406	2.211	0.072	0.375	2.32	0.094	0.257	3.055
LVA	2.502	0.056	11.399	2.702	0.051	12.311	0.934	0.132	4.254
RECA	1.068	0.08	9.615	1.26	0.066	11.337	1.635	0.046	14.714
RICA	0.345	0.249	3.104	0.42	0.199	3.776	0.545	0.138	4.904
RSA	0.049	0.565	1.59	0.055	0.49	1.78	0.072	0.335	2.341
RVA	0.738	0.191	3.362	2.031	0.067	9.25	2.615	0.047	11.912

(B)	**Patient 3A**				**Patient 3B**		
	R_p	**C**	**R_d**		**C**	**R_d**	**R_p**
DAo	7.121e-06	9.956	0.18	**DAo**	7.432e-06	9.358	0.191
LCCA	0.308	0.188	2.774	**LECA**	1.297	0.071	11.67
				LICA	0.429	0.216	3.864
LSA	0.039	0.484	1.254	**LSA**	0.059	0.506	1.913
LVA	0.787	0.121	3.587	**LVA**	2.097	0.072	9.553
RCCA	0.235	0.247	2.118	**RECA**	1.009	0.092	9.081
				RICA	0.335	0.276	3.015
RSA	0.041	0.454	1.337	**RSA**	0.044	0.681	1.423
RVA	1.457	0.065	6.638	**RVA**	1.607	0.095	7.32

7.2. Mesh Sensitivity Analysis

Table 7.2: GCI and k computed for maximum and mean pressure of each slice

P_{Max}	**AAo**	**Supra3**	**P_{Mean}**	**AAo**	**Supra3**
$GCI_{1,2}$	~0	~0	**$GCI_{1,2}$**	~0	~0
$GCI_{2,3}$	~0	~0	**$GCI_{2,3}$**	~0	~0
k	1	1	k	1	1

List of Figures

List of Tables